# Analysis of Residual Stresses in Laser Trimmed Alumina Microelectronic Substrates

by

Kenneth L. Venzant

Thesis submitted to the faculty of the
Virginia Polytechnic Institute and State University
in partial fulfillment of the requirements for the degree of

**MASTER OF SCIENCE**

in

Materials Science and Engineering



APPROVED:

Robert W. Hendricks

Prof. Robert W. Hendricks, Chairman

Ronald S. Gordon

Prof. Ronald S. Gordon

Aicha Elshabini-Riad

Prof. Aicha A. Elshabini-Riad

May, 1993

Blacksburg, Virginia

# Analysis of Residual Stresses in Laser Trimmed Alumina Microelectronic Substrates

by

Kenneth L. Venzant

Committee Chairman: Prof. Robert W. Hendricks

Materials Science and Engineering Department

## (ABSTRACT)

The research presented here investigates the effects of laser trimming on the state of stress in alumina $Al_2O_3$ hybrid microelectronics substrates. Evaluation of stress was performed using x-ray diffraction residual stress analysis and dynamic strain measurements using strain gages before and after laser trimming. X-ray diffraction measurements were carried out in both the longitudinal and transverse directions on the front and back sides of the substrates. The dynamic strain measurements were performed in situ with strain gages attached to the bottom of the substrates while the substrates were trimmed with a 400 watt YAG laser.

The substrates were characterized using optical microscopy, scanning electron microscopy/ energy dispersive x-ray analysis (SEM/EDAX), electron probe microanalysis (EPMA) and electron spectroscopy for chemical analysis (ESCA). The results from these characterization steps gave results for fractography (optical), surface and bulk composition (SEM/EDAX), chemical composition (ESCA) and phase analysis (EPMA).

Results show that laser trimming produces stress gradients which are generally tensile in nature and could have deleterious effects on the mechanical integrity of the substrates if used in hybrid microelectronic applications. Furthermore the stress distribution across the substrates was found to be uniformly distributed showing no peak stresses near the heat affected zone (HAZ) boundary. Phase analysis determined that the substrates contained a magnesium aluminum spinel phase ($MgAl_2O_4$) and that the glass and pore phases are randomly distributed in the substrates. This could have some overal effect on the state of residual stress in the substrates after they have been laser trimmed.

# ACKNOWLEDGEMENTS

The author would like to give sincere thanks and appreciation to the members of his thesis committee: to Professor Robert W. Hendricks for providing guidance, support, and education during the time of this research; Professor Ronald S. Gordon in providing financial support when times of finding money was difficult; and to Professor Aicha Elshabini-Riad for always being there when resources and technical guidance were needed.

The author would also like to extend a special thank you to the Graduate School of Virginia Polytechnic and State University and The College of Engineering Dean's Office for financial support through assistantships during the course of this research.

Appreciation and thanks are given to the Residual Stress Research Group: Marc Tricard, Scott Courtney, Allan Ward III, Robbie Cunningham and Jinmyun Jo for providing technical assistance. Special thanks are also given to Steve McCartney, Mac McCord, and Todd Solberg for their assistance with the many characterization techniques. Without the help of Professor William T. Reynolds, the phase analsysis of alumina would have been incomplete. Professor Reynolds was always available to assist in this effort. I am in great debt to Jan Doran for all the help she provided to me on the administrative side in order to complete my course work and degree requirements. I would also like to thank Dr. Victor Strite for his efforts in reading and editing this thesis.

This thesis is dedicated to both my wife Desiree and mother, Dorothy Venzant. To Desiree who has put up with many long hours that I have worked on this thesis and has given unconditional support to me during the course of the research presented in this thesis. My mother has supported me in whatever I've chosen to do and for this I am thankful. It is because of their love and support and through the guidance of God that I was able to continue and complete this thesis.

# TABLE OF CONTENTS

# LIST OF FIGURES

# LIST OF TABLES

# Chapter 1

# INTRODUCTION

In general, residual stresses arise from regions of heterogeneous plastic deformation following fabrication or processing of materials in some physical manner. Hence, residual stresses are set in a material when it is produced, or when it undergoes some anisotropic plastic deformation in use [1]. Residual stresses are therefore "self-equilibrating internal stresses existing in a free body which has no external forces or constraints acting on its boundary," as defined by Mura [2].

There are numerous situations that cause residual stresses in materials. These stresses are intrinsic to all materials. For ceramics residual stresses play two roles which can be beneficial or deleterious to the ceramic . The compressive stresses in engineering or structural ceramic parts are beneficial, since they are known to retard any small cracks that are created by corrosion or local deformation. Tensile stresses, however, are known to result in fatigue (during cyclic loading) and fracture of the component.

The stress fields generated at the surface of materials are primarily sensitive to x-ray residual stress measurements. Surface stresses are also a potential source of weakness. At the surface, the stress field can aid fast crack propagation, but these stresses can also close or block cracks by squeezing them shut. Tensile stresses tend to be extremely dangerous since they may pull a material apart or open, thus accelerating crack growth and subsequently destroying the part [3].

For ceramic systems, heavy grinding and laser trimming can result in crack growth due to the creation of large tensile stresses. This comes about because of the brittle nature of the ceramics [4]. Residual stresses in ceramic systems may also arise from thermoviscoelastic effects, spatial nonuniformities from thermal expansion effects, phase transformations and

variations in furnace environment variables. More importantly, ceramic materials that are residually stressed as in vapor deposited silicon carbide, may exhibit a time-dependent spontaneous and in some instances explosive fracture at room temperature.

Laser processing of ceramic hybrid microelectronic substrates has almost completely replaced other separation techniques. Because of its short interaction time with the (small heating period), there is no mechanical load and no contamination of the parts as in mechanical techniques. The research discussed herein therefore focuses on the nature of the stress distribution developed in alumina substrates after laser processing and the nature of their phase and chemical composition. The basic properties of the substrates are characterized using a wide range of techniques. The mechanical properties of the alumina are analyzed by X-ray diffraction residual stress and strain gage analysis as a function of laser processing.

Chapter 2 contains a background and review of the subject considered. A general statement of the problem is covered in Chapter 3. The discussion presented there will consider problems encountered in the fabrication of thick film hybrid circuits and provide a statement summary of the work given in this thesis.

Chapter 4 will cover alumina substrate materials characterization such as ESCA (Electron Scattering for Chemical Analysis), EPMA (Electron Probe Microanalysis) and microscopy techniques and various optical microscopy techniques. Phase analysis determination and volume fraction of the phases detected are also presented. X-Ray residual stress and strain gage techniques for stress and strain measurements of the substrates are described. X-ray diffraction residual stress analysis is covered in detail since it was the major technique used in determining residual stresses in the alumina ceramic substrates.

Laser machining systems and laser processing in general utilized in the research presented here is covered in Chapter 5. These laser systems are discussed in relation to their effects on the alumina substrates. Statistics and data analysis techniques are also discussed in Chapter 5 and were used to draw some of the conclusion of the experimental data.

Results and discussion of the experiments are given in Chapter 6 along with detailed

conclusions which considers ramification of the results.

Chapter 7 offers recommendations and outlines future work deemed necessary from the results of the research efforts presented in this thesis.

# Chapter 2

# BACKGROUND AND LITERATURE REVIEW

This section presents a general overview of ceramic properties, ceramics used for microelectronic substrates, origins of residual stresses in ceramics, how ceramics are machined and the residual stresses that may be developed in machined ceramic parts. Principles of x-ray diffraction residual stress analysis are reviewed with the basic theory behind stress-strain relations which is the foundation of the x-ray residual stress analysis. Laser trimming ceramic materials is covered in detail since is was a major part of the experimental work during the course of the research.

## 2.1 Structure–Properties of Ceramics

Ceramic materials receive their interesting but crucial properties after they have undergone some kind of firing sequence. The green or unfired ceramic contains a mixture of milled crystals, binder and plasticizer. Pores are created in the ceramic upon firing due to the evaporation of oils and water. Pores can be made to disappear or shrink due to pressure differentials during the sintering process. Besides their hardness and brittle nature, ceramics have an extremely low resistance to thermal stress. This thermal resistance is the only property known to affect laser machining [5]. More importantly, ceramics are not easily mechanically altered or machined because of the nature of their lattice defects which prevents grain boundary motion. It is also well known that dislocations are hindered from crossing any grain boundaries. This is the exact cause of ceramic breakage and fracture. Breakage or fracture that occur due to some applied force or residual stress occur because ceramics are not ductile as are metals. But some ceramics do have the ability to withstand

high pressures and may be resilient against thermal shock if their coefficient of thermal expansion is low (see below). Fracture has been found to occur along the grain boundaries. Pores are known to reduce the cross section, adversely affecting stiffness. More importantly, contaminants found along the grain boundaries are known to seriously reduce the strength of ceramics [6, 7].

Since the thrust of the research presented here is concerned with the laser trimming of ceramic substrates, it is important to understand their resistance to thermal shock. The resistance of ceramics to sudden temperature changes is found from

$$\Delta T_{max} = \frac{\sigma_z \cdot (1 - \nu)}{E \cdot \alpha} \tag{2.1}$$

This, of course, is assuming that there is a high heat transfer number. $\Delta T_{max}$ represents the maximum temperature obtained without subsequent breakage, $\sigma_z$ is the tensile strength, $\nu$ Poisson's ratio, E is the elastic modulus and $\alpha$ is the coefficient of thermal expansion. If we use the numbers from Table 2.1 for 96% $Al_2O_3$ we will obtain

$$\Delta T_{max} = 65K. \tag{2.2}$$

While this section will consider the current problem with residual stress in ceramics parts in general, a discussion on residual stresses in substrates as found in industry and research laboratories will be given in Chapter 3, "Statement of The Problem." There, discussions will center around past experience with substrate breakage due to residual stresses found in hybrid circuit research at the Hybrid Microelectronics Laboratory at Virginia Polytechnic Institute and State University. Further details on laser machining ceramics are also given to support the "statement of the problem."

Several major electronic materials manufacturers, including Alcoa, Coors, Kyocera and Hitachi, have been faced with the problem of substrate fracture and breakage during fabrication. The problems associated with stress, particularly thermal stress, are crucial because:

1) hybrid microelectronics are faced with the problem of the differences in the coefficient

of thermal expansion among the various packaging materials. In Figure 2.1 we see that there are indeed variations in the coefficient of thermal expansion between the materials as indicated by the histogram plot to the right of the figure,

2) the service condition of the packages becomes severe as increased component density results in a more demanding thermal environment, and

3) product development has been cut short due to the increased need for more accurate and diverse hybrid circuit products and associated applications. The first two conditions create hostile thermal environments for the materials involved, leading to warpage and various crack zones.

There are many papers that discuss determining residual stresses in $Al_2O_3$ caused by grinding [8, 9, 10], but very few report on residual stresses caused by laser damage. There is practically no work done on laser effects as a function of residual stress in ceramic substrates.

For this thesis the main focus is on stress distributions in laser trimmed $Al_2O_3$ substrates, since past work by Schulz et al [11] have shown that the residual stresses do not affect the electrical properties of thick film circuits fabricated on the $Al_2O_3$ substrates.

The literature review surveys papers that report research activities in:

1) structure-properties of ceramics—obtained a general but logical approach of residual stress effects in brittle (ceramic) materials and parts,

2) ceramics used for microelectronic and other applications,

3) alumina—reviewed properties and applications, viz., fabrication sequences, uses and basic material properties,

4) ceramic properties—reviewed structural/engineering ceramics, ceramic composites, ceramic materials design, transformation toughened ceramic systems, and fracture mechanics of ceramics.

5) residual stresses in polycrystalline materials,

6) origin of residual stress in ceramic systems,

7) x-ray diffraction residual stress analysis,

8) instrumentation/measurement and analysis/interpretation—reviewed in order to un-

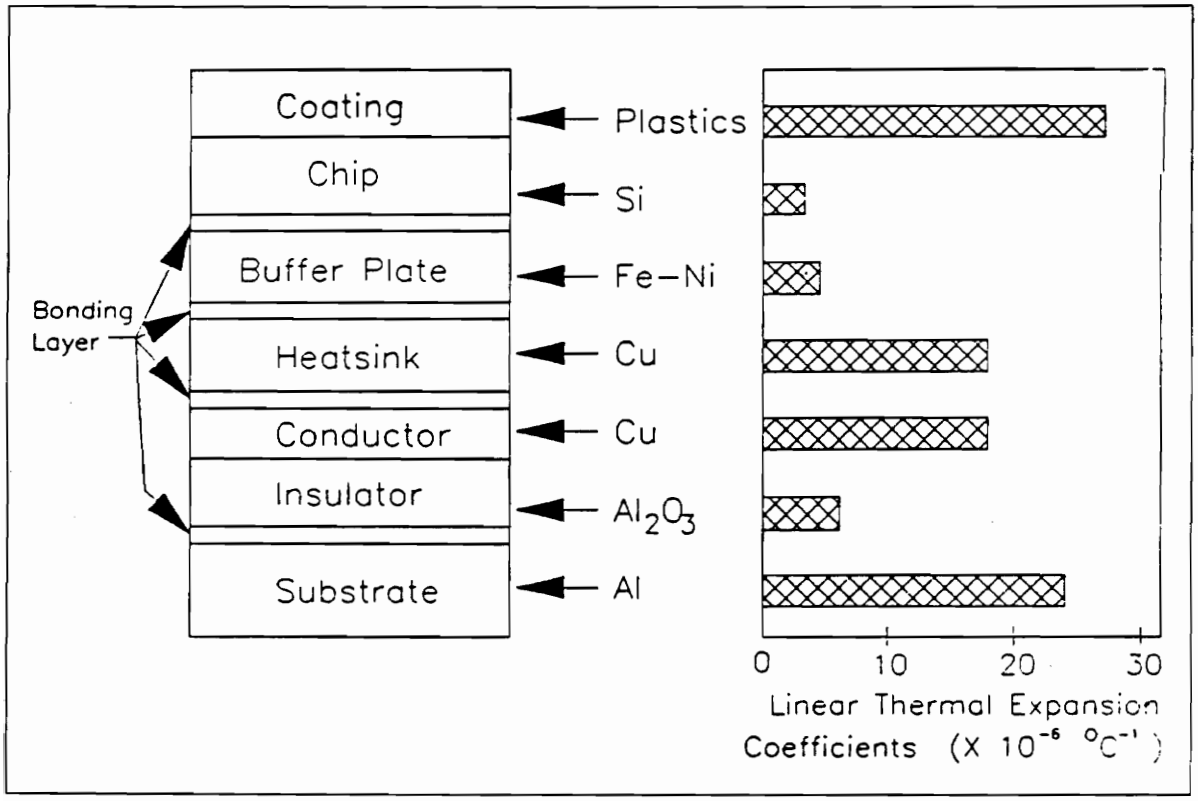


Figure 2.1: Multilayer package example utilized in hybrid technology schemes [12].

derstand measurement errors, to review other systems, and to understand accuracy considerations for residual stress measurements.

9) determination of the X-ray elastic constant for engineered ceramics—pertinent because residual stresses are calculated from X-Ray peak shifts using elasticity relations. Since strain in only one plane is observed, the elastic modulus similarly must be known in that plane.

10) laser-material interactions—this was also critical to review since it involved a major portion of the research presented here.

The above survey was performed to get an accurate account of residual stress effects in brittle materials—primarily ceramic substrates such as $Al_2O_3$—used in microelectronic applications. The next section will explore comparing alumina to other ceramic materials. The discussion is not limited to substrate materials but ceramics in general.

## 2.2 Alumina and Other Ceramic Materials for Microelectronic and Other Applications

Alumina and engineering ceramics for microelectronics applications are explored in lieu of residual stress phenomenology. The review however, is weighted toward ceramic tools, parts and other engineered ceramics since very little work has been done on residual stress in ceramic microelectronic substrates. This review includes general properties of advanced materials under consideration for microelectronic substrates, such as beryllia (BeO), aluminum nitride (AlN), silicon carbide (SiC), mullite ($3Al_2O_3 \cdot 2SiO_2$) and silicon nitride ($Si_3N_4$) as well as the more traditional $Al_2O_3$.

The criteria that are met by the electronics industry for ceramic substrates, specifically the thick and thin film industry, include:

- excellent electrical insulation properties.
- compatability with surface deposited materials, including stability and strength to withstand these components or deposits.

- low dielectric losses.
- resistance to dimensional changes at high firing temperatures, about 1000°C and higher.
- ability to comply with rigid standards for both thick and thin film screen printing or deposition. Both require dimensional tolerances, substrate uniformity and thickness, as well as resistance to bowing or distortion.
- ability to achieve high thermal conduction for maximum power dissipation.
- physical and chemical compatability with the conductor glaze or components (coefficient of thermal expansion (CTE) similarities [13] and resistor composition[1]) in order to achieve strong bonding between the substrate and associated components.
- proper surface roughness (for thick films) or smoothness (for thin films). Rough surfaces affect conductor adhesion; noticeable increased resistor noise is seen with rougher surfaces.
- reproducibility in manufacture so that thick or thin film circuits are not affected by compositional changes [14, 15, 16].

In general, most ceramics are made from a formulation of many raw materials which usually result in uncertain physical properties. However, since the development of high purity oxide ceramics like alumina and beryllia, which meet most of the criteria for electronics packaging applications, a revolution in the electronics industry has occurred. These materials have shown improved electrical performance, mechanical properties, thermal and chemical inertness (resistance to corrosion). Table 2.1 shows some properties of thick film alumina (96% $Al_2O_3$).

[1]This is critical since a circuit design might call for mounting a silicon IC chip on the substrate. This would require that the CTE of the substrate to be 3–4×10⁻6/° C in order to match that of silicon.

### 2.2.1 Alumina

Alumina has been found to meet most of the above requirements and is therefore the most widely used of ceramic substrates. For thick film applications, substrates have alumina contents between 85–97% by weight. These substrates are essentially composed of alpha alumina crystals embedded in a glassy matrix phase. This glassy matrix is composed of calcium and magnesium silicates. The alumina substrates utilized in the work presented here contain about 4% (weight) of a glassy phase and some traces of boron, potassium, and sodium. This 4% glassy phase, essentially an alkaline-earth/aluminosilicate formulation, is utilized in 96% alumina substrates to enhance substrate manufacture since its presence allows for reduced firing temperatures. Holmes and Vest identify other important functions of this glassy phase, including facilitating the bonding process between the metal films and the substrate [17], and diffusional process interactions between the alumina glass phase and the glass phase of the conductor or resistor pastes to create a strong interaction for maximum bonding [15]. According to Southern, a negative effect of the glass phase includes the tendency to reduce thermal conductivity and dielectric strength of alumina [18]. Magnesia is found in most oxides and its presence serves as a grain growth inhibitor [19]. Hoffman [17] reports on a roll–compacted alumina technique that will reduce process firing times, create less flaws in the finished substrate and improve resistor composition [17]. For the most part, the bonding mechanism for alumina and beryllia to metals involves oxidation effects of the manganese forming the glassy phase that in turn diffuses or penetrates the porous molybdenum layer and upon cooling adheres it to the ceramic [14]. More on the composition of the alumina substrates used in this research will be given in Chapter 4, "Alumina Substrate Materials Characterization."

The physical condition of the substrate surface is critical for thick film and thin film circuit fabrication. One must achieve a 3.75 $g/cm^3$ density including a surface finish of about 0.63 $\mu$m, the center line average (CLA); this primarily applies to thick film processing [19]. The CLA is a parameter which indicates how flat the thick film substrates are since

Table 2.1: General properties of thick-film alumina substrates (96% Al2O3)

| Property | Conditions | Test | Property Value |
|---|---|---|---|
| Surface finish (CLA), $\mu$m($\mu$in.) | As-fired | Profilometer 0.762 mm | 0.6(25) |
| flexural strength, MPa(ksi) | 21°C | ASTM F 417 | 400(58) |
| Thermal conductivity, W/m. °C | 20°C | ASTM C 408 | 26 |
| | 100°C | | 20 |
| | 400°C | | 12 |
| Thermal coefficient of | 25 – 200°C | ASTM C 372 | 6.3 |
| expansion, $10^{-6}$/°C | 25 – 500°C | | 7.1 |
| | 25 – 800°C | | 7.6 |
| | 25 – 1000°C | | 8.0 |
| Volume resistivity, $\omega/cm$ | 25°C | ASTM D 1829 | $10^{14}$ |
| | 300°C | | $5.0\times10^{10}$ |
| | 700°C | | $4.0\times10^{7}$ |
| Dielectric constant at | 1 MHz | ASTM | 9.5 |
| 25° C | 100 MHz | | 9.5 |
| Dielectric loss($\tan\delta$) | 1 MHz | ASTM D 150 | 0.0004 |

surface roughness is important in controlling the thick film to substrate interaction during firing. If the surface porosity is not kept within limits, a mechanism known as "flow out"of the glass binder occurs. Many more parameters suffer from a lack of understanding the material. For further explanation see Crossland [19].

Although some discussion is given on newer ceramic substrate materials that may have some improved properties and performance, alumina still represents about 90% of all ceramic substrate sales [20]. Therefore new and better processing conditions and ways to improve processing methodology are warranted for this material. This thesis explores several methods, including processing (laser trimming) and nondestructive evaluation by using X-ray diffraction. Other ceramic materials are considered in the next section because, even though alumina has outstanding properties, these other materials have even superior properties but are currently plagued by processing and fabrication problems in the thin and thick film circuit industry.

Previous work in thick film circuits and associated ceramic substrates performed by Schulz [12, 25, 11] demonstrate the following:

- as received, $Al_2O_3$ substrates are nearly stress free,

- printed and fired substrates showed an average surface residual stress of 7.7 ksi (53 MPa),
- laser cut bare substrates showed residual stresses of about 13 ksi (90 MPa).
- $Al_2O_3$ substrates for thick film applications developed stresses of 15.6 ksi (108 MPa) after laser cutting. These stresses are nearly 40% of the estimated rupture stress, 40 ksi (276 MPa),
- stresses found in the printed and fired substrates were found not to significantly affect the electrical performance of the transmission circuits,

Annealing the ceramic substrates were also explored by Schulz [12]. Discoveries made found that the substrates when annealed at high temperatures, around 1500 °C, showed reduced stress values. Schulz also discovered that the stresses tended to be redistributed in the substrates after annealing.

### 2.2.2 Advanced Ceramic Substrate Materials

**Non Oxides**: Figure 2.2 illustrates some electrical, thermal, and mechanical properties of AlN, SiC and $Si_3N_4$ ceramic substrates [20]. Not much work has been published on SiC or AlN used for hybrid circuit fabrication and laser trimming, primarily because nonoxides are less stable chemically than alumina [22]. For instance, from results of X-ray photoelectron spectroscopy (XPS), degradation of AlN occurs due to laser irradiation, which results in the formation of free Al. This occurs because of the AlN being transformed into $Al_2O_3$ [22].

**Oxides**: Mullite is another refractory material that can achieve requirements for high-speed device applications as reported by Horiuchi et al [23]. Mullite is a traditional refractory ceramic; its properties have been improved beyond alumina's through the use of sol-gel processing efforts [23]. Furthermore, mullite processed with more uniform particle sizes results in improved sintering behavior, with CTEs comparable to silicon. Mullite is an important ceramic simply because of its uses in some applications that preclude alumina.

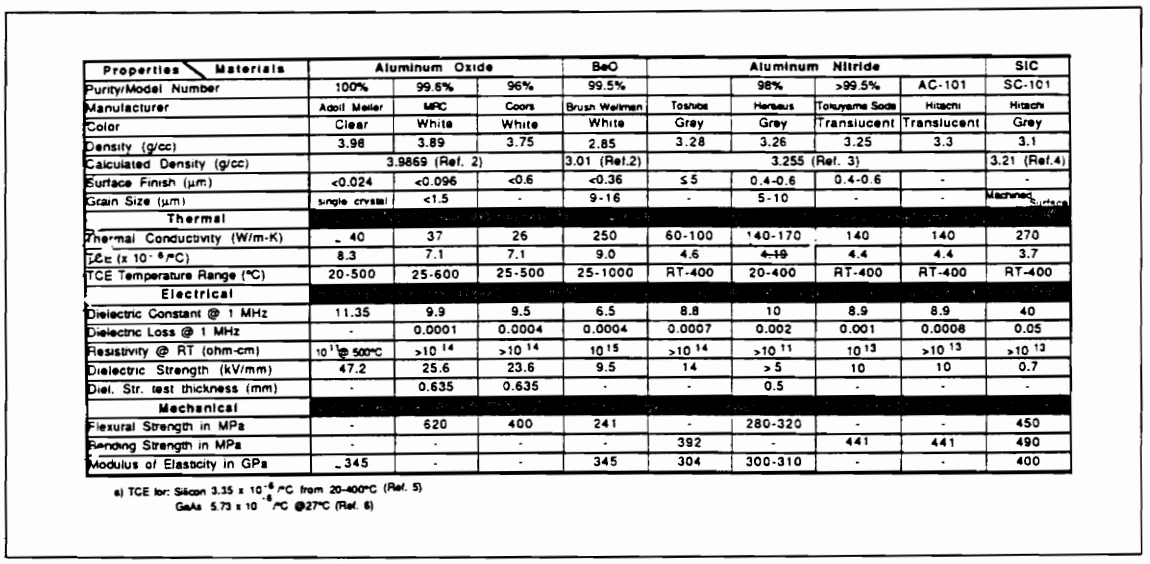

| Properties \ Materials | Aluminum Oxide | | | BeO | Aluminum Nitride | | | | SiC |
|---|---|---|---|---|---|---|---|---|---|
| Purity/Model Number | 100% | 99.6% | 96% | 99.5% | | 98% | >99.5% | AC-101 | SC-101 |
| Manufacturer | Adoll Meller | MRC | Coors | Brush Wellman | Toshiba | Herseus | Tokuyama Soda | Hitachi | Hitachi |
| Color | Clear | White | White | White | Grey | Grey | Translucent | Translucent | Grey |
| Density (g/cc) | 3.98 | 3.89 | 3.75 | 2.85 | 3.28 | 3.26 | 3.25 | 3.3 | 3.1 |
| Calculated Density (g/cc) | 3.9869 (Ref. 2) | | | 3.01 (Ref.2) | 3.255 (Ref. 3) | | | | 3.21 (Ref.4) |
| Surface Finish (μm) | <0.024 | <0.096 | <0.6 | <0.36 | ≤5 | 0.4-0.6 | 0.4-0.6 | - | - |
| Grain Size (μm) | single crystal | <1.5 | - | 9-16 | - | 5-10 | - | - | Machined Surface |
| **Thermal** | | | | | | | | | |
| Thermal Conductivity (W/m-K) | ~ 40 | 37 | 26 | 250 | 60-100 | 140-170 | 140 | 140 | 270 |
| CTE (x $10^{-6}$/°C) | 8.3 | 7.1 | 7.1 | 9.0 | 4.6 | 4-19 | 4.4 | 4.4 | 3.7 |
| TCE Temperature Range (°C) | 20-500 | 25-600 | 25-500 | 25-1000 | RT-400 | 20-400 | RT-400 | RT-400 | RT-400 |
| **Electrical** | | | | | | | | | |
| Dielectric Constant @ 1 MHz | 11.35 | 9.9 | 9.5 | 6.5 | 8.8 | 10 | 8.9 | 8.9 | 40 |
| Dielectric Loss @ 1 MHz | - | 0.0001 | 0.0004 | 0.0004 | 0.0007 | 0.002 | 0.001 | 0.0008 | 0.05 |
| Resistivity @ RT (ohm-cm) | $10^{15}$ @ 500°C | $>10^{14}$ | $>10^{14}$ | $10^{15}$ | $>10^{14}$ | $>10^{11}$ | $10^{13}$ | $>10^{13}$ | $>10^{13}$ |
| Dielectric Strength (kV/mm) | 47.2 | 25.6 | 23.6 | 9.5 | 14 | > 5 | 10 | 10 | 0.7 |
| Diel. Str. test thickness (mm) | - | 0.635 | 0.635 | - | - | 0.5 | - | - | - |
| **Mechanical** | | | | | | | | | |
| Flexural Strength in MPa | - | 620 | 400 | 241 | - | 280-320 | - | - | 450 |
| Bending Strength in MPa | - | - | - | - | 392 | - | 441 | 441 | 490 |
| Modulus of Elasticity in GPa | ~345 | - | - | 345 | 304 | 300-310 | - | - | 400 |

a) TCE for: Silicon 3.35 x $10^{-6}$/°C from 20-400°C (Ref. 5)
GaAs 5.73 x $10^{-6}$/°C @27°C (Ref. 6)

Figure 2.2: Electrical, thermal and mechanical properties of standard and new substrate materials.

Table 2.2: Properties of 99% beryllia (BeO)

| | |
|---|---|
| Density, $g/cm^3$ | 2.85 |
| Flexural strength, MPa(ksi) | 241(35) |
| Thermal Expansion, $10^6$ 25°$C$ to: 200°$C$ | 6.4 |
| 500°$C$ | 7.2 |
| Thermal conductivity. W/m·°$C$ W/m, °$C$ | 130 – 200 |
| Dielectric constant at 1 MHz | 8.6 – 9.0 |
| Dielectric loss at 1 MHz | 0.001 |

For instance, mullite can be used in silicon chip applications because of its CTE value of $4.5\times10^{-6}$/°C closely matches that of a silicon chip (the CTE for silicon is $3.35\times10^{-6}$ [24, 23]. Table 2.3 illustrates some characteristics of mullite.

Since residual stresses are a primary concern in the work presented here, the next section will cover the origin of residual stresses materials in general. Efforts in residual stress work in machined engineering ceramics in general are covered along with associated residual stresses and residual stresses in ceramic parts. Various types of stresses found within materials are considered and finally a section on laser trimming will conclude the chapter since it is a

Table 2.3: Mullite ceramic characteristics in comparison to 92 wt% alumina

| Characteristics | New Mullite M1 | M2 | M3 | MS1 | MS2 | 92%wt Alumina |
|---|---|---|---|---|---|---|
| Dielectric-constant (1MHz) | 7.3 | 7.5 | 7.3 | 5.9 | 5.7 | 9.4 |
| Dissipation factor($\times 10^{-4}$, 1MHz) | 15 | 15 | 15 | 31 | 35 | 5 |
| Insulation resistivity ($\Omega$-cm) | $> 10^{14}$ | $10^{14}$ | $10^{14}$ | $10^{14}$ | $10^{14}$ | $10^{12}$ |
| CTE ($\times 10^{-6}/°C$) | 4.5 | – | 4.5 | 3.8 | 3.4 | 7.2 |
| Flexural Strength ($kg/mm^2$) | 20 | 23 | 31 | 30 | 22 | $28 - 35$ |
| Surface roughness ($\mu$m) | 0.5 | 0.5 | 0.2 | 0.3 | $0.5 \sim 0.8$ | |

major part of this thesis.

## 2.3 Origin of Residual Stresses in Ceramic Systems and Parts

In the introduction it was discussed that residual stress can be both beneficial and harmful to materials. Noyan and Cohen give an excellent review on residual stresses in metals and ceramics in reference [26].

Residual stresses may be divided into two categories: micro-residual stresses and macro-residual stresses. Micro-residual stresses are found in the different phases of materials, while macro-residual stresses may be measured across the bulk material. Residual stresses of the first and second kind may be classified as macroresidual stresses (because these stresses operate over more than one grain), while residual stresses of the third kind (which operate over a single grain) are classified as micro-residual stresses.

When materials are fabricated by processes which involve high temperatures, such as laser trimming of ceramic substrates, large tensile stresses are found to develop in the material due to non-uniform cooling (with attendant shrinkage) [12, 27]. Laser trimming and cutting will be treated in more detail in Section 2.5.1. Compressive stresses may also develop. For some materials, especially ceramics, stresses are found to develop from shipping or storage. More importantly, fatigue-type failures can develop during temperature cycling under normal operation [25].

Lin and Ericsson found that compressive stresses occur for steel in both parallel and

perpendicular directions in the layer of the laser-hardened material. Tensile stresses were discovered in the surface and depth layer following laser tempering [28]. They also found stresses in large heat-affected zones of their samples due to the major differences in the heating and cooling rates of the different layers of the substrate. Laser trimming of ceramic substrates results in very small heat-affected zones; therefore, the amount of residual stresses in the entire substrate may be small [29].

Structural and engineering ceramics used in today's technology-driven markets have many advantages over conventional and some advanced materials due to low density, high strength and hardness, low heat expansion, good heat conductivity, high thermal stabilization, and oxidation resistance. However, since ceramics are brittle due to their covalent/ionic bonding mechanism, nondestructive quality control is crucial throughout the manufacturing process as reported by Goebble [4]. Goebble also reports on different nondestructive evaluation techniques and the importance of knowledge of material parameters.

From the results of current research efforts as reported by Goebble, defects down to less than 100$\mu$m will generally result in failure when loads of up to 43.5 ksi (300 MPa) are applied to polycrystalline materials. This, however, will depend on the type of defect. More importantly, four point bending experiments with reaction bonded silicon nitride have found that loads of 200 MPa (29 ksi) were shown to cause failures at surface defects of $\geq$ 15$\mu$m [30]. Therefore, for nondestructive evaluations of ceramic parts and components, it is important to know what types of defects, microstructure, and stresses are present in the ceramic material during manufacturing sequences. From a microstructural aspect, the investigator must be familiar with grain size, grain site distribution, porosity (pore size, pore site distribution) and percentage.

### 2.3.1 Machining Engineering Ceramics

Ceramics are machined in a variety of ways: grinding, cutting, drilling, breaking with scoring, sandblasting, or laser trimming. Although the methods presented have their differences, each share the common principle of producing one or more cracks nucleated within

the material which may traverse the sample until it is separated into larger or smaller pieces [31]. The new separated crack surface is seen as a continuous fracture surface, or is composed of many small fracture surfaces [31]. This will be discussed further in Chapter 6, as it plays a crucial role in laser trimming.

Fractures in brittle materials are classified into two types: intrinsic (flaws introduced during material formation) and extrinsic (flaws that are stress induced due to some form of machining). The intrinsic flaws are predominantly voids or inclusions, whereas the extrinsic flaws are microcracks which result from residual stresses [32].

Crack nucleation resulting from a laser beam when concentrated at point to obtain high power density will cause a small contact area to form. At this point, high compressive stresses are initially created which propagate toward the interior of the material, finally transforming to tensile stresses at some distance under the surface being heated (this occurs upon cooling). Furthermore, shear stresses are known to be present throughout the contact region. Fracture—created degradation, and sometimes single microcracks may result in a total failure in the overall material system [31]. Furthermore, only a small number of atoms will arrive at new positions of equilibrium due to irreversible distortions brought about by laser machining. This irreversible damage may be caused by increased force of penetration by the indenter or laser beam. If defects are not present, regions that have the initial contacts will increase and deformations in microvolumes develop and hence the creation of plastic or viscous flow behavior.

Another crucial factor which may have some bearing in the work presented here is that cracks may form at some point after the part has been unloaded. According to Mencik [31], as the surface of the ceramic is being breached, plastic deformation as well as damage occurs immediately below the surface. But at the same instant, the indenter or laser creates large compressive stresses at the region of contact, thereby preventing atomic displacements. Once the force is removed, tensile stresses formed under the surface by the elastically distorted surface region will produce cracks (one or more), as there are no compressive forces available.

### 2.3.2 Residual Stresses in Engineering Ceramics

According to Johnson-Wallis et al. [10], the origin of residual stresses in ceramics and other materials is primarily due to machining by mechanical means such as grinding, laser, ultrasonics, etc. The basic effect of machining results in an accumulation of a gamut of "isolated" sharp particle contact events [10]. In early abrasion studies, it was considered that residual stresses arose from fracture interface debris which tended to halt crack healing mechanisms formed by the abrasion. However, recent investigations stipulate that machining which produces localized contacts and abrasion will result in irreversible deformation [32]. Different interpretations exist for the case of fracture in machining. It has therefore been concluded by investigators that an isolated elastic/plastic region was found to generate a radially compressive residual stress field. This stress field has a tangential tensile nature which is clear of the plastic zone surrounding the initial contact site [33]. Furthermore, additional strength—degrading cracks are found to form on median planes within the tensile field [33].

Sometimes residual stress fields overlap because of neighboring damage sites in a machined ceramic surface. This overlapping causes a layer of residual compressive stress. However, this compression tends to reduce the residual tension effects which in turn act on the strength controlling flaw [10].

In most cases, ceramics machined by grinding and polishing were found to contain compressive residual stresses. Eigenmann et al. [34] found that machined ceramic surfaces (SiC, $Al_2O_3$, and $Si_3N_4$) that were ground, lapped, spark eroded, and cut had steep near—surface compressive residual stress gradients [34]. They also discovered residual stresses after unloading, when loading under bending-creep-conditions using high temperatures caused inhomogeneous plastic deformation; they also report on residual stresses in surfaces treated by diffusion processes [34].

Residual stresses resulting from machining damage (grinding, polishing, laser trimming) is understood to be due to the accumulation of many isolated sharp particle contact reactions

[10]. Recent results reported by Johnson-Wallis state that localized contacts due to abrasion and machining can cause irreversible deformation and fracture are a result of the following considerations:

- there is an isolated elastic/plastic contact creating a compressive field that is radial in direction.
- this compressive field has tangential tension found outside the plastic zone surrounding the contact site.
- cracks that are known to degrade strength form median planes within the tensile field.
- the overlapping of residual stress fields created from neighboring damage sites results in the overall residual compressive field layers.
- it has been determined that this compressive field does not eradicate residual tensions which are known to act on the strength-controlling flaw [10].

Essentially, residual and applied stresses define the localized stress state. Surface finishing from machining components can result in residual stresses that may reduce the strength of a part by as much as 40%, as reported by Marshall [33].

In general due to the high hardness of ceramics, the layers that are usually affected by residual stresses after machining are very near the surface. Since these stresses reside near the surface, X-ray diffraction residual stress analysis is the method of choice to detect the surface stresses. For bulk materials, careful lapping of the ceramic part is performed. This allows for the X-ray residual stress measurements to be performed on a new surface.

Overall, X-ray residual stress applied to ceramics is difficult compared to metals, since ceramics are less sensitive to X-ray diffraction. Careful analysis of data generated from ceramic parts must be performed since the data are usually hard to interpret.

When ceramic parts are machined surface compressive stresses are generated. In some circumstances, as reported by Johnson-Wallis et al. [10] residual compressive stresses were

found to cause severe buckling due to diamond grinding. They also discovered an underlying tensile stress layer near the strength-controlling damage.

There is currently not much literature on the subject of stress in ceramic microelectronic substrates. The next section will cover work performed by the Residual Stress Group at Virginia Tech.

### 2.3.3 Stresses in Ceramic Microelectronic Substrates

Stresses that develop in the substrates can be linked to processing history from start to finish. Therefore the stresses developed in ceramics and ceramic substrates are superpositions. For instance the total stress in a can be represented by:

$$\sigma^{RS} = \sigma^{RS,I} + \sigma^{RS,II} + \sigma^{RS,III} \tag{2.3}$$

where residual stresses (RS) I, II, and III are the stresses of the first, second and third kind. Residual stresses of the first kind are those stresses that setup in a material covering several grains. They are created from processing that cause inhomogeneously distributed plastic changes on the dimensions of the work piece. Residual stresses of the second kind result from elastic anisotropy due to the different phases having varying thermal expansion coefficients. Finally residual stresses of the third kind act at short ranges within the and equilibrate in the material over small distances. Generally these are stress fields centering around dislocations or point lattice defects [34, 35]. In the alumina substrate there is also a CTE mismatch between the matrix and precipitate phases, resulting in intrinsic or residual stresses.

## 2.4 Measurement of Residual Stresses

There are four techniques (mechanical, diffraction, acoustic, and magnetic) that allow for the determination of the superposition of various loading stresses and residual stresses in most materials. These stresses can be determined using sophisticated experiments and

theoretical stress analysis procedures. In general, depending on the nature of the residual stress and the material, the stress state may be determined from:

- the mechanical release of large strains or macrostrains from the , recorded via strain gages (e.g., hole drilling, in which stress is measured by the change in the local strain). This sort of testing is destructive, however.
- the displacement or lack thereof of lattice strain processes. X-ray and neutron diffraction experiments and procedures are used in these residual stresses measurement methods.
- the effects of intrinsic physical structure properties of the material itself as in ultrasonic stress analysis in which stresses are determined from differences in shear wave time of flights.
- another intrinsic detection technique is by magnetic methods, viz., Barkhausen "noise" analysis (BNA), which can be used only in ferromagnetic materials [35, 36].

All of the above techniques except diffraction are indirect methods to measure residual stresses. X-ray and neutron diffraction techniques, however, are direct means of measuring residual strain in materials. These two methods measure the lattice spacing displacements by shifts in diffraction peaks—these are directly proportional to homogeneous lattice strains in the direction of workpiece rotation (measured in terms of tilt angle $\psi$) and are nondestructive. X-ray residual stress stress analysis (XRRSA) is limited to the measurement of surface stresses. This is a result of common X-ray wavelengths having small penetration depths in most crystalline materials. From biaxial elasticity theory, any residual stress of the first kind (residual stresses occurring in macroscopic dimensions) results from strains which are found to be linearly dependent on $\sin^2\psi$ in every angular distance of the relating stress or deformation ellipsoid [35]. More will be discussed regarding this $\sin^2\psi$ technique in the following section.

### 2.4.1 X-ray Determination of Residual Stress

This section will explore measurement procedures of x-ray residual stress analysis along with the associated stress strain relations and introduce the $\sin^2\psi$ technique of measuring residual stress.

The d-spacings (distances between a given crystallographic plane) are obtained from Bragg's Law, which is given by:

$$n\lambda = 2d_{hkl}\sin\theta \tag{2.4}$$

where $\lambda$ is the incident radiation, n is an integer multiple of the radiation wavelength, $d_{hkl}$ is the distance between the planes of Miller indices (hkl), and $\theta$ is the angle of incidence of the X-rays to the (hkl) planes. Figure 2.3 illustrates this behavior or scattering. This figure shows a cubic cell diffracting X-Ray photons (note the geometrical illustration of the parameters involved showing how the waves constructively interfere). Cullity [37] states that "a diffracted beam may be defined as a beam composed of a large number of scattered rays mutually reinforcing one another." For a known incident radiation and sample crystal structure, diffraction planes can be found and d-spacings or lattice displacements can be calculated. Furthermore, these different grains will result in diffraction peaks that are slightly displaced from the previous measurement. By differentiating Bragg's law, we find

$$d\lambda = 0 = (-2d\cos\theta + 2\delta d\sin\theta), \tag{2.5}$$

or

$$\frac{\delta d}{d} = \frac{\delta\theta}{\tan\theta}. \tag{2.6}$$

Thus, for a given error $\delta\theta$, the error in d-spacing is minimized if measurements are made at high angles. In effect, the d-spacing decreases with the tilt while the angle $2\theta$ increases.

In x-ray residual stress analysis (XRRSA), diffraction peaks are obtained by tilting the substrate across a range of orientation angles $\psi$, while keeping $2\theta$ fixed. This is shown in Fig-

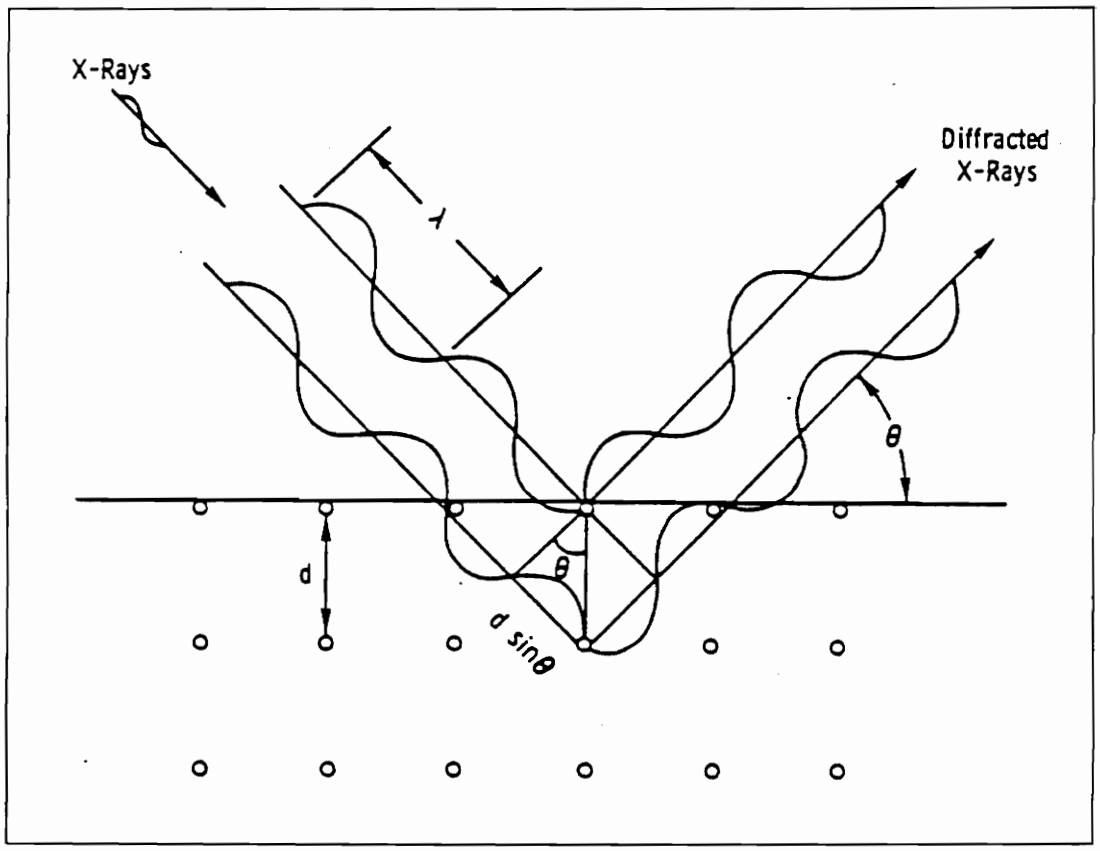


Figure 2.3: Illustration and derivation of Bragg's Law [38].

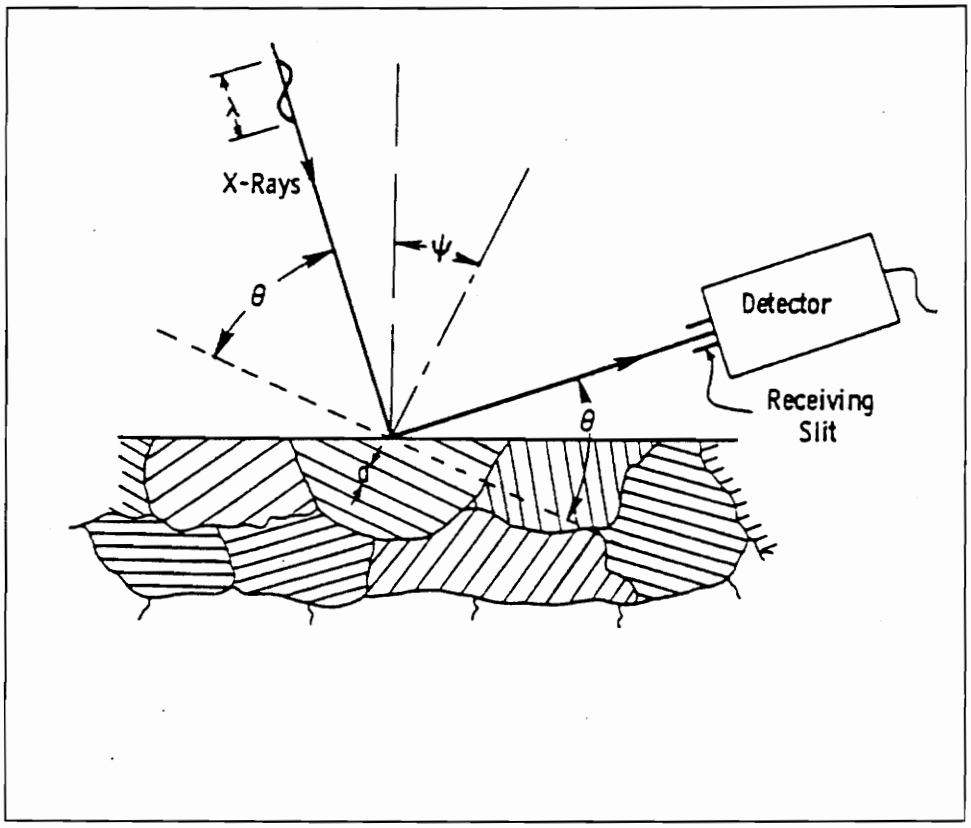


Figure 2.4: Atomic plane schematic in grains oriented for X-ray diffraction [38].

ure 2.4. The optimum grain size which should result in better statistics for polycrystalline materials is about 10–50 $\mu$m [38].

Residual stresses are measured to be compressive or tensile, depending on the shift in diffraction peaks. For the large values of $2\theta$ employed in XRRSA, a peak shift to lower $2\theta$ values indicates widely spaced planes in the direction of the diffraction vector, and thus compressive stresses in the plane of the material. Figure 2.5 illustrates this by showing the effect of residual stress on the $2\theta$ Bragg angle diffraction (or position).

From Figure 2.5, $d_0$ represents the initial stress-free condition (no stress, no atomic displacements) which is increased when the atoms move from $d_0$ to $d_1$ (final stress state) representing the application of an applied tensile stress—the atoms being pulled apart. This case is representative of a $\theta$ increase as defined by Bragg's law.

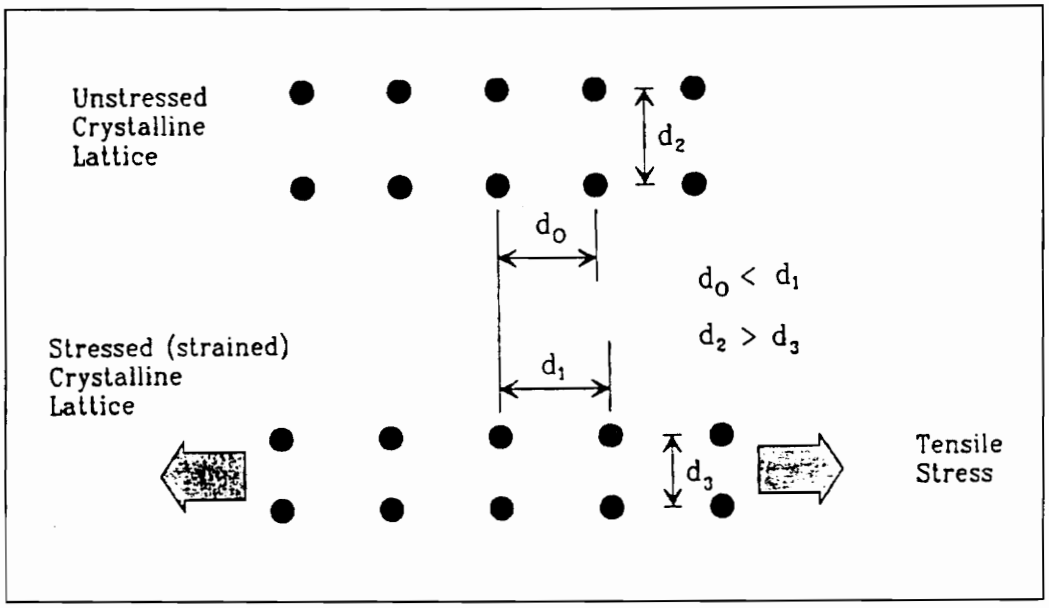


Figure 2.5: Effect of residual stress on the displacements of atoms and the $2\theta$ Bragg angle [12].

Figure 2.6 illustrates what will happen when a position—sensitive detector (as in our case) is moved over several $2\theta$ angles in order to locate the angle of maximum diffraction from grains that satisfy Bragg's Law. Diffraction occurs only for those (hkl) planes that are perpendicular to **k**; **k** bisects the incident and diffracted beam. Figure 2.6 also shows what happens after new grains are diffracted when the specimen is tilted with respect to the incident wavelength or diffraction vector. Here the orientation of the diffraction planes are almost perpendicular to the diffraction direction.

Furthermore, these different grains will result in diffraction peaks that are slightly displaced from the previous measurement increases, as shown in Figure 2.6 [26].

### 2.4.2 Stress-Strain Relations

The X-ray diffraction technique is really measuring strain and not the stress. Therefore, the interplanar spacings, $d_{\phi,\psi}$, or d-spacings are serving as an internal strain gage. For the case presented here, strain is related to the d-spacing difference divided by the unstressed

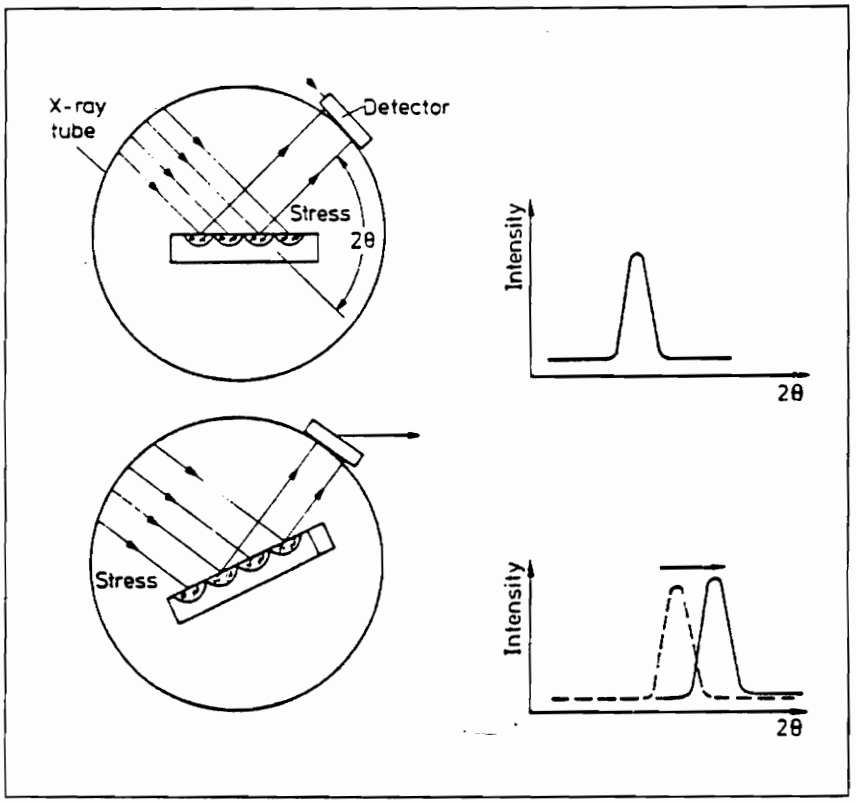


Figure 2.6: Diffraction after the sample is tilted, viz., diffraction occurs in the same planes but with different grains [26].

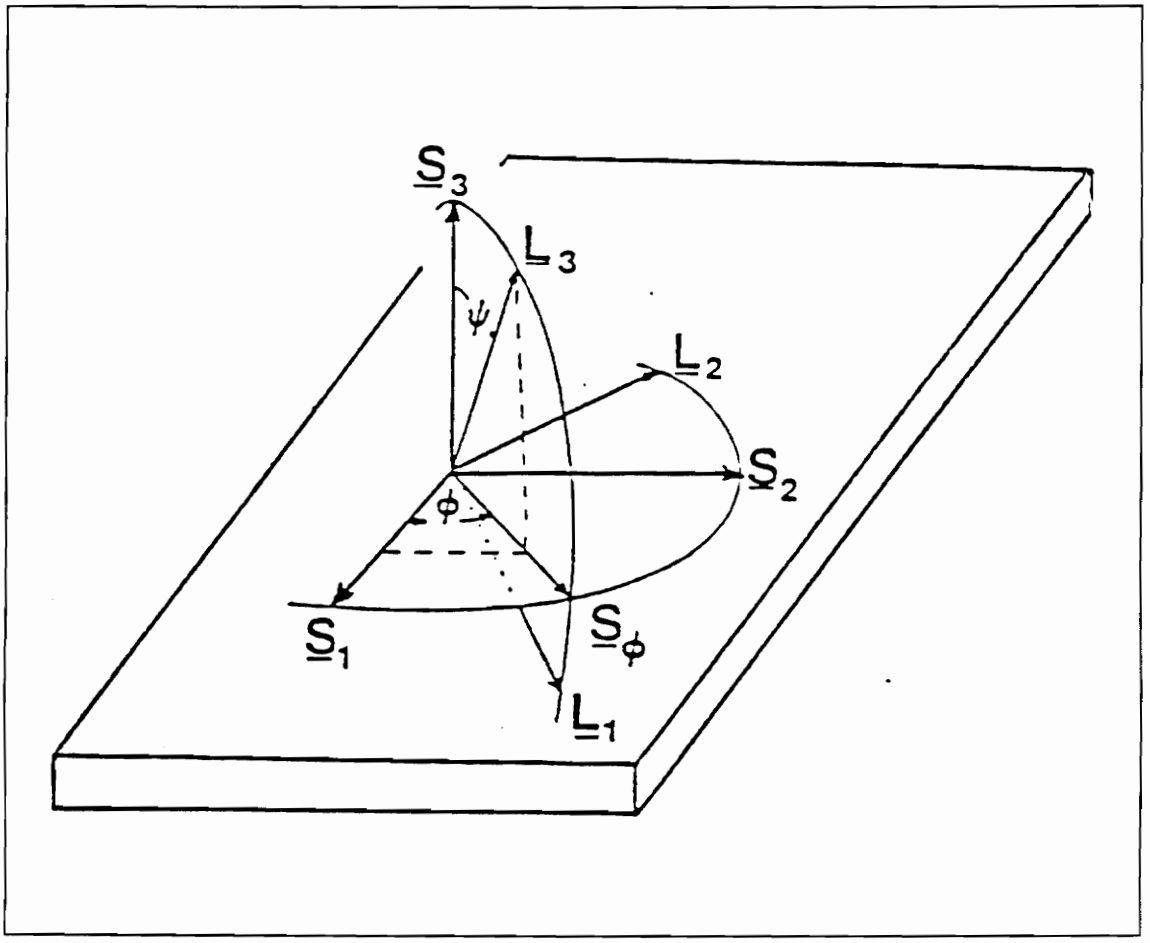


Figure 2.7: Sample coordinate system of the $\psi$ diffractometer showing laboratory $L_i$, sample $S_i$ coordinates, and the $\phi$, $\psi$ angular relationships [12].

lattice spacing

$$(\epsilon'_{33}) = \frac{d_{\phi,\psi} - d_0}{d_0} \tag{2.7}$$

Equation 2.7 represents the case for one dimensional strain. The geometry for x-ray diffraction measurements is illustrated in the three dimensional system in Figure 2.7.

In Figure 2.7 $\underline{S_i}$ and $\underline{L_i}$ define the two coordinate systems utilized in the X-ray residual stress measurements. $\underline{S_i}$ represents the sample's surface and is defined by $S_1$ and $S_2$. $\underline{L_i}$, the laboratory system defined by $L_3$ acting normal to the hkl planes in which the d-spacings

are determined by X-rays. Finally, $L_2$ is located in the planes that defines the orthogonal coordinates $S_1$ and $S_2$ making an angle $\phi$ with $S_2$.

We expand on the relationships between stress and strain by following the stress-strain equations of continuity as developed by Dölle which are given below. Equation 2.8 illustrates the relationship found between the d-spacing change of a crystallographic plane and a triaxial stress field. This stress field is determined from a Cartesian coordinate system transformation law, Hooke's law and the strain-deformation relationship, viz.,

$$\begin{aligned}(\epsilon'_{33})_{\phi,\psi} = \frac{d_{\phi,\psi} - d_0}{d_0} &= \epsilon_{11}\cos^2\phi\sin^2\psi + \epsilon_{12}\sin 2\phi\sin^2\psi \\ &\quad + \epsilon_{22}\sin^2\phi\sin^2\psi + \epsilon_{33}\cos^2\psi \\ &\quad + \epsilon_{13}\cos\phi\sin 2\psi + \epsilon_{23}sin\phi\sin 2\psi \\ &= \frac{1+\nu}{E}\left(\sigma_{11}\cos^2\phi + \sigma_{12}\sin 2\phi + \sigma_{22}\sin^2\phi - \sigma_{33}\right)\sin^2\psi \\ &\quad + \frac{1+\nu}{E}\sigma_{33} - \frac{\nu}{E}(\sigma_{11}+\sigma_{22}+\sigma_{33}) \\ &\quad + \frac{1+\nu}{E}(\sigma_{13}\cos\phi + \sigma 23\sin\phi)\cdot\sin 2\psi. \end{aligned} \tag{2.8}$$

As before, $d_0$ is the d-spacing of the (hkl) plane in the unstressed material and $d_{\phi,\psi}$ is the d-spacing parameter of the measurement plane which is oriented normal to the sample coordinate system (see Figure 2.7). The applied residual stress tensor is represented by the $\sigma_{ij}$ components; the X-ray elastic constants of the material are represented by $(1+\nu)/E_{hkl}$ and $\nu/E_{hkl}$, where $E_{hkl}$ is Young's modulus and $\nu$ is Poisson's ratio. These constants are applied in the residual stress analysis since they follow Hooke's law and relate the internal strains ($\epsilon$) to the stress values. However, as mentioned previously, these constants are different for each crystallographic orientation. Therefore the X-ray elastic constant should be determined experimentally for the material under study.

Equation 2.8 shows the relationship for a triaxial applied field of stress. If the stress field is biaxial, then the stress components $\sigma_{ij}$ =0 for i or j =3. For this case, Equation 2.8 becomes

$$\frac{d_{\phi,\psi} - d_0}{d_0} = \frac{1+\nu}{E}\left(\sigma_{11}\cos^2\phi + \sigma_{12}\sin 2\phi + \sigma_{22}\sin^2\phi\right)\sin^2\psi + \frac{\nu}{E}(\sigma_{11} + \sigma_{22}) \qquad (2.9)$$

This equation can be further reduced if the first bracket is set equal to $\sigma_\phi$, which is the stress in the $\phi$ direction, and since when $\psi = 0$, we have

$$\frac{d_{\phi,0} - d_0}{d_0} = \frac{\nu}{E}(\sigma_{11} + \sigma_{22}) \qquad (2.10)$$

A reduction of this equation generates a final form

$$\frac{d_{\phi,\psi} - d_{\phi,0}}{d_0} = \frac{1+\nu}{E}\sigma_\phi \sin^2\psi. \qquad (2.11)$$

This final form predicts a linear relationship between d and $\sin^2\psi$ if a biaxial stress field exists; the slope of the line would be $(1+\nu/E)\,\sigma_\phi$. The slope, $\sigma_\phi$ of equation 2.11 is the residual stress determined from the irradiated material volume. Two $\psi$ tilt angles are sufficient to determine the residual stress only if the material is in a biaxial stress state and all underlying elasticity and optics assumptions are valid. A biaxial stress approximation assumes no shear stress and therefore, the biaxial approximation is incorrect when applied (i.e., when shear stresses exist) to materials showing preferred orientation, texture, or even shear stress.

### 2.4.3 Shear Stress Analysis of X-ray Residual Stress Measurements

For work in x-ray residual stress analysis careful interpretation of the data is crucial. In the $\sin^2\psi$ technique there are a variety of deviations from a linear d versus $\sin^2\psi$ plot. These deviations or non-linearities may be due to texture, preferred orientation, shear stresses, grain size effects, etc. Various examples of nonlinearities are illustrated in Figure 2.8 [41]. If nonlinearities in the data are encountered the biaxial stress analysis will be invalid and a triaxial stress analysis will be in order.

In general, the biaxial model assumes an equation of the form $d = A + B\sin^2\psi$ for fitting the data to stresses acting biaxially. Since the model fails when nonlinearities are

encountered, the shear stress model is considered and has the form d = A + B $\sin^2\psi$ + C $\sin 2\psi$. The extra term in this equation, C $\sin 2\psi$, represents the shear component of the general residual stress equation. The B term (the normal component in stress analysis) is related to the slope and is determined from the multiply regressed data. The shear stress equation defines an ellipse and the B term determines whether $\psi$ splitting will have a positive or negative slope. The constants A, B, and C in comparison with equations 2.9, 2.10, 2.11, shows that

$$A = d_0 + d_0\left[\frac{1+\nu}{E}\sigma_{33} - \frac{\nu}{E}(\sigma_{11}+\sigma_{22}+\sigma_{33})\right] \tag{2.12}$$

$$B = d_0\frac{1+\nu}{E}(\sigma_{11}-\sigma_{33}) \tag{2.13}$$

and

$$C = d_0\frac{1+\nu}{E}\sigma_{13} \tag{2.14}$$

where all variables have been defined above. If it is assumed that the shear stress model fits the data and the biaxial model doesn't, we expect the shear model to be the best fit to the data in most cases compared to the biaxial case. This can be determined by examining standard statistical t, F and R values as will be discussed in Chapter 4.

## 2.5 Laser-Material Interactions

To understand the laser-material interaction, a brief explanation is given below. In general, lasers have three distinct modes of operation: normal mode (pulse length) operating in the millisecond range, Q-switched mode operating in the shorter nanosecond range, and the continuous wave mode or cw. The pulsed mode and Q-switched mode lasers are generally more suitable for laser trimming/scribing, drilling or cutting ceramic, wafers, and metals [55].

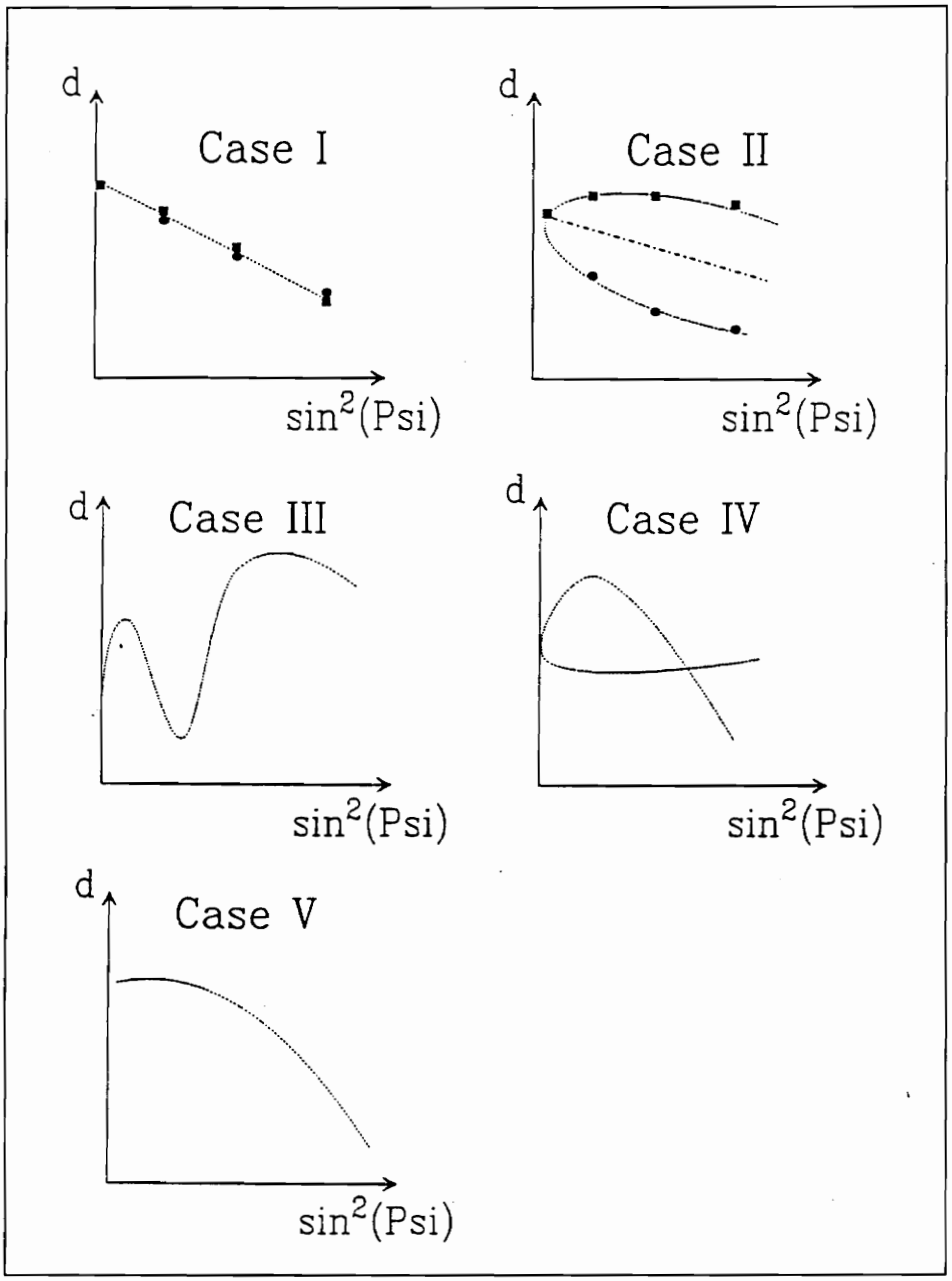


Figure 2.8: Non-linearities in various d-versus $\sin^2\psi$ plots [41]. Case I represents a biaxial stress condition (compressive), Case II a shear stress condition (psi-splitting), Case III is indicative of oscillations in the data (preferred orientation and grain size effects), Case IV involves geometrical errors, and finally Case V indicates that the material may contain a stress gradient perpendicular to the materials surface.

Laser applications for industrial use for materials processing are categorized into two groups: (1) applications requiring a controlled amount of laser energy such as micromachining, resistor trimming, substrate trimming/scribing and semiconductor annealing; and (2) applications wherein a large amount of heat or energy is imparted to the sample in order to bring about the necessary phase transformation in the sample for cutting, welding and other processes.

To laser process a material, the following must be taken into account: laser beam characteristics, material properties (optical, thermal, surface region), and energy transfer optimization, viz., the heat conduction, absorption capacity, and rate. Soarez and Perez-Amor [55] recommend that the following items should guide careful laser–material interaction applications:

- the creation of a highly intense initial pulse to circumvent any surface reflectivities.
- adjustment of power density and the duration of the pulses to give optimum conditions for laser heating or melting (vaporization).
- understanding of the lateral dimensions of the area being processed. The spot size (usually a micron sized region) is dependent on this process.
- the beam width and pulse controls the depth of interaction, which is dependent on the heat conductivity and material removal rates.

Finally, the incident energy absorbed is given by:

$$I(z) = I_0 e^{-\alpha z} \tag{2.15}$$

This is Lambert's law where I(z) is the radiation intensity at a depth z, and $\alpha$ is the absorption coefficient.

### 2.5.1 Laser Trimming Alumina And Other Ceramic Materials

The primary purpose of laser machining ceramic materials is to create localized damage by penetrating the surface with an intense collimated beam of energy at some diffraction limited point. This is done to control the propagation of a single crack. The laser is simply nucleating cracks for crack propagation [31, 42, 43]. The laser's output and its working region must be chosen so that the ceramic characteristic wavelength $\lambda$ is opaque to it.

Scribing or trimming ceramic materials is similar to vaporization. For trimming purposes, a blind cut is performed on the material to serve as a stress raiser. This is done to enable the material to be mechanically snapped along the trimmed lines. The method or strategy used in trimming ceramics is to create a small heat affected zone with as little surface debris as possible. Small HAZs must be created since laser machining will generate high residual stress effects which are detrimental to the workpiece [29]. Furthermore, ceramics are prone to failure when tensile stresses are created [7].

When laser processing ceramic materials, one must consider the critical temperature cycle of laser processing. This temperature cycle is defined by external stress, geometric configurations, and the characteristics of the material itself [29]. The external stresses are solely defined by the critical value of the temperature gradient in the material. Furthermore, the environmental conditions and laser energy may directly affect the amplitude and speed of the temperature cycle. The thermal stress resistance is directly dependent on the speed of the thermoshock. It is interesting to note, however, that a mild heat transfer will generate a damage resistance that is higher than that of a hard thermoshock. Hence, crack propagation initiated by residual stress due to these shock loads is easily influenced by the heat conducted to the cut face. In addition, chemical reactions are also known to contribute to the external stress [29, 31]. Affolter and Schmid give a good overview on processing ceramics with solid state lasers in [44].

For straightforward laser machining, the ideal ceramic substrate would have material properties such as low elasticity parameters, low thermal expansion, a high modulus of

rupture, and a fairly high thermal conductivity. The $Al_2O_3$ substrates used in the research covered in this thesis are unfortunately susceptible to thermal shocks—localized overheating is known to cause large tensile stresses, resulting in subsequent failure [12, 27]. Pabler and Lensch report on a short pulse duration (superpulse) method proven to be effective in reducing the thermal load on ceramic substrates [65]. Dettmer and Charles [20] report on laser trimming alumina as compared to BeO, SiC, and AlN. After the set up the laser for 96% $Al_2O_3$ machining, alumina was the only substrate able to be laser machined with the parameters used (power = 30 Watts, frequency = 300 Hertz, pulse length = 0.3 milliseconds, feed rate = 0.02 inch/second). For BeO the laser power was increased to 50 Watts. Machining AlN and SiC required refocusing of the laser beam, as well as decreasing the feed rate and increasing the power. Although laser machining $Al_2O_3$ is an established practice, simply varying the parameters should allow the other ceramic materials to be machined with relative ease.

The microcracks formed during laser trimming greatly influence the mechanical properties of the ceramic. Most microcracks are formed by stored elastic energy, an immediate result of the thermal stresses generated due to the laser. In order to reduce this elastically stored energy, the heat affected zone must be minimized. Specifically, to examine this procedure of minimizing HAZs and therefore the stored energy, a point heat source must be considered. For instance, applications with a thermal thin sheet having axial symmetry for essentially a line source [44], generally follow an equation of the form:

$$T(r,T) = \frac{Q}{4\pi kdt} e^{-\rho C_p^2/4kt} \tag{2.16}$$

In this equation, Q is the quantity of heat, $\rho$ is the density of the material, $C_p$, the specific heat, k, the thermal conductivity, and t and d are the time and thickness of the sheet respectively. From this approach it can be assumed that if the short laser pulses are considered as immediate heat trains, the width of the HAZ will be reduced, since the immediate pulses will minimize the amount of heat Q liberated [44].

Furthermore, when considering processing brittle materials such as ceramics, the follow-

ing parameters should be varied to minimize the HAZ:

- pulse length
- pulse shape
- spot size
- pulse feed rate (frequency)

The pulse length and/or frequency are to be reduced as prescribed by equation 2.16.

### 2.5.2 Laser Trimming Ceramic Substrates

When substrates are laser trimmed a variety of factors come into play which include cracking, spalling, thermal stress generation, phase transformations, etc. According to Mencik [31], when ceramic parts are laser machined the following structural and material interactions occur:

- low power laser energy incident upon the ceramic workpiece will result in thermal stresses.
- Once the laser beam leaves a point after trimming, the effected region of the substrate will quickly solidify.
- Cracks are generated both parallel and perpendicular to the laser path and in other directions.
- Lasers operating in the pulsed mode tend to eliminate unwanted heating and thermal stress generation.
- Both the speed and motion of the laser beam as well as the radiation intensity influence the integrity and quality of the grooves formed.

Gardner and Beauchamp [46] have discovered that laser trimming was found to reduce the strength of ceramic parts. They also discovered that 96% alumina seemed to degrade far worse than the strength degradation of 99% alumina. Furthermore, the controlled crack growth needed for separating ceramic substrates may be performed optimally through the use of two lasers placed at opposite ends of the substrate. The speed of separation with this technique may be increased four times as much. This process may further be enhanced by translating a cooling device just behind the laser. The result is that tensile stresses are increased at the crack tip as confirmed by Mencik and Machulka [31, 39].

Past research performed by Schulz [25] on both XRRSA and electrical measurements on alumina microelectronic substrates after the substrates were laser trimmed and fabricated with thick film circuits, showed that the residual stresses found were tensile in nature but were found to have no effect on the electrical properties of the thick film circuits. Furthermore, after attempts to anneal the stresses out of the substrates, the stresses were found to be reduced and redistributed. Additional work by Venzant [27] found that the stresses were generally tensile in nature but were isotropically distributed across the substrate.

## 2.6 Summary

It has been shown that the need for the study of residual stress in materials crucial especially in the ceramics industry, since ceramics are replacing many applications usually performed with metals. Residual stresses were shown to be both beneficial and detrimental to engineering parts and XRRSA is the method of choice when nondestructive evaluation of residual stresses are warranted. Laser machining ceramics has been shown to be a very complicated process involving many variables and processing problems. Although complicated, laser machining is known to be far superior to most conventional machining methods (for instance diamond cutting ceramics). Alumina although a well established ceramic engineering material currently does not face the many fabrication and processing problems that newer ceramic materials have this is especially true when laser machining is considered.

Chapter 3 will cover the general problem statement and give a description on what the present work will explore regarding alumina microelectronic substrates.

# Chapter 3

# STATEMENT OF THE PROBLEM

This section will consider the current problem with substrates as found in industry and research laboratories. The discussion will center around past experience with substrate breakage due to residual stresses in the Hybrid Microelectronics Laboratory for microelectronics hybrid circuit research at Virginia Polytechnic Institute and State University and a what the present work will attempt to explore.

Alumina (96%) substrates have been used in the Hybrid Microelectronics Laboratory for RF transmission circuit substrates. The motivation of the research was to identify and eliminate mechanical failures in a wide band probe used for radio frequency transmission applications. The probes were made of an alumina substrate with a thick film (AgPd) transmission circuit fabricated on the top surface. A generic structure of the probe is illustrated in Figure 3.1 including location of fracture.

After laser trimming and fabrication, the probes showed tensile stresses of 17 ksi (117 MPa) on the component side of the probe and compressive residual stresses of the same magnitude on the backside [12]. The tensile stresses are high and play a major part in the fracture process of the probes (as illustrated in Figures 3.1 1(b) and (c)). These stresses are almost half the rupture strength of alumina (50 ksi or 345 MPa).

In the work presented in this thesis the nature of the stress distribution across the substrate is explored as a function of laser trimming, characterization of the substrates before and after laser trimming to ascertain whether any structure property change occurred due to laser trimming, and measure the strain response insitu as a function of laser trimming. Because of the complex structure of standard $Al_2O_3$ substrates and because fo the importance of the interaction of the various phases which may be present, it is essential to understand

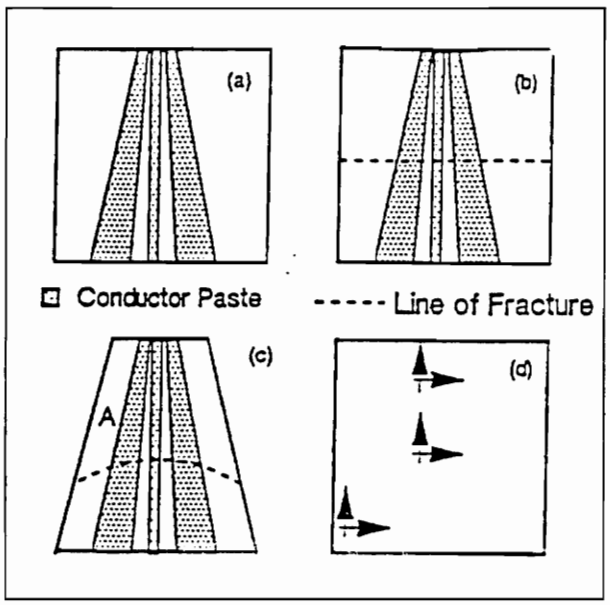


Figure 3.1: Laser cut RF probe. (a) Original substrate with RF probe. (b) Fractured substrate. (c) Fractured laser-cut substrate. (d) Location and orientation of stress measurements [25]

the detailed microstructure of the starting material. Characterization was performed using optical and electron microscopy (scanning electron microscopy (SEM), electron scattering for chemical analysis (ESCA), acoustic microscopy, dye penetrant, x-ray radiography, and electron probe microscopy (EPMA)) The stresses were measured using x-ray diffraction before and after laser trimming and in situ during laser trimming using strain gages. X-ray diffraction was used to measure the residual stresses on a microscopic scale while the strain gages will measure residual stresses on a macroscopic scale. Therefore the stress/strains were measured statically (x-ray diffraction) and dynamically (strain gage). Static measurements by x-ray diffraction residual stress analysis was used to understand the extent of compressive and tensile stresses before and after laser trimming. Tensile stresses are known to cause fracture and subsequent failure. Dynamic measurements were necessary to understand the behavior of the substrates while they were being laser trimmed—this in turn gave crucial information to the final residual stresses. The next chapter will examine

the materials characterization procedures of $Al_2O_3$ microelectronic substrates used in the present work.

# Chapter 4

# ALUMINA SUBSTRATE MATERIALS CHARACTERIZATION

This section will explore the procedures used to characterize the alumina substrates. Optical microscopy, secondary electron microscopy/energy dispersive x-ray analysis (SEM/EDAX), electron spectroscopy for chemical analysis (ESCA), and electron probe microanalysis (EPMA) were used to understand the chemical nature and composition of the substrates. X-ray phase analysis was used to verify the phase results as detected by EPMA. NDE techniques such as liquid dye penetrant and acoustic microscopy were also used and will be discussed briefly. Some typical results of EPMA and X-ray phase analysis are given in this Chapter while the results of the other techniques will be shown in Chapter 5. The ceramic substrates were characterized for chemical composition, microstructure (volume fraction of the glass, pore and other significant phases, and fractography), and phases present. X-ray residual stress analysis was employed as the major characterization step used to determine the stress distribution in the substrates. Listed below are merits of each technique and the information they provide.

- optical microscopy was used to perform basic fractography work on a macroscopic level as well as identify phase segregation.
- SEM/EDAX was used to investigate both macroscopically and microscopically the structure and composition of the substrates. EDAX was found to be sensitive only to the alumina content of the substrate, so that use of ESCA became necessary. SEM photos were very useful since we were able to probe the walls and depths of laser trimmed paths to look for flaws and to compare the laser–material interactions of the

400 watt JK700 and the 30 watt ESI lasers.

- X-ray radiography was employed to discern any macroscopic anomalies in the substrates after being machined (laser and diamond cut).
- acoustic microscopy was utilized for the same reasons as radiography but to discern any variations at a smaller scale as a function of laser machining only.
- a dye penetrant technique was used to detect any fractures on a macroscopic level after substrates were laser machined.
- ESCA was used to ascertain the exact chemical composition of the substrates.
- EPMA was employed to perform compositional maps of the substrates to discern the number and types of phases present and to qualitatively calculate the volume fraction of the phases detected.
- X-ray phase analysis was performed with the Scintag XDS 2000 to verify quantitatively unsuspected phases observed by EPMA.
- X-ray residual stress analysis is a technique that allows exact residual stress measurements in material systems possible and was used in this research to map the stress distribution in the substrates before and after laser machining.

## 4.1 Materials

The alumina substrates used in this study were obtained from Kyocera Industrial Ceramics Corp., San Diego, CA. The substrates were 96% alumina with a 4% glassy phase (this phase is necessary for standard thick film substrates to enhance bonding between the alumina and thick film paste). Their properties are similar to those given in Table 2.1; they are standard thick film substrates cut in 1 x 1 x 0.025 in. (25.4 x 25.4 x 0.64 mm) squares.

## 4.2 Materials Characterization

The following sections will expand upon each of the characterization techniques by giving more specific details and how each technique was utilized to characterize the alumina thick film substrates. Results of the as-received materials are presented here; those for laser-cut materials will be presented in the following chapter.

### 4.2.1 Optical Microscopy

A variety of optical tools were used to observe the surface and bulk integrity of the substrates. A Bausch and Lomb General Inspection Microscope was used to inspect the substrates before and after laser scribing and to observe the effect of liquid dye penetrant on the substrates. Magnification ranges varied between 10X to 25X. A polarizing automated high power microscope was used to inspect laser trimmed substrates immediately after laser trimming with the JK700 laser at ITT GTC in Roanoke, Virginia. Typical magnifications ranged from 25X to 500X. Color micrographs were automatically created once resolution and magnifications were achieved. A Neophot Optical Metallograph Microscope was used to optically characterize metallogrphically prepared substrates. For this setup, a substrate was laser trimmed with five power levels using the JK700 laser in five parallel locations . The sample was next metallographically prepared for optical and EPMA analysis. Sample preparation involved sandwiching the substrate between two additional substrates two maximize the surface area to be analyzed. The assembly was mounted at 45° to achieve additional surface area. The assembly was next selectively diamond polished with $0.5\mu$, $0.3\mu$, and $0.1\mu$ diamond paste with metallographic oil as the medium for polishing between a nylon polishing pad and the mounted susbstrates.

### 4.2.2 X-ray Radiography

X-ray radiography is a convenient technique for detection of significant macroscopic variations of any material. More importantly, this technique has the ability to detect

crack—like defects since they are sensitive to orientation with respect to the radiation. The technique was applied to the substrates that were laser trimmed to look for cracks developing radially from the separation region or trim region and as a function of diamond cutting. The X-ray machine utilized was a Hewlett Packard Faxitron X-ray System model 43805N. The work was performed at ITT Electro-Optical Products Division, in Roanoke Virginia.

### 4.2.3 Accoustic Microscopy

Scanning acoustic microscopy was employed to characterize the substrates for any suttle defects in or near the heat affected zone (HAZ) due to the laser trimming process. The instrument was a Model UH3 Olympus Scanning Acoustic Microscope (SAM). Several laser trimmed substrates were analyzed with this microscope. The surface of the substrates were scanned with a focusing probe optic at a frequency of 200 MHz. The probe had a 0.25 in. focal length and a 30° aperture. The focusing probe or lens was coupled to the backside of the substrates through a water medium (used to create a passage for sound waves thereby enhancing the attenuation and improving the overall signal-to-noise ratio). Image processing was next performed using a Kodak SV6500 Olympus Q2 Image Analysis System. This technique however, is restricted to the surface or at a few wavelengths below it. As received substrates showed no discernable cracks at the level of resolution of the SAM ($5\,\mu$m at the 200 MHz frequency).

### 4.2.4 Dye Penetrant Visual Inspection

Dye penetrant can usually detect the most severe surface flaws. However, the technique is not optimized for ceramics since a "capillary" effect occurs due to the porosity of the ceramics. However, the technique was utilized since it is capable of penetrating surface-or near-bulk cracks as small as $1\mu$m width in about 15 seconds. The penetrant used was a tube from Glo-Tek, Dallas Texas. A substrate that was laser trimmed was examined using the dye penetrant at the HAZ (heat affected zone) while placed under an inspection microscope

and examined; magnification varied between 10 and 25X. The penetrant fluoresces, while penetrating any cracks when viewed under UV light, none were detected. In principle dye penetrants can only quantify surface cracks lengthwise but not the depth [4].

### 4.2.5 SEM/EDAX

To analyze the surface of the substrates for pore size and laser machining effects on a microscopic level, scanning electron microscopy was performed. A Scanning Tunneling Electron Microscope (STEM) located in the Virginia Tech Microstructure Laboratory was utilized for analyzing the microstructure of the substrates before and after laser trimming. Results are illustrated of a substrate laser machined with an ESI laser in Chapter 5. EDAX was employed to perform chemical analysis of the substrates; the technique, however, was only sensitive to the aluminum in the substrates. ESCA and EPMA were therefore used to detect the other species in which the EDAX was insensitive to, like silica and MgO.

### 4.2.6 Elemental Mapping of Alumina by ESCA

A Kratos XSAM-800 X-Ray Photoelectron Spectrometer located in the Virginia Tech Microstructure Laboratory was used for ESCA analysis. The samples were chemically cleaned with trichloroethylene and acetone before being analyzed. The results of ESCA are shown in Figure 4.1 and a summary of data obtained from this spectrum is given in Table 4.1. The initial chemical analysis was performed at the immediate surface, i.e., no sputtering was done (zero sputter time). To analyze the alumina surface a few atoms below the first monolayer, sputtering with ions must be performed. From Figure 4.1 and Table 4.1, the carbon peak is high due to handling. After sputtering for 5 minutes, the carbon content drops and the percent atomic species detected is at 100% instead of only 90% as in the case for zero sputtering time.

Table 4.1: Summary of ESCA results, atomic % species detected.

| | C | O | Al | Si | Ca | Mg |
|---|---|---|---|---|---|---|
| Quantum states | 1*s* | 1*s* | 2*p* | 2*p* | 2*p* | 2*p* |
| Sputter = 0, | 48 | 27 | 18 | 4.4 | 1.2 | 1.4 |
| Sputter = 5 min. | 22 | 40 | 32 | 4.1 | 1.1 | 0.6 |

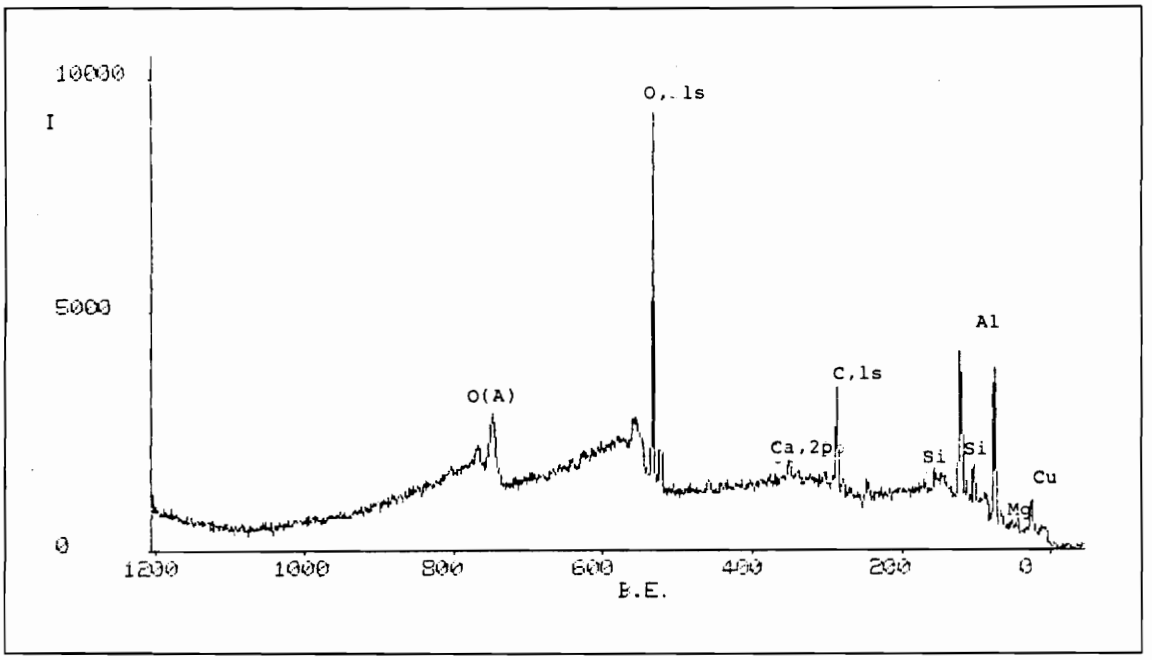


Figure 4.1: ESCA analysis of 96% alumina illustrating elements detected. The copper peak is due to the specimen chamber.

### 4.2.7 Elemental Mapping of Alumina by EPMA

Electron probe micro-analysis (EPMA) allows one to perform elemental maps of the constituent phase areas of interest. EPMA is founded on the principles of the interaction of highly energized electrons with the specimen serving as the target. The instrument utilized for the compostional work presented here was a CAMECA-SX50 Electron Microprobe located in the Geological Sciences Department at Virginia Tech. It uses a 4-spectrometer or four x-ray crystal detectors to perform wavelength dispersion as opposed to energy dispersion found in SEM/EDAX machines.

The process for performing electron microbe analysis essentially involved focusing a 15 kV @ 10 nA electron beam to a 1$\mu$m spot size and slowly scanning the substrate in 3$\mu$m steps from the base of the substrates cross section to the surface. X-ray spectrometry was used to detect the four phases by comparing a standard to an unknown. Corrections were made for fluorescence, absorption, and the affected atomic number.

For quantitative information using EPMA a fully automated analysis was performed at every beam location. The system must perform a pixel map count rate for each element using a wavelength spectrometer and an energy spectrometer. From the ratio of these two measurements values, an intensity ratio is performed between a known and unknown standard. After a matrix correction and digital image processing, a compositional map is made of the area of the sample being analyzed. Figure 4.2 illustrates an x-ray map of the alumina substrates used in this research. The four quadrants illustrate the different phases detected. The technique used to produce the micrographs in Figures 4.2—4.5 is called thresholding in which the phase of interest is enhanced while suppressing the unwanted phases.

Figure 4.2 illustrates a x-ray map of one region of a substrate that was metallographically prepared as discussed in the optical microscopy section above. In order to perform a semiquantitative analysis of the volume fraction of each phase, x-ray maps were taken of four phases determined from the electron probe. The four phases included the glass

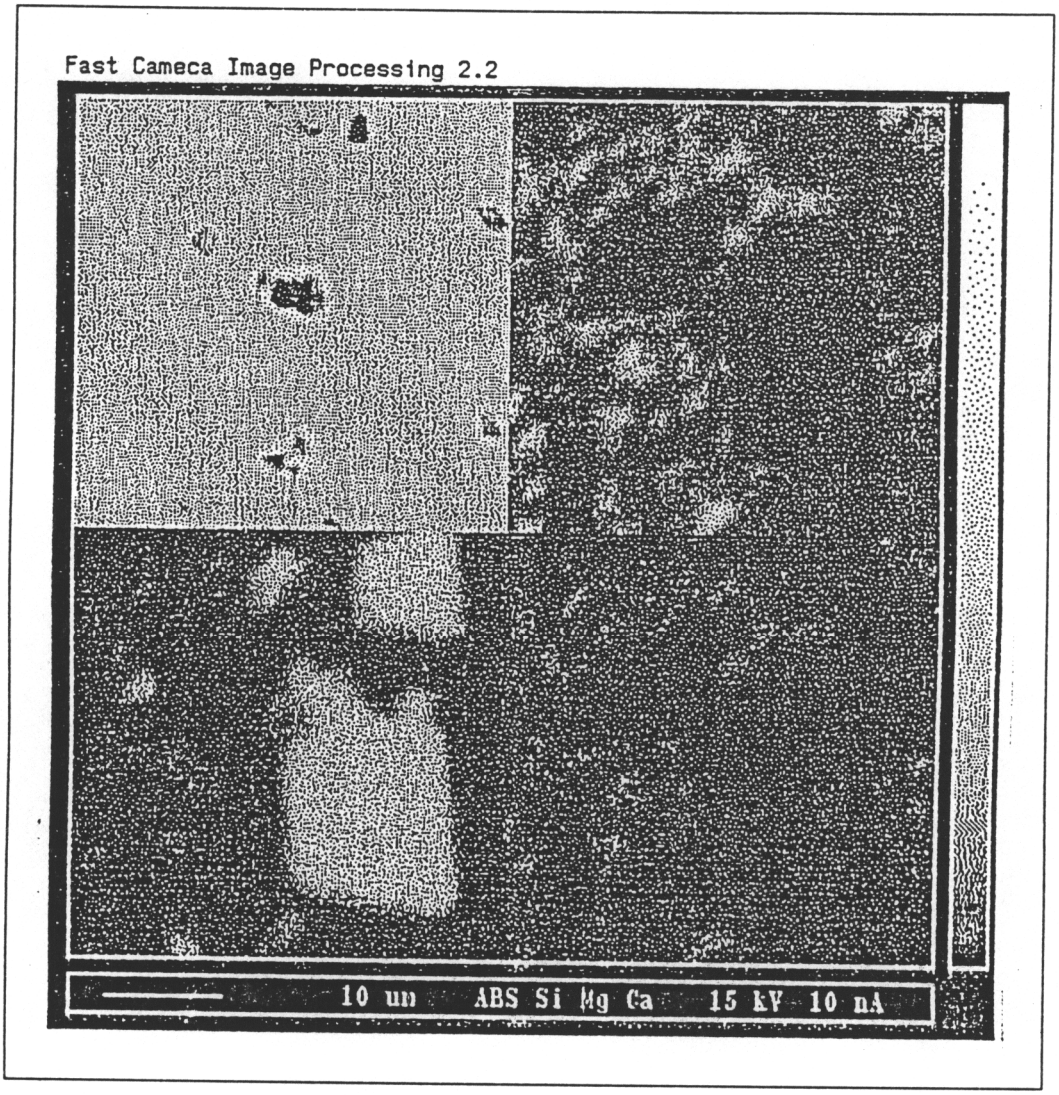


Figure 4.2: X-ray Map of alumina showing elemental compositions. The top left illustrates the pore phase, the top right the glassy phase, bottom left the Al-Mg spinel, and the bottom right Ca, which is part of the glass. Each quadrant was determined by suppressing through thresholding all phases allowing an outline of the pore phase.

(involving calcium and silica), pores, and the magnesium-aluminum spinel structures. Five micrographs were made of each phase using a 200 mm camera so that an areal analysis could be performed for the point counting procedure explained in the next section.

Other trace elements were found using EPMA such as Na (0.7%), K (0.4%) and Fe (0.3%). The iron is probably serving as a contaminant species.

The next section will cover how the volume fraction of each phase (viz., pores, glass, and $MgAl_2O_4$) was determined from point counting and areal analysis techniques.

### 4.2.8 Phase Analysis by Point Counting

Point counting is a conventional technique used to determine the various constituents in a microstructure and can be done on micrographs obtained from optical microscopy, SEM, TEM, EPMA, etc. From the micrographs created from the EPMA x-ray maps, a regular grid was superimposed on each micrograph and the number of intersections of the constituent which lie on the grid lines was determined.

In general when the variable constituent is measured as a proportion $p$, the mean $\mu$ and standard deviation $\sigma$ of the distribution are known to be related by [47]:

$$\mu = p\sigma = \sqrt{[p(1-p)/n]} \tag{4.1}$$

The volume fraction is therefore the ratio of the average number of intersections (Y) in the area of the constituent to the total number of points counted (n) and p is the proportion Y/n. A total of five (represented by k in Table 4.2) frames were taken of each phase which resulted in a total of 500 points per phase, since each grid contained 100 intersection points. The 500 points utilized per phase are in agreement with the confidence interval values determined in the next section for the glassy phase only. When point counting is employed the results are known to conform to the binomial distribution. From this, the accuracy of the estimate can be calculated from the points counted and the subsequent determined proportion.

Table 4.2: Summary of point counting results

| Phase | n | k groups | Y | p=(Y/n)(proportion) | Volume Fraction |
|---|---|---|---|---|---|
| glass | 500 | 5 | 37 | 37/500 | $0.074 \pm 0.031$ |
| Al-Mg spinel | 500 | 5 | 15 | 15/500 | $0.034 \pm 0.021$ |
| Pores | 500 | 5 | 24 | 24/500 | $0.048 \pm 0.114$ |

From point counting, the volume fractions of the three phases were determined as shown in Table 4.2.

From the results, confidence intervals may be calculated using the binomial distribution. For instance if Y is the number of successes that a line intersection occurs for a certain constituent and n is the total number of points counted, then Y/n is the sample proportion p then the equations given above, viz., the mean and variance will follow the binomial distribution. The central limit theorem implies

$$\sigma = \frac{Y - np}{\sqrt{np(1-p)}} \tag{4.2}$$

which follows a binomial distribution since it is approximately N(0,1) and hence

$$p\left[-z\left(\frac{\alpha}{2}\right) \leq \frac{Y - np}{\sqrt{np(1-p)}} \leq z\left(\frac{\alpha}{2}\right)\right] = 1 - \alpha \tag{4.3}$$

where z is a test statistic used to calculate the critical region for the confidence interval. In general Y is usually observed to be y and if p is approximated by y/n then a 100(1-$\alpha$) percent confidence interval will be

$$p = \frac{y}{n} \pm z\left(\frac{\alpha}{2}\right)\sqrt{\frac{(y/n)(1-y/n)}{n}} \tag{4.4}$$

Therefore, for a 90% confidence interval using the above expression, the the following is obtained [0.0771, 0.0431] which corresponds to a 1% standard deviation for 500 points using Table VIII of [47] for the glassy phase. Similar calculations for the spinel phase and pores result in the estimated confidences limits (90%) shown in Table 4.2.

Table 4.2 shows that the glass phase, which was found to be composed of silicates, CaO

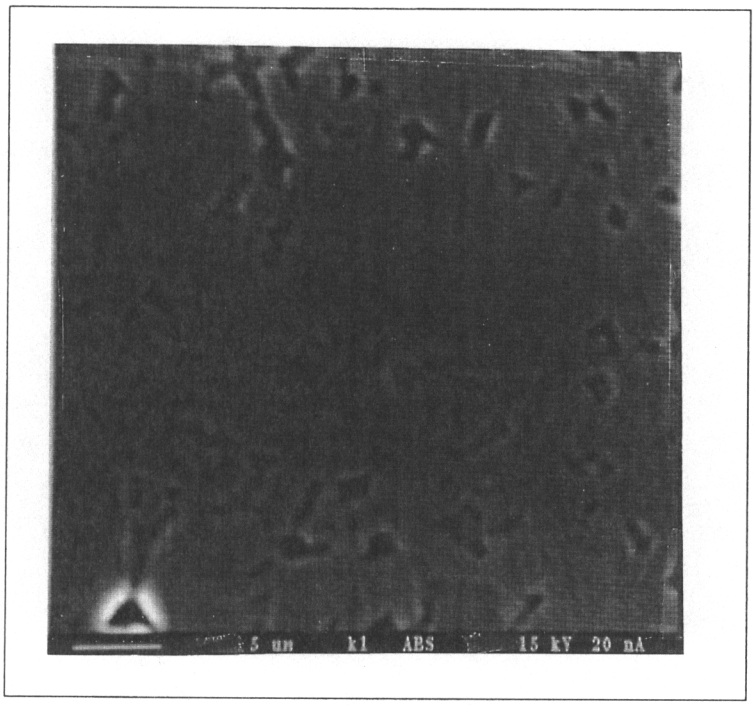


Figure 4.3: Threshold x-ray map of the glass phase from an alumina substrate. Note the fairly uniform distribution of this phase representing a volume fraction of 7.4% from this substrate.

and Mg, has a volume fraction of 7.4%. This volume fraction is randomly distributed as illustrated in the micrograph shown in Figure 4.3. Similar micrographs are given in Figures 4.4 for the spinel phase and 4.5 for the pores. The pore phase effects will be discussed in Chapter 6. In Figure 4.3 the glassy phase is randomly distributed and this randomness may have a significant effect on the overall residual stress of the substrates. The pore phase distribution, as shown in Figure 4.5 also illustrates this same randomness and may also contribute some effect on the measured residual stress.

### 4.2.9 X-ray Diffraction Phase Analysis

Since traces of $MgAl_2O_4$ spinel were observed using EPMA, X-ray diffraction phase analysis was performed to verify this spinel phase using a Scintag XDS 2000. A diffraction pattern of this phase was performed using a step-scan procedure since the spinel phase

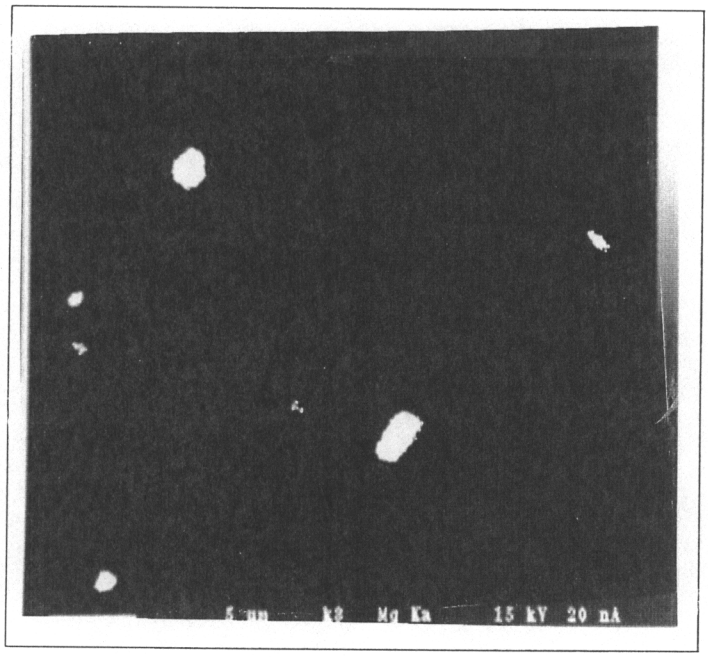


Figure 4.4: Threshold x-ray map of the Mg-Al spinel phase from an alumina substrate. Its volume fraction was determined to be 3.4% in this substrate.

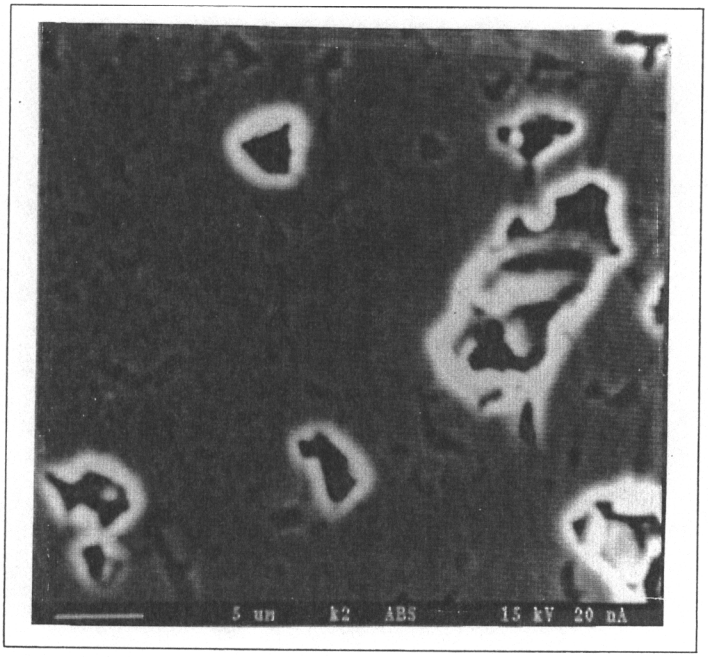


Figure 4.5: Threshold x-ray map of the pore phase from an alumina substrate. This phase was found to be quite abundant representing a volume fraction of 4.8% from this substrate.

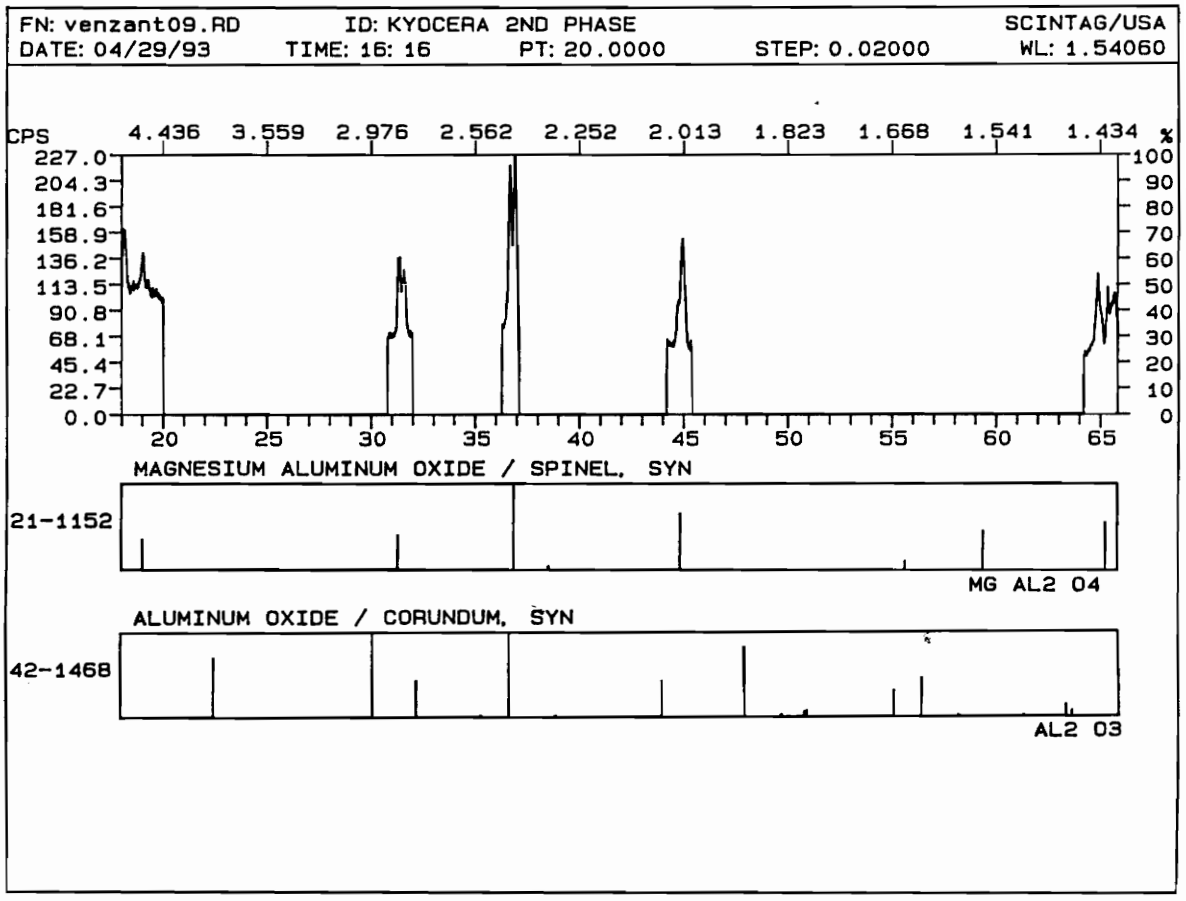


Figure 4.6: X-ray diffraction pattern of 96% alumina showing a match with corundum and the weak peaks which are identified as the spinel phase as shown at the bottom of the figure.

peaks are weak compared to those of the major phases in alumina. The pattern is shown in Figure 4.6. From the results, the corundum and $MgAl_2O_4$ spinel phases were identified with respect to to the diffraction pattern for the 96% alumina substrates as shown in this figure. The 3.4% volume fraction of the spinel is created from a phase transformation resulting from the aluminum and magnesium phases of the substrate combining during processing.

## 4.3 X-ray Residual Stress Analysis

X-ray residual stress analysis was the major technique used to characterize the state of residual stress of the alumina substrates. For the experimental x-ray residual stress work, a Technology For Energy Corporation (TEC) Model 1610 portable X-Ray stress analyzer was used. The measurements were made with nickel filtered Cu$K_\alpha$ radiation, which was diffracted from the (146) planes of the alumina substrates at approximately 136° $2\theta$. From work performed previously [50, 51], the (146) planes generate high peak intensities at large $2\theta$ angles, thereby giving more significant shifts in $2\theta$. For the experiments performed for the present work, the copper X-ray tube was operated at 37 kV at 0.85 mA. The (146) planes were measured using a position-sensitive proportional counter (PSPC) detector mounted on a 135° Bragg-angle bracket. A schematic of this arrangement and the overall stress analyzer system is illustrated in Figure 4.7. A picture of the TEC diffractometer is shown in Figure 4.8.

The PSPC is essentially a one-dimensional wire chamber counter that is designed to immediately observe by detection a broad range of angles in the $2\theta$ range. Furthermore, each photon that diffracts and scatters unto the detector's wire is then electronically decoded in order to illustrate a digital image of the scattered X-rays (again, in one dimension). The computer algorithm BIAXAL, part of the software of the stress analyzer, determines the peak location from the image generated by statistical curve fitting. [1]

Channel location is then determined from the detector of the top percentage of the fit peak. It is this channel number that is related to the exact $2\theta$ angle. A $d_{hkl}$-spacing versus $\sin^2\psi$ is calculated from the $2\theta$ value by utilizing Bragg's law. This curve-fitting process is performed after geometric corrections for detector background, Lorentz polarization, and sample absorption, all of which affect the scattering process and vary with $\theta$. Counting

[1] The BIAXAL program fits a parabola to a certain percentage of the peak. A 20% peak fit was used, which, as can be seen in Figure 4.5, is above the $K_{\alpha 2}$ maximum intensity and therefore only fits to $K_{\alpha 1}$. The $K_{\alpha 2}$ peak was not included in the calculation since it would have fit the peak in the wrong region of the spectra.

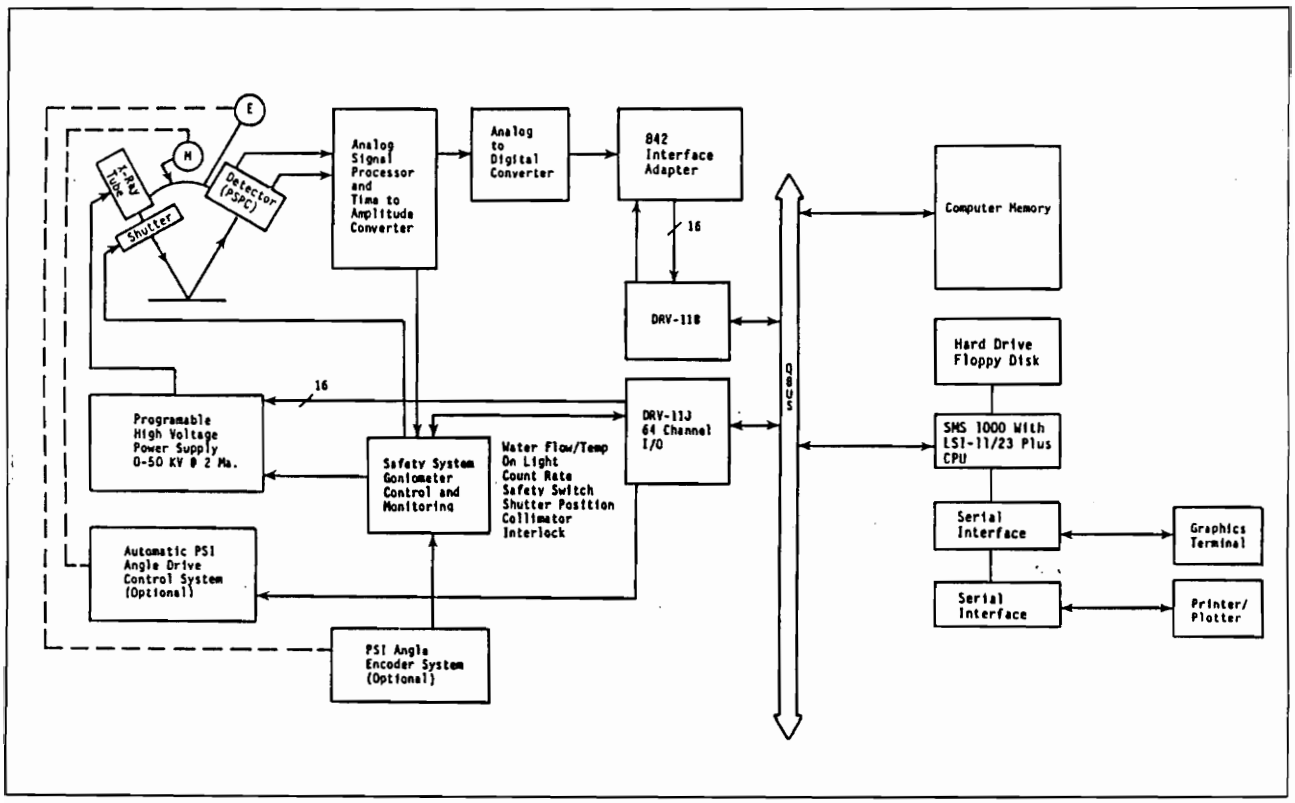


Figure 4.7: Schematic of the detector and diffractometer with associated hardware of the TEC stress analyzer [52].

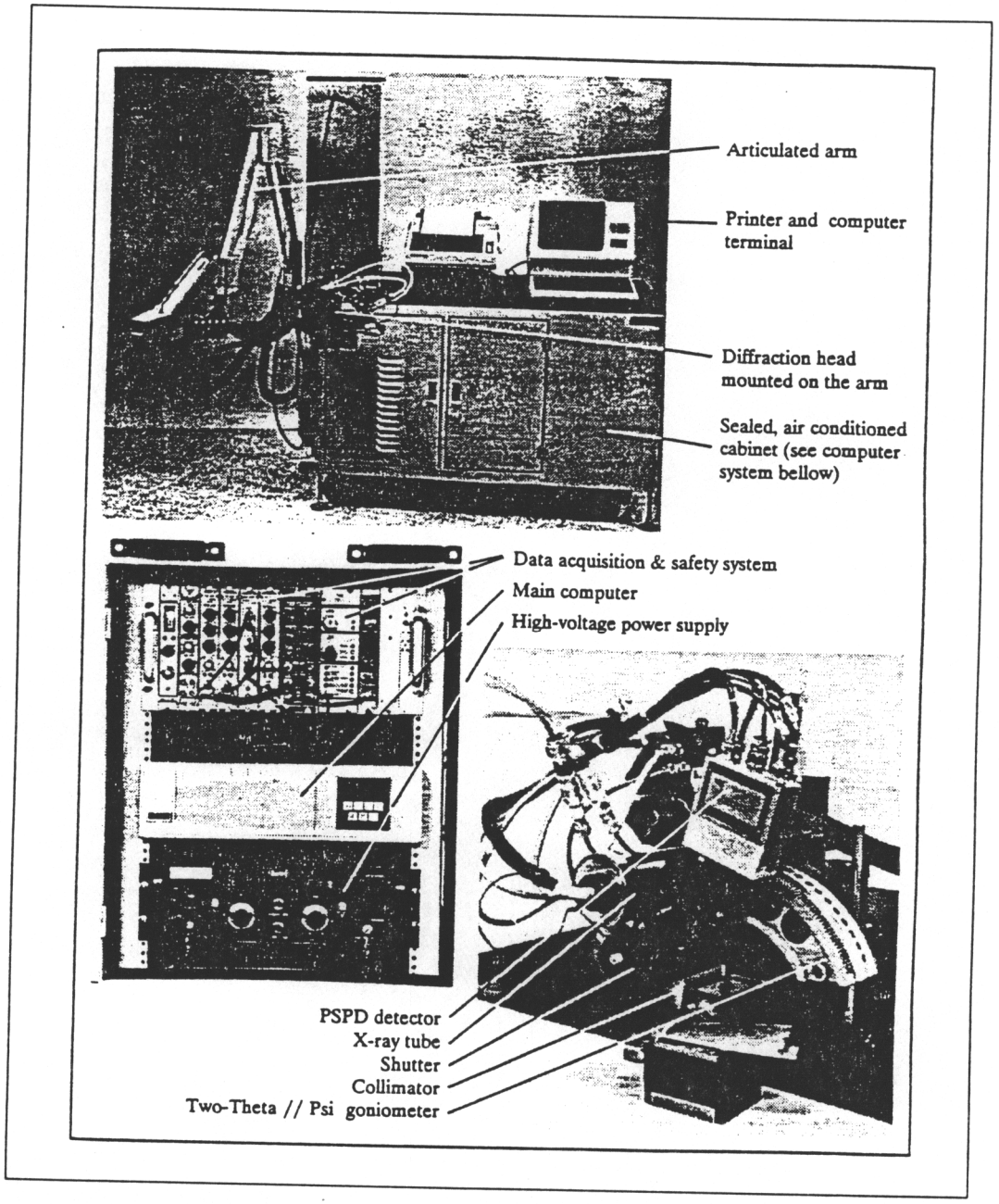


Figure 4.8: TEC Portable Apparatus for Residual Stress (PARS) measurements. [52].

statistics errors in the measurement, which are affected by the amount of data acquisition performed, are also determined in the algorithm. From the error computed, one can make a judgment call about the experiment. An overview of the PSPC and its basic operation can be found in [26, 48].

A typical diffraction pattern is shown in Figure 4.9. This Figure shows a series of peaks which are known to be the result of several things. The (146) planes are easily singled out as are the (3 0 14) located at channel 73 and (2 0 14) at around channel 104.5. The peaks at the end are due to the end effects of the detector, while the (146) peaks between the end effect peaks are the result of peaks contributed to lower $2\theta$ scans [12]. Furthermore, the (146) peaks represent a doublet ($K_{\alpha 1}$ and $K_{\alpha 2}$). The peaks are sharp because $Al_2O_3$ is so brittle; there is not enough microstrain to sufficiently broaden the peaks. The (146) peaks in most cases are nearly overlapping and may be treated as one peak. Therefore to perform calculations on this peak the program that performs the parabolic fit must be programmed to ignore the correction for $K_{\alpha 2}$. Furthermore, the additional peaks seen in the pattern are removed so that the software in the stress analyzer will not analyze them since if analyzed, will result in erroneous data by placing the peak position off its true location during the parabolic fit routine of the software. Figure 4.10 illustrates a modified diffraction pattern showing only the peaks of interest.

It is crucial to discuss at this point the importance of the X-ray elastic constants for the material under study. This material constant should be determined experimentally since it will vary per sample orientation and corresponding atomic planes. However, in this research, interests laid strictly in the absolute value changes; therefore, the results of Tanaka, Yamamoto, and Suzuki [49] (given in Table 4.3) were utilized since they calculated the elastic constant for 96% alumina substrates.

Before starting the experimental study of residual stress measurements across the samples, several collimators (rectangular and round) were used to ascertain which gave the best statistics and stress value when measured as compared to stress values of a reference sample (alumina substrate). From these trials a 2 mm round collimator met the statistical

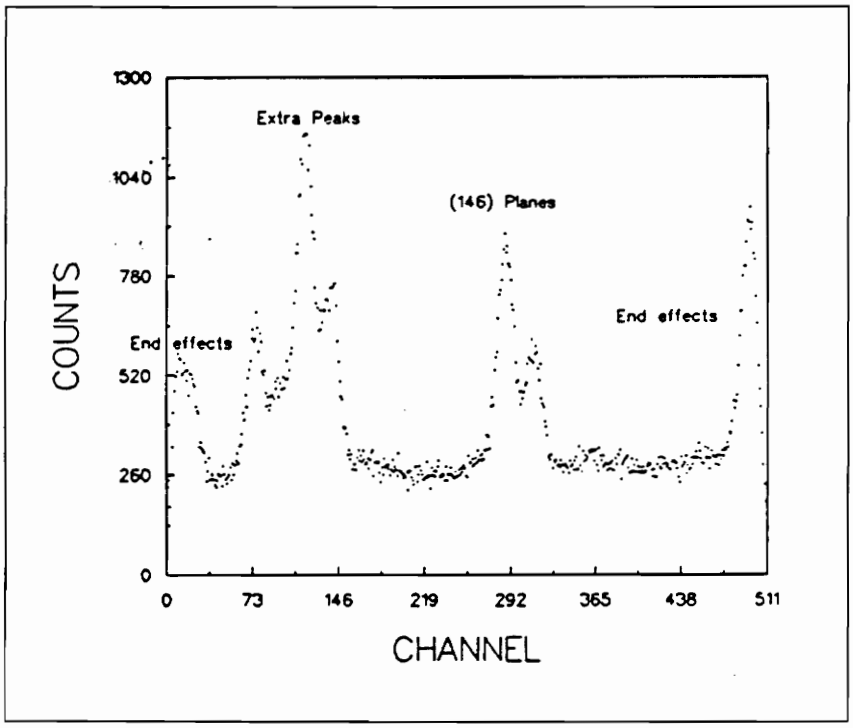


Figure 4.9: Typical diffraction pattern of 96% alumina before peak subtractions. The (146) planes are seen at channel 292, the peaks seen at channel 73 are identified as the (3 0 14) plane and the peak at 104.5 is identified as the (2 0 14) plane, as determined by X-ray phase analysis; see text for details.

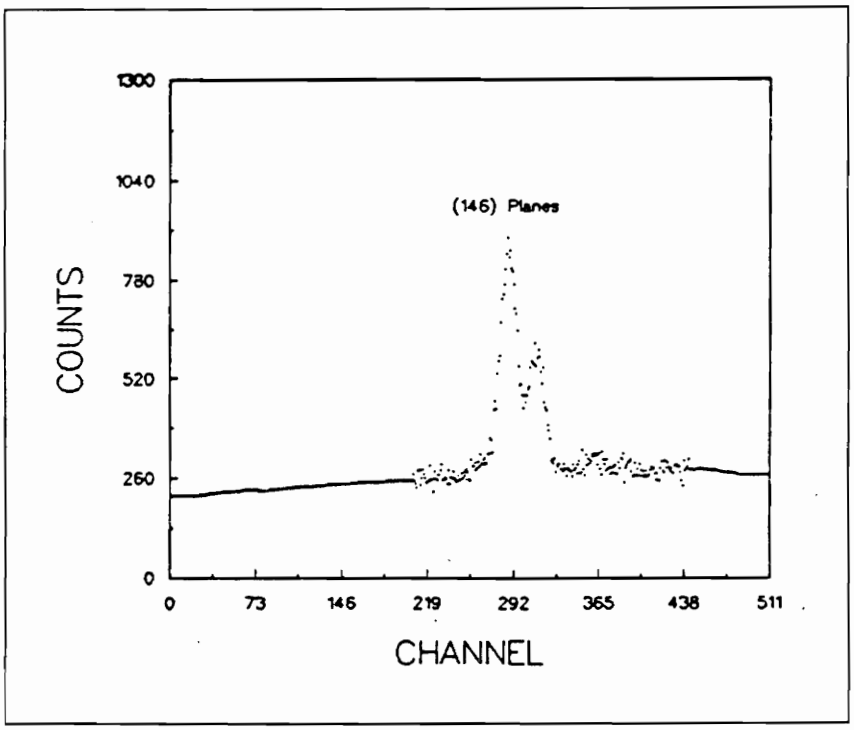


Figure 4.10: Typical diffraction pattern of 96% alumina after peak subtractions. This diffraction pattern illustrates the (146) planes.

Table 4.3: X-ray constants determined for 96% Alumina [49].

| Alumina (% Purity) | Elastic Constant $E/(1+\nu)$ (ksi) | (GPa) |
|---|---|---|
| 99 | 47.0 | 324 |
| 96 | 45.2 | 312 |
| 92 | 34.8 | 240 |

accuracy and stress values that closely matched the stress statistics of the reference sample. The measurements were made at seven different $\psi$ tilts: $\pm 33$, $\pm 25$, $\pm 15$, and 0 degrees $\psi$ (after careful sample and diffractometer alignment). To average across the grains for statistical accuracy, and to reduce the effects of preferred orientation, each $\psi$ was programmed to oscillate three degrees i.e., the angles oscillated at $\pm$ 1.5 degrees in each direction. Initially measurements were taken at 120 seconds, which led to large error bars due to insufficient peak intensity. Count times were then doubled, resulting in better statistics.

The procedure used here was repeated for each $\psi$ angle and performed three times for each measurement location to reduce systematic errors resulting from sample positioning or alignment. In general, a plot of the $d_{hkl}$ versus $\sin^2\psi$ is linear (where the stress is proportional to the slope); however, deviations of the plot caused by nonuniformity of stress with depth, shear stresses, and sample preferred orientation will result in nonlinearity. Figure 4.11 illustrates a $d_{hkl}$ versus $\sin^2\psi$ plots generated from the TEC BIAXAL program.

### 4.3.1 Statistical Error Analysis

The output is shown in Table 4.12. This table shows the measurement setup and data generated from the analysis of raw data. At the bottom of the table are the stress value, counting statistics, and goodness of fit stress error. The counting statistics (CS) at the bottom of the table are errors corresponding to differences in peak intensities diffracted from different grains, leading to uncertainty in peak location. This Bragg peak location error will generate an error in the d-spacing, and will therefore give a error in the slope and subsequently in the stress value since it is proportional to the slope. Thus, CS error

is simply the errors expected if only those errors associated due to finite measuring times of the experiment were involved. Goodness of fit (GF) errors are nothing more than the deviations of the slope of the $d_{hkl}$ versus $\sin^2\psi$ plot.

To test for the completeness of the Biaxial analysis used by the software program BIAXAL, a shear stress or triaxial analysis was performed on the calculated peak data from the alumina substrates measurements and is explained below.

### 4.3.2 Shear Stress Analysis

The procedure for performing the shear stress analysis is performed by retrieving data from the Biaxal data analysis program provided by TEC and downloading these data to a database program called RS/Base developed in our facilities [40]. Before the data are downloaded they are analyzed on the TEC stress analyzer program and a report is created. This report is then downloaded to RS/Base which is resident in a DELL 286. A typical analysis RS/base report is shown in Figure 4.13. The first part shows the general experimental setup conditions, the second illustrates the data acquisition and some statistics. The final portion illustrates the model fit to the data, in this instance the Biaxial model is used. In Figure 4.14, the triaxial model or shear stress model is compared to the biaxial model. Figure 4.15 illustrates a plot of the data.

The shear stress analysis or pseudo-triaxial stress analysis program RS/Analyze was next applied [41] to generate a model from multiple regression of the data which considers both the biaxial and triaxial models. Both the biaxial and triaxial models are discussed in the next section.

From the data in Figure 4.14, the statistical analysis lists an $R^2$ value which represents how the model fits the data, an F-test which estimates the agreement of the data with the model, and a p-value which measures the level of significance of a statistical test. In general the closer to one the $R^2$ value is the better the model. For the biaxial model for the data in Figure 4.14, the $R^2$ test is a low 0.07 which would indicate that this model is not a good fit to the data. The F-test number should be as high as possible in this case it is only .39.

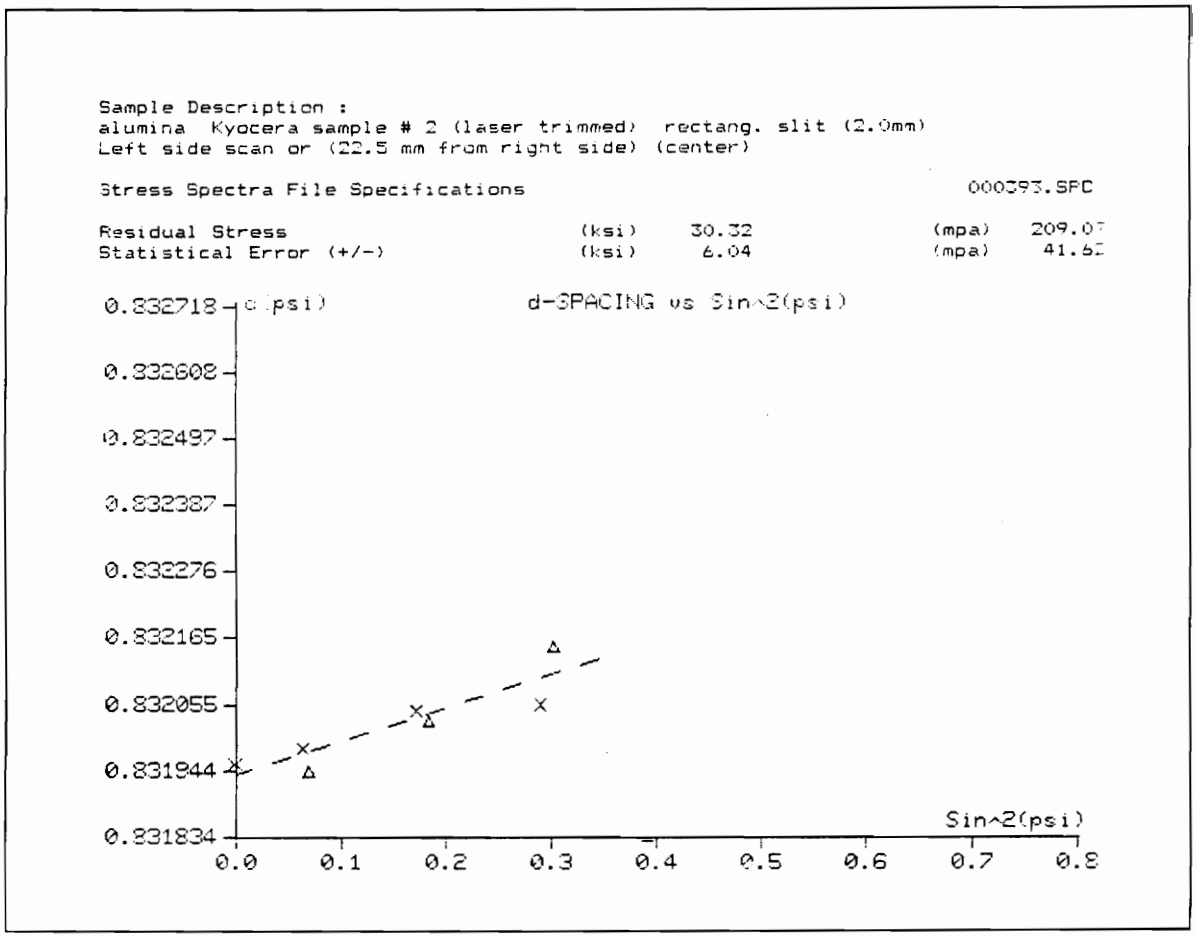


Figure 4.11: Typical $d_{hkl}$ versus $\sin^2\psi$ plot of alumina generated from the biaxial stress analysis. Statistically this data fits the Biaxial stress model, however there are cases in which this model is not accurate as in the shear stress in which the data shows splitting in the plot.

```
*****************        Residual Stress Analysis Report        *****************

Date: 12-JUN-91   Time: 06:28:41

Sample Description :
alumina  Kyocera sample # 2 (laser trimmed)  rectang. slit (2.0mm)
Left side scan or (22.5 mm from right side) (center)

System Hardware Configuration :
        Auto Psi Angle Drive
        Psi Angle Position Encoder

ADC Channels Full Scale                                                    512
Collimator Slit Type -                                  Rectangular      2.00

X-ray Target Material and Wavelength                     Copper     1.54178
Detector Mounting Block Bragg Angle                                   135.00
Oscillating Psi Angle                                                   3.00
High Voltage and Beam Current                          37000.          0.85
Peak Bounding Range (percent)                                           40.

Material ID Number                                                      19
Material Type                                  Alumina 96%, (146) Kyo

Stress Spectra File Specifications      (altered spectra)          000393.SPC
Stress Spectra Acquisition Date:                          12-JUN-91   05:41:24
Stress Spectra Count Time (sec)                                        120

Calibration File Specifications                                    CCR51L.135

Detector Calibration Coefficients
A  0.785973E-08        B -0.458547E-05        C  0.0302049        D  127.3762


 Psi   Sin^2(Psi) Pk Chan  Intens   FWHM   Kalp Cor  2-Theta D Spacing  St. Dev.
----- ---------- ------- -------- ------ -------- ------- --------- --------
-33.0  0.30267   285.68    116.6   0.65   0.05943  135.75  0.832153  0.000012
-25.0  0.18397   286.30    107.9   0.58   0.03533  135.80  0.832028  0.000011
-15.0  0.07063   286.91     85.4   0.56   0.02506  135.83  0.831944  0.000013
  0.0  0.00005   287.44     88.4   0.61   0.04426  135.82  0.831955  0.000014
 15.0  0.06348   288.01     91.7   0.68   0.06987  135.81  0.831981  0.000016
 25.0  0.17334   288.37    101.3   1.09   0.10184  135.79  0.832044  0.000015
 33.0  0.29037   288.28    118.5   1.15   0.10309  135.79  0.832056  0.000016


Fitted Delta D vs Sin^2(Psi) Data
D Spacing Intercept                                                 0.831936
Slope of Fitted Line                                          5.579050E-04
Material Stress Constant                                      2.211538E-08

Residual Stress                                    30.3 ksi        209.1 MPa
Counting Statistics Stress Error  (+/-)             2.7 ksi         18.7 MPa
Goodness of Fit Stress Error      (+/-)             5.4 ksi         37.2 MPa
Total Stress Error                (+/-)             6.0 ksi         41.6 MPa
```

Figure 4.12: Typical data summary and analysis report.

**Stress Spectra:**

| | | | | | |
|---|---|---|---|---|---|
| **Filename** | 000407.SPC | | **Acquisition Date/Time** | 20-Feb-92 | 19:14:59 |
| **User Def 1** | VENZANT | **User Def 2** | | **User Def 3** | |

**Sample Description :**

alumina Kyocera reference sample, round collimator (2.0mm). Laser trimmed sample #2, scan is in x axis 4mm f center.

| | | | | | |
|---|---|---|---|---|---|
| **Measurement** | **Type** | Psi | **Stress Spectra Count Time (Sec)** | 120.00 | |
| | **Chi Value** | 0.0 | **Tilt Angle Oscillation Range** | 3.0 | |
| | **Phi value** | 0.0 | | | |
| | **Psi Value** | 0.0 | **Slit Resolution in Two_Theta** | 0 | |
| | | | **Collimator Shape/Size** | Round | 2 |
| | **X-Ray Tube** | Copper | | | |
| | **Wavelength** | 1.54180 | **Peak Bounding Range (%)** | 20 | |

**Material:**

| | | | | | |
|---|---|---|---|---|---|
| **Name** | Alumina 96%, (146) Kyo | **ID #** | 19 | **Database** | T |
| **(1+Mu)/E** | 2.210000E-08 | **Anisotropy Factor** | 0.00 | | |

| Detec | Var | Sin^2(Var) | Intensity | FWHM | 2-Theta | d-spacing | St. Dev |
|---|---|---|---|---|---|---|---|
| 0 | -33.0 | 0.30370 | 33.4 | 0.71 | 135.8800 | 0.831774 | 0.000043 |
| 0 | -25.0 | 0.18466 | 25.6 | 0.64 | 135.9000 | 0.831724 | 0.000029 |
| 0 | -15.0 | 0.07094 | 23.0 | 1.12 | 135.8900 | 0.831746 | 0.000106 |
| 0 | 0.0 | 0.00006 | 21.9 | 1.12 | 135.9000 | 0.831730 | 0.000040 |
| 0 | 15.0 | 0.06307 | 22.5 | 1.07 | 135.9100 | 0.831692 | 0.000046 |
| 0 | 25.0 | 0.17247 | 26.3 | 1.10 | 135.9200 | 0.831654 | 0.000050 |
| 0 | 33.0 | 0.28912 | 32.1 | 1.17 | 135.9500 | 0.831589 | 0.000053 |

Figure 4.13: Biaxial report of a typical run analyzed with RS/analyze.

**Model**

$d = A + B \sin^2(Psi)$

**Regression:**

| | A | B |
|---|---|---|
| Value | 8.32E-01 | -1.45E-04 |
| Error | 4.38E-05 | 2.33E-04 |

**Statistics:**

| | R-Square | F-Test | p-value |
|---|---|---|---|
| Value | 0.07 | 0.39 | 5.59E-01 |

**Stress:**

| | Value | CS Error | GOF |
|---|---|---|---|
| Normal | -7.91E+03 | 1.02E+04 | 1.27E+04 |

**Model**

$d = A + B \sin^2(Psi) + C \sin(2Psi)$

**Regression:**

| | A | B | C |
|---|---|---|---|
| Value | 8.32E-01 | -1.70E-04 | -7.60E-05 |
| Error | 1.69E-05 | 8.95E-05 | 1.39E-05 |

**Statistics:**

| | R-Square | F-Test | p-value |
|---|---|---|---|
| Value | 0.89 | 16.26 | 1.20E-02 |

**Stress:**

| | Value | CS Error | GOF |
|---|---|---|---|
| Normal | -9.27E+03 | N/A | 4.87E+03 |
| Shear | -4.14E+03 | N/A | 7.57E+02 |

Figure 4.14: Biaxial and pseudo-triaxial multiple regression models of the data reported in Figure 4.13 created by RS/analyze.

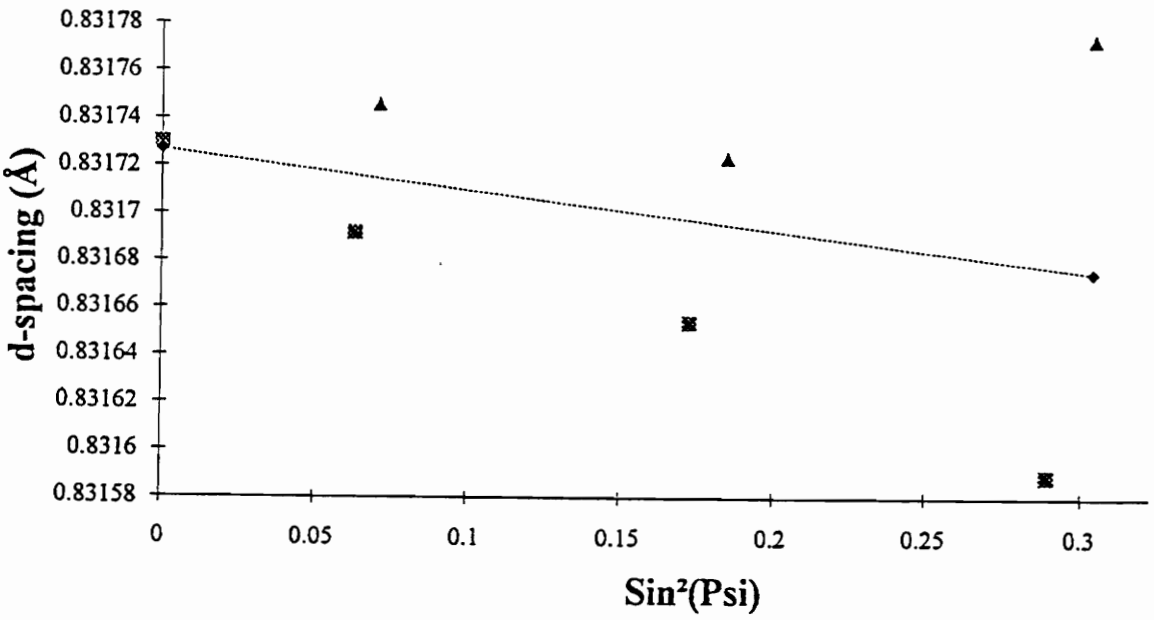


Figure 4.15: Plot of d versus $\sin^2 \psi$ of the data generated in the report shown in Figure 4.13.

A F < 4 means the model is not statistically significant. The P-value on the other hand should generate a low number and this model gives a P-value of .559 indicating a confidence of 49% that the model is correct.

The shear stress model on the other hand has generated statistics that fit well to the data. The $R^2$ value is 0.89, the F-test is large, 16.26 and the level of significance or P-value is 0.012 indicating a confidence interval of 98.8%. Therefore, we accept the hypothesis that the shear stress model gives the best fit to the data.

The data is observed to fit well with the shear stress model because of the extra term,

$C \sin 2\psi$ which introduces additional degrees of freedom for the F-test, viz., $df_1$, $df_2$, $df_3$. The additional degree of freedom increases the value of $R^2$ to approach 1.

In some cases the data do not fit well to either model. For instance, the data shown in Figure 4.16 generates the statistics given in Figure 4.17. Since all of the statistical parameters are not optimum, neither model is a good fit which may mean that the data could be grossly scattered as illustrated in Figure 4.18 of sample 1A. Such effects are attributed to X-ray optics errors, grain size, and preferred orientation, more of which are handled by equations 2.9, 2.10, and 2.11 given in Chapter 2.

From the models and data presented here, one can see how important statistics are to data analysis and how crucial it is to correctly interpret XRRSA data.

**Stress Spectra:**

| | | | | | |
|---|---|---|---|---|---|
| **Filename** | 000417.SPC | | **Acquisition Date/Time** | 21-Feb-92 | 19:15:00 |
| **User Def 1** | VENZANT | **User Def 2** | | **User Def 3** | |

**Sample Description :**

alumina Kyocera reference sample, round collimator (2.0mm). Laser trimmed sample #2, scan is in x axis 10mm f center.

| | | | | | |
|---|---|---|---|---|---|
| **Measurement** | **Type** | Psi | **Stress Spectra Count Time (Sec)** | | 120.00 |
| | **Chi Value** | 0.0 | **Tilt Angle Oscillation Range** | | 3.0 |
| | **Phi value** | 0.0 | | | |
| | **Psi Value** | 0.0 | **Slit Resolution in Two_Theta** | | 0 |
| | | | **Collimator Shape/Size** | Round | 2 |
| | **X-Ray Tube** | Copper | | | |
| | **Wavelength** | 1.54180 | **Peak Bounding Range (%)** | | 20 |

**Material:**

| | | | | | |
|---|---|---|---|---|---|
| **Name** | Alumina 96%, (146) Kyo | **ID #** | 19 | **Database** | T |
| **(1+Mu)/E** | 2.210000E-08 | **Anisotropy Factor** | 0.00 | | |

| Detec | Var | Sin^2(Var) | Intensity | FWHM | 2-Theta | d-spacing | St. Dev |
|---|---|---|---|---|---|---|---|
| 0 | -33.0 | 0.30373 | 31.5 | 0.56 | 135.8900 | 0.831762 | 0.000041 |
| 0 | -25.0 | 0.18459 | 29.9 | 0.69 | 135.8900 | 0.831756 | 0.000053 |
| 0 | -15.0 | 0.07110 | 23.8 | 0.64 | 135.9300 | 0.831640 | 0.000034 |
| 0 | 0.0 | 0.00006 | 24.9 | 1.13 | 135.9200 | 0.831674 | 0.000051 |
| 0 | 15.0 | 0.06294 | 26.8 | 1.10 | 135.9400 | 0.831605 | 0.000040 |
| 0 | 25.0 | 0.17273 | 27.6 | 1.07 | 135.8900 | 0.831768 | 0.000078 |
| 0 | 33.0 | 0.28928 | 32.3 | 1.15 | 135.9300 | 0.831649 | 0.000036 |

Figure 4.16: Report of the experiment for sample no. 2.

**Model**

$d = A + B \sin^2(Psi)$

**Regression:**

| | A | B |
|---|---|---|
| Value | 8.32E-01 | 2.85E-04 |
| Error | 4.26E-05 | 2.26E-04 |

**Statistics:**

| | R-Square | F-Test | p-value |
|---|---|---|---|
| Value | 0.24 | 1.59 | 2.63E-01 |

**Stress:**

| | Value | CS Error | GOF |
|---|---|---|---|
| Normal | 1.55E+04 | 8.21E+03 | 1.23E+04 |

**Model**

$d = A + B \sin^2(Psi) + C \sin(2Psi)$

**Regression:**

| | A | B | C |
|---|---|---|---|
| Value | 8.32E-01 | 2.75E-04 | -3.11E-05 |
| Error | 4.38E-05 | 2.32E-04 | 3.61E-05 |

**Statistics:**

| | R-Square | F-Test | p-value |
|---|---|---|---|
| Value | 0.36 | 1.12 | 4.10E-01 |

**Stress:**

| | Value | CS Error | GOF |
|---|---|---|---|
| Normal | 1.50E+04 | N/A | 1.26E+04 |
| Shear | -1.69E+03 | N/A | 1.97E+03 |

Figure 4.17: Biaxial and pseudo-triaxial multiple regression models of the data reported in Figure 4.15.

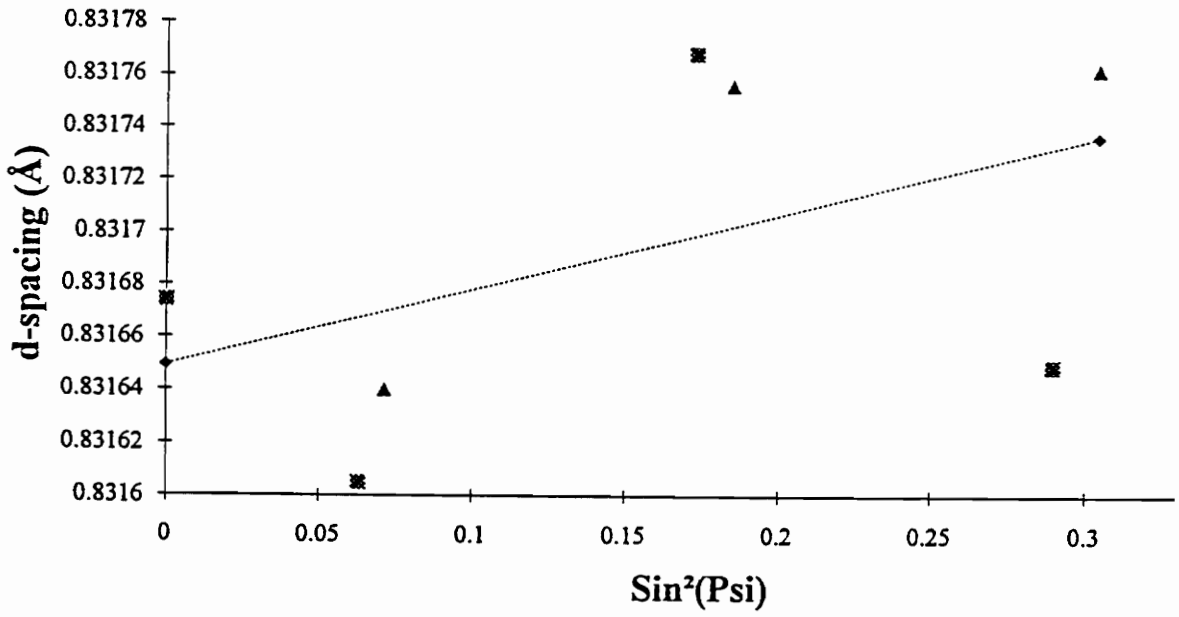


Figure 4.18: Plot of d versus $\sin^2 \psi$ for sample 1A. Note the deviations in the data.

## 4.4 Summary

We have applied a number of materials characterization steps each critical to the understanding of the structure/properties of the alumina substrates as a function of laser machining. Optical microscopy, x-ray radiography and liquid dye penetrant were utilized to examine the surface properties of the substrate before and after laser machining and diamond cutting. Scanning acoustic microscopy and x-ray residual stress analysis were each employed to examine the substrates on a microscopic level. While acoustic microscopy relies on stress waves to generate any slight mechanical deformation due to laser machining, x-ray residual stress analysis relies on strain deformation occurring between atomic lattice planes. ESCA, EPMA and x-ray phase analysis were each used to determine the chemical composition and the phases present in the substrates.

It has been determined from this work that the substrate is a complex multiphase ceramic material composed of a distributed glassy phase (5.8%–7.0%), a magnesium aluminium spinel phase $MgAl_2O_4$ (3.4%) and pores (4.8%). The $MgAl_2O_4$ phase is also randomly distributed. We are not surprised with the amount present since the substrates are manufactured at high processing temperatures and this is an equilibrium phase. ESCA provided chemical spectroscopic data giving volume percents of silica, aluminum, oxygen (as an oxide) and magnesium. EPMA gave both chemical and phase composition as well as supplying information on how the various phases are distributed in the substrates. X-ray phase analysis was used to confirm the $MgAl_2O_4$ spinel phase as determined by EPMA. It is important to note that ESCA and EPMA were in good agreement as to the amount of glass present in the substrates which was determined to be between 5.8 and 7% by volume. The stress state for for non-machined substrates was found to be between 2 to 6 ksi $\pm$ 4 ksi.

Statistics and data analysis was shown to be a critical part of XRRSA work. Results presented illustrated that the biaxial model may not be the correct model of the data when XRRSA is performed on $Al_2O_3$ microelectronic substrates.

Laser trimming performance and associated laser machining/trimming instruments used in this research will be covered in the next chapter. The two laser systems, the ESI Model 25 and the JK700 lasers will be described and how they were used to laser trim the substrates are given.

# Chapter 5

# LASER TRIMMING OF ALUMINA SUBSTRATES

A general explanation of the laser systems used to machine the subsrates is initially given, and includes the ESI Model 30 and the JK700 400 watt laser; their performance as a function of machining the substrates is covered. The ESI laser was used in the initial round of experiments while the JK700 was used in the final experiments. Since the JK700 laser allowed complete control over laser parameters, it was utilized for most of the laser machining as will be illustrated by the optical micrographs given below.

This chapter will also present results of the effect laser trimming had on the substrates. These results will consist of NDE anlaysis of the ESI laser trimmed substrates which will include radiography, acoustic and optical microscopy, and residual stress analysis. The substrates laser trimmed with the JK700 laser will include optical microscopy as well as residual stress analysis. Dynamic strain gage analysis was an additional technique applied to the substrates trimmed with the JK700 laser. The strain gage results were obtained at several different laser power levels.

In general there are two types of lasers that are optimized for trimming—the $CO_2$-$N_2$-He molecular laser and the Nd-YAG laser. The $CO_2$ molecular laser has good coupling with nonmetals due to its wavelength of 10.6 $\mu$m. This wavelength also has its limitations in focusing (its minimum is 0.001 in). The YAG type laser, however, can be Q-switched (turned on and off) at an astounding rate of 5000 pulses per second. The Q switch properties enhance the power of the YAG type lasers, allowing them to achieve peak outputs higher than molecular lasers. Operating at 1.06 $\mu$m, the YAG's laser energy can be focused to a spot size one tenth that of the molecular lasers; this property makes them well suited for

scribing ceramics [53].

The $Al_2O_3$ substrates used in the research for this thesis were cut using a laser-scribing method and a laser-trimming method of thermal shock spalling (controlled fracturing). The scribing method utilized an ESI Model 25 laser trimming system located in the Hybrid Microelectronics Laboratory at Virginia Tech. The controlled fracturing method utilized a JK700 laser at ITT Gallium Arsenide Technology Center, Roanoke, Virginia. Both were Nd-YAG (neodynium-yttrium aluminum garnet) lasers. The Virginia Tech laser had a maximum output of 30 watts while the ITT laser offered a maximum output power of 400 watts. Nd-YAG dye pump lasers are the lasers of choice when performing resistor or substrate trimming because of their high pulse energy and high repetition rates.

Figure 5.1 illustrates the effect of a laser beam incident on the substrate with an illustration of the temperature profile, distribution and tension compression theoretical plot. Plots of the dynamic strain measurements show similar distribution as this theoretical plot. In general, if the tensile stresses are greater than the critical stress, the material will fracture as we have seen happen while using the JK700 laser operating between .50 to 1.06 Joules.

## 5.1 NDE Results From the ESI Laser

The ESI laser is a general resistor trimmer and substrate scriber laser. Lasers of this type are usually cw-pumped, repetitively Q-switched Nd-YAG lasers. This laser operates at short–pulse duration (about 200 ns) with high peak power pulses, which enables materials to be laser machined and left with a clean material removal finish. An example of a substrate laser trimmed in this manner is shown in Figure 5.2. Note the edges show no irregular patterns do to the trimming process. The Laser parameters for trimming alumina with this system were 15 watts at 1.5 MHz with an interaction speed of about 3 mils per second.

The NDE techniques outlined in the NDE section of Chapter 4 are presented in this section for x-ray radiography, microscopy (optical metallography, and SEM), acoustic microscopy, liquid penetrant, and EPMA.

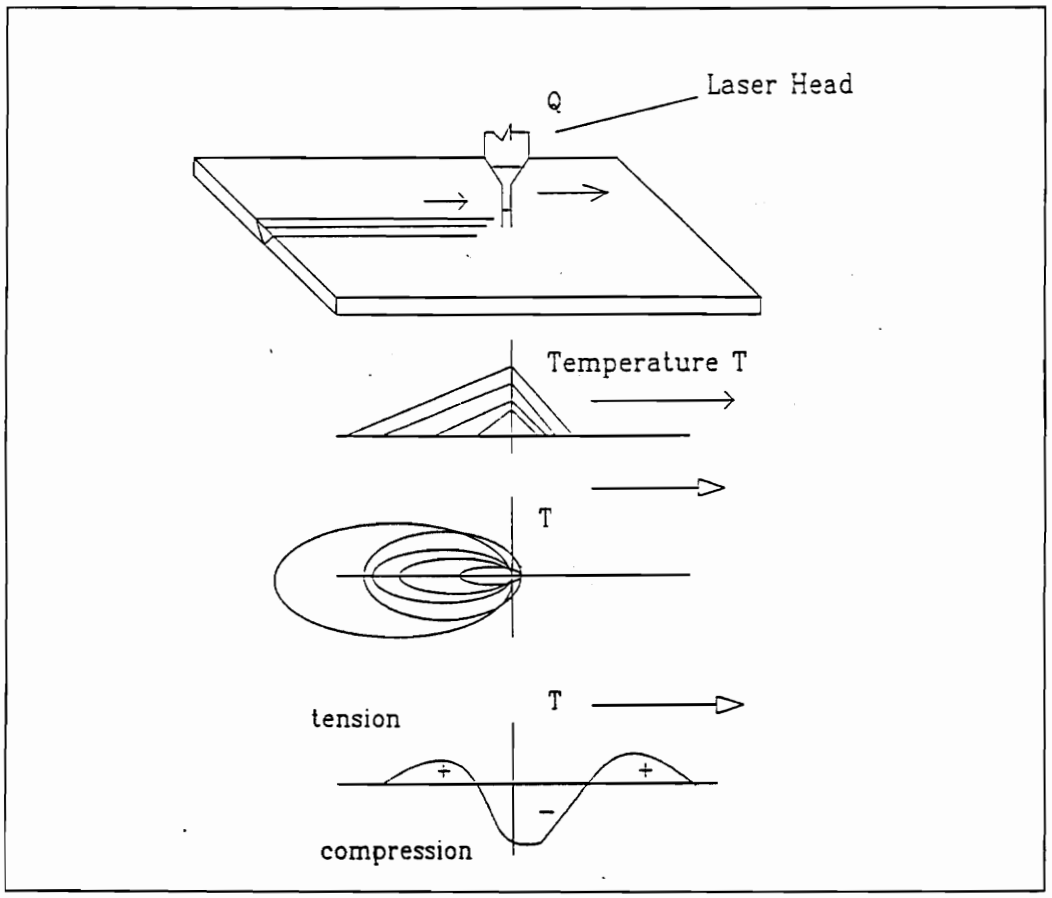


Figure 5.1: General description of laser trimming substrates. Thermal and stress distributions are also illustrated. The last figure illustrates tension and compression stresses perpendicular to the laser beam trace in the top figure.

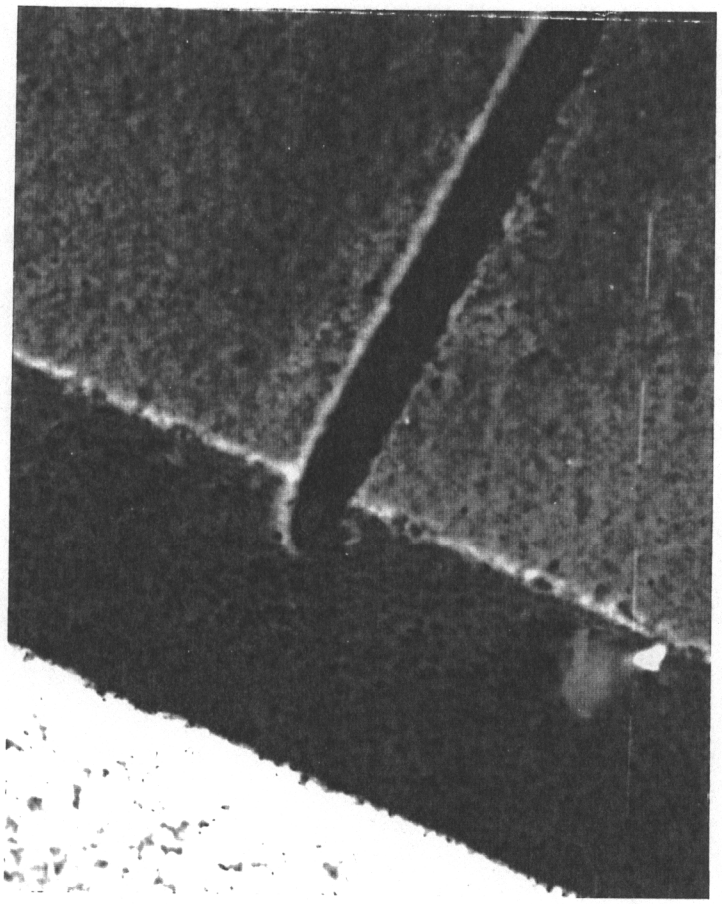

Figure 5.2: Alumina substrate laser trimmed with the ESI Model 25 system.

X-ray radiography results are illustrated in Figure 5.3. This figure illustrates radiographs of two samples that have been diamond cut and laser trimmed. This technique was used to search for any cracks due to the laser or the diamond cutting; no major defects were observed. The dye penetrant and radiography techniques may have been more effective if used simultaneously, by the use of the so called "dye enhanced radiography technique." With this technique, the characterization sequence could proceed in the following manner:

- apply the dye to the substrates; view under an inspection microscope.
- if flaws are not detectable, perform X-Ray radiography on the substrate with the penetrant applied.

With the combined techniques, cracks may have revealed themselves.

The acoustic micrograph illustrated in Figure 5.4 is a micrograph of a subsrate laser trimmed with the ESI laser. This technique was used to discern microscopic anomalies in the substrate and again results were negative. There is however, a small region adjacent to the melt zone highlighted by the acoustic microscope image analysis. This small region parallel to the melt/hardening zone could be the outline of the HAZ.

## 5.2 Residual Stress Results from the ESI Model Laser

To understand the nature of the residual stresses created from the use of laser machining, two parallel lines 6 cm apart were laser trimmed with the ESI Model 25 system. This is illustrated in Figure 5.5. X-ray residual stress measurements were made on the front and back of the substrates.

Only nearly stress-free samples were chosen for the laser trimming process in order to observe any increases in the residual stress due to laser trimming process. After laser trimming with the ESI Model 25 laser in two locations as shown in Figure 5.2, the laser trimmed samples were characterized using XRRSA in 11 positions that were 2mm apart in three different locations. The measurements were performed in both the longitudinal and transverse directions. The data generated are averages of three X-ray residual stress

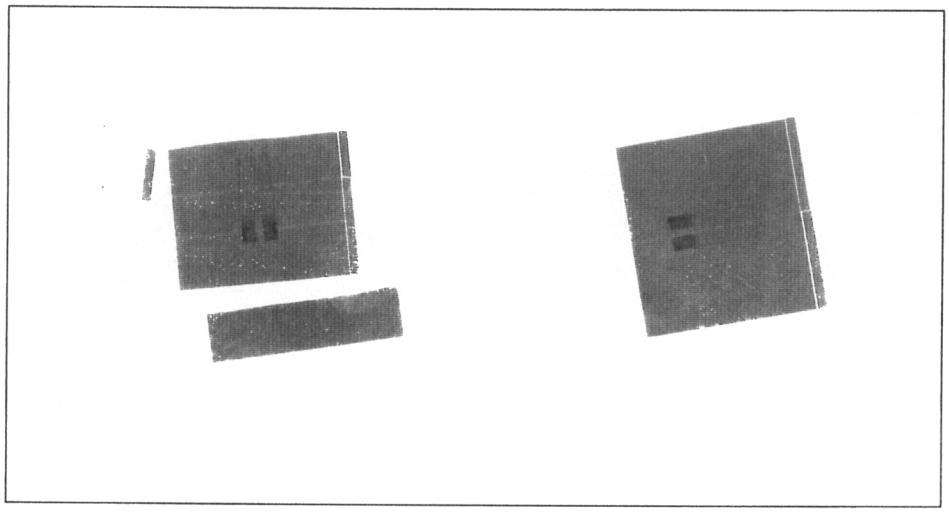

Figure 5.3: X-ray radiograph of samples that were diamond cut, as shown in the breaks and laser trimmed with the JK700 With this technique no flaws are visible. This may be attributed to the lack of resolution of this machine, since it was not a microfocus device.

measurements made along the aforementioned directions. The back side of the samples were also measured but only in 5 positions 4mm apart. Figures 5.7 and 5.8 show the results of these measurements when locations 1 and 3 are compared. The laser power delivered to the samples was 14-15 watts at 0.4 kHz. Initially it was anticipated that a steep stress gradient would appear near the heat affected zone of the substrates as is common in the HAZ of welded metals see Figure 5.6. This appears not to be the case here. Therefore, an average of the residual stress data is shown by the dashed line.

Statistically the stresses in Figure 5.7 and 5.8 are isotropic across the substrate. Stress measurements performed on the reverse side are also uniform as seen in Figures 5.9 and 5.10.

The data generated in the plot of Figure 5.7 and 5.8 are averages of three measurements. The initial stress data of this sample prior to laser trimming were about $\pm 6$ ksi. After laser trimming the substrates into the two parallel sections as indicated by the arrows, x-ray residual stress measurements showed GF statistics as low as 11 ksi and as high as 13 ksi. while counting statistics as low as 10.6 and as high as 20.7 were noted. It was previously

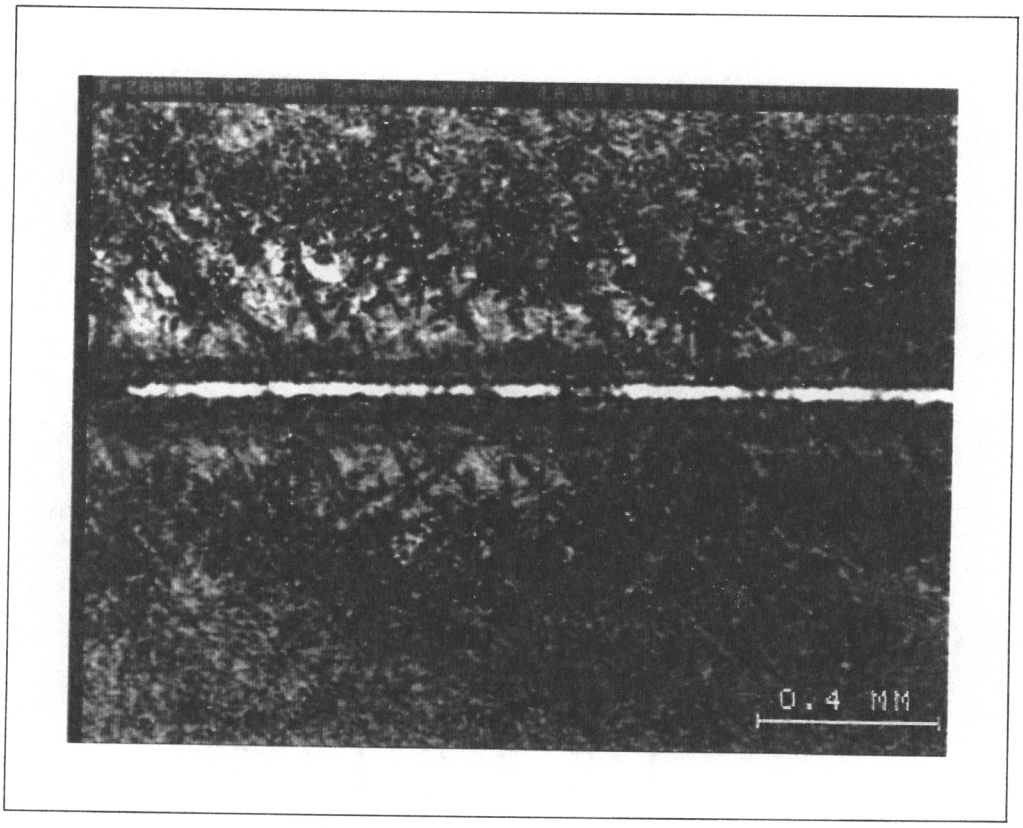


Figure 5.4: Acoustic micrograph of an alumina substrate laser trimmed with the ESI Model laser. Note the area at the very edge of the laser trimmed lines. This may be attributed to the HAZ.

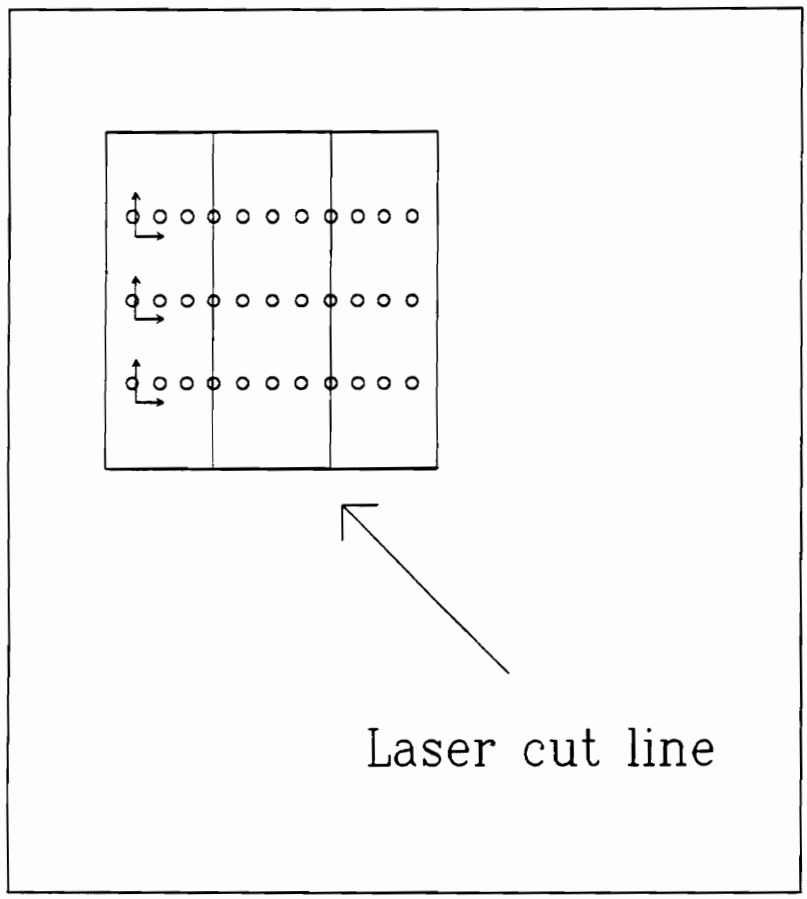


Figure 5.5: Schematic of a substrate showing laser cut lines and the location X-ray residual stress measurements.

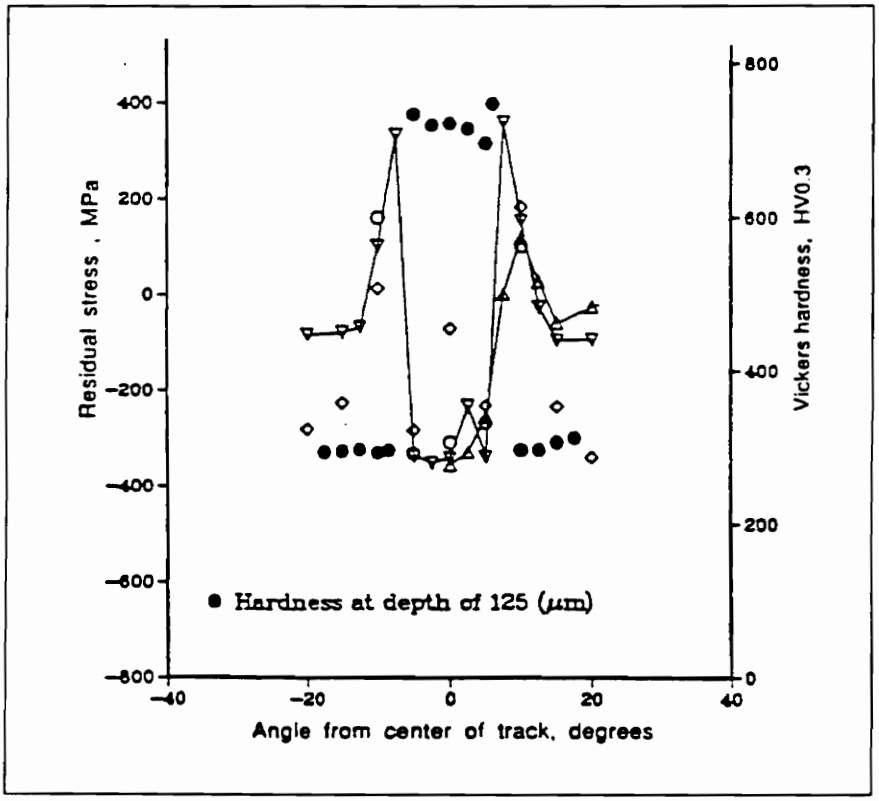


Figure 5.6: Longitudinal stress distribution of laser hardened track in Cr-Mo steel [28].

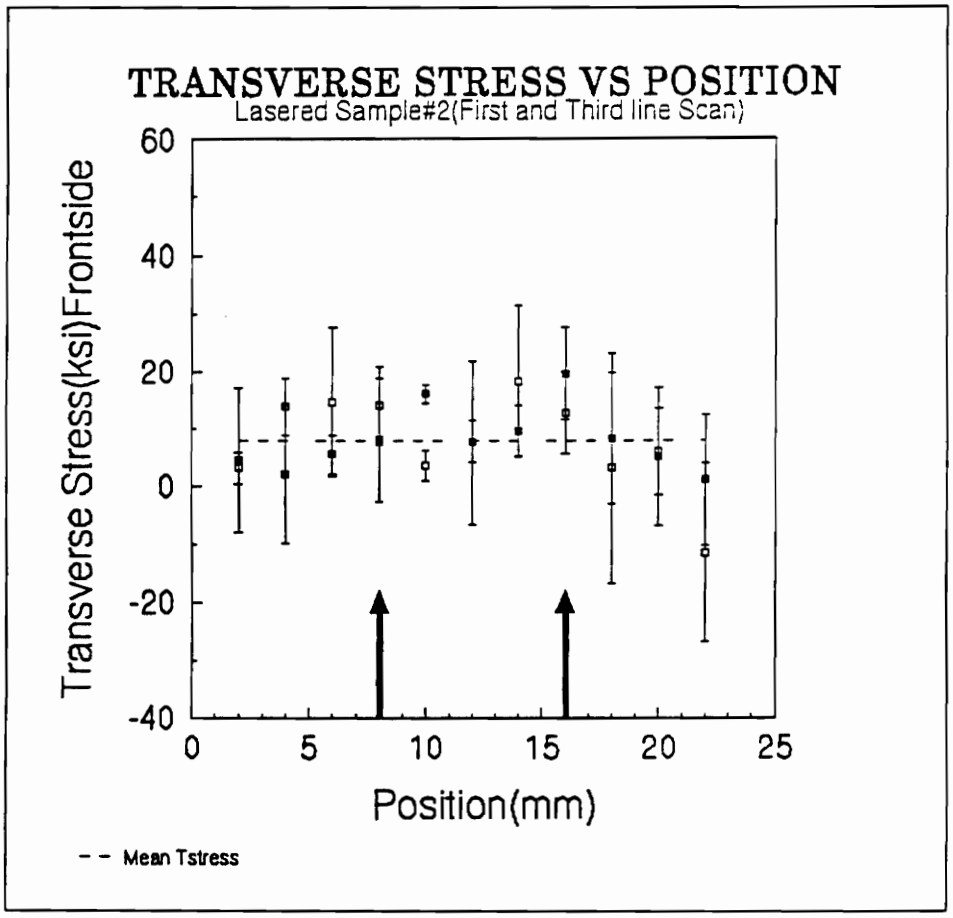


Figure 5.7: Transverse X-ray residual stress measurements of the first (open squares) and third (closed squares) lines of alumina laser trimmed with the ESI laser (front side).

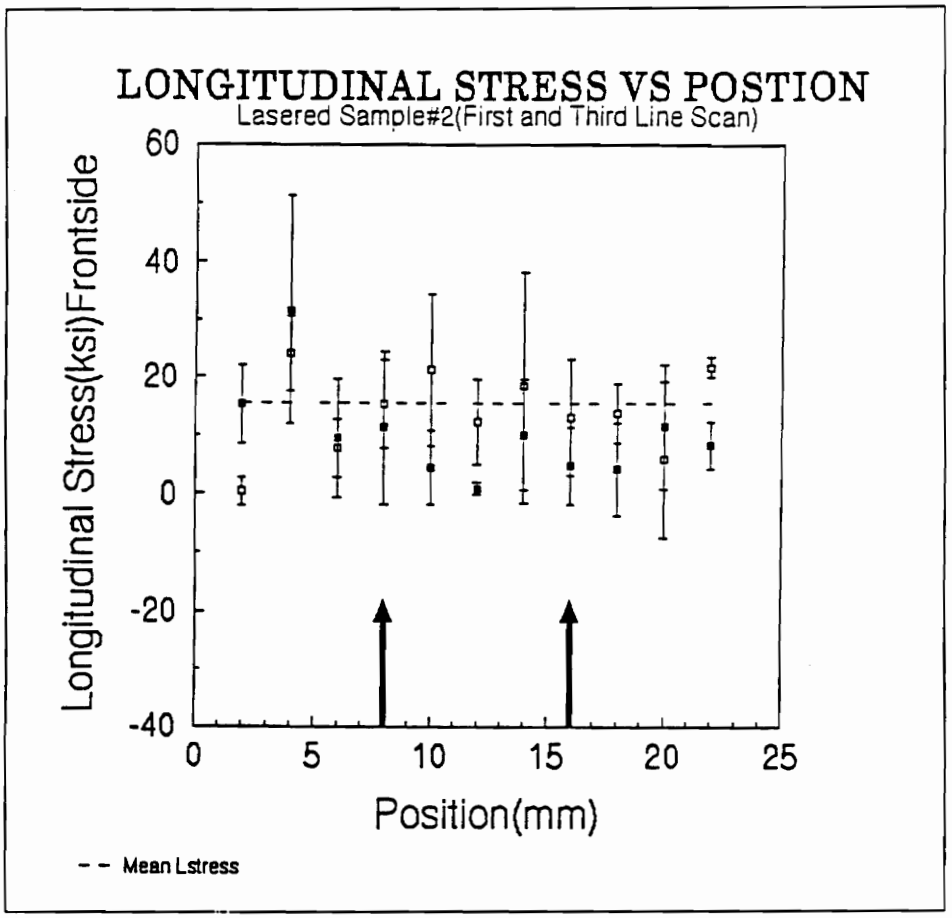


Figure 5.8: Longitudinal X-ray residual stress measurements of the first (open squares ) and third (closed squares) lines of alumina laser trimmed with the ESI laser (front side).

stated that the counting statistics (CS) errors are those which would be expected if only errors due to finite measuring times of the experiment were involved. The GF errors are those associated with the fit of the biaxial and triaxial stress models (given in Chapter 2) to the data. That the GF errors are approximately the same as the CS errors (Table 1) implies that equation 5.1 below is an acceptable model of the data, but the errors could be reduced significantly by extending the measuring times. CS errors and GF statistics stress values are illustrated in Table 5.1. As stated above, it was anticipated that larger stresses would form in or near the HAZ; such effects were not apparent from the results of the data analysis. Steep stress gradients were anticipated for the laser trimming process as typically seen for metals since laser trimming the substrates may be seen as a point heat source performing material removal at high heats of fusion. In Figure 5.6 steep stress gradients are seen near the heat affected zone [28].

As noted earlier, The equation that relates the residual stress by the variation of the d-spacing for the shear stress case is given by [26]:

$$\frac{\mathrm{d}_{\phi,\psi} - \mathrm{d}_{\phi,0}}{\mathrm{d}_0} = \frac{1+\nu}{\mathrm{E}}[\sigma_{11}\sin^2\psi + \sigma_{13}\sin 2\psi] \tag{5.1}$$

where $d_{\phi,\psi}$ represents the d-spacing of the planes forming the angle $\psi$ with the material's surface in the $\phi$ direction, $d_{\phi,0}$ is representative of the d-spacing for $\psi = 0$, the unstressed lattice planes are given by $d_0$, $\nu$ and $E$ are Poisson's ratio and the X-ray elastic modulus respectively, $\sigma_{11}$ is the normal stress and $\sigma_{13}$ represents the shear stress term. We have assumed the stresses normal to the sample were zero, viz., $\sigma_{33} = 0$. Further details of this technique are given section 2.4.2.

### 5.2.1 Statistics and Data Analysis

A variety of statistical techniques were applied including multiple regression, Kolmogorov-Smirnoff, and analysis of variance for substrate correlations between the location of the laser cut and the resultant residual stresses. No correlations could be found [27]. Therefore, it may be concluded that the thermal shock resistance properties of the ceramic substrates

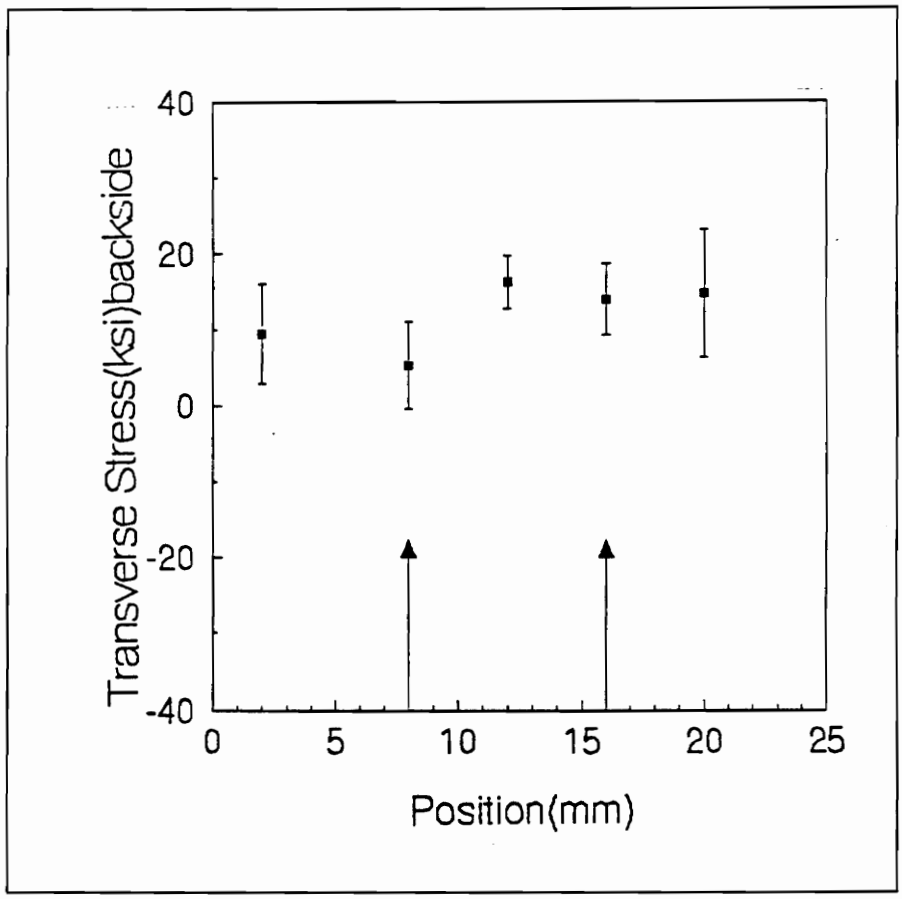


Figure 5.9: Transverse X-ray residual stress measurements along the third line for alumina laser trimmed with the ESI laser (back side).

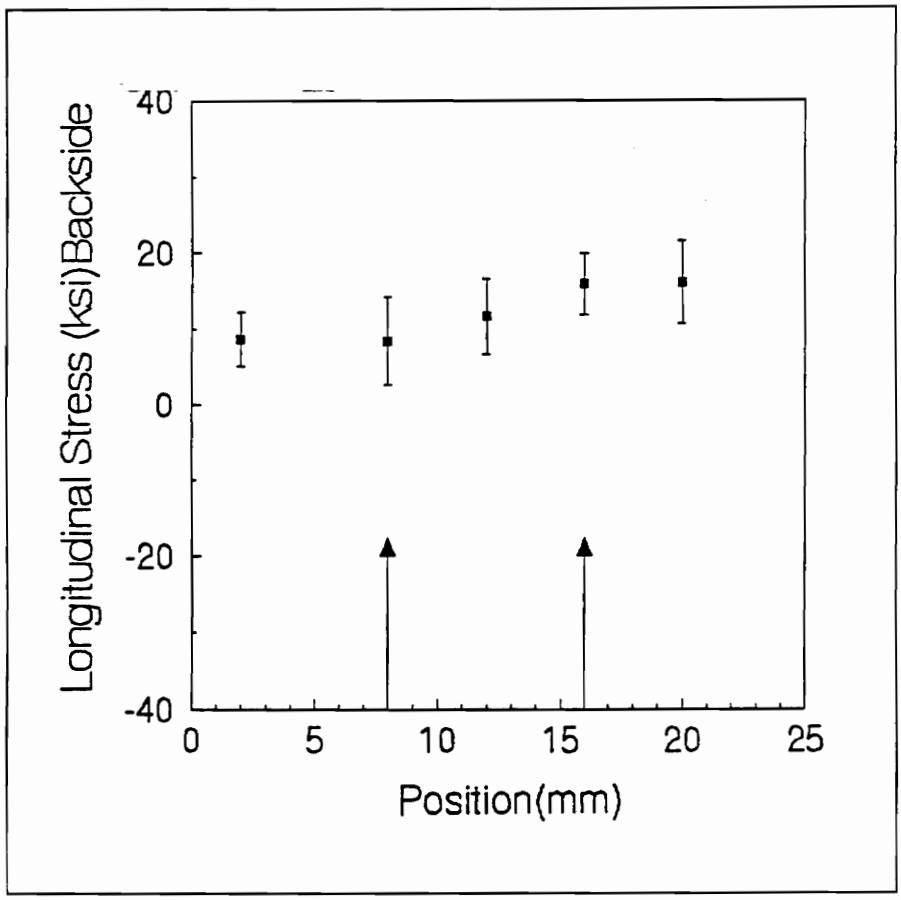


Figure 5.10: Longitudinal X-ray residual stress measurements along the third line for alumina laser trimmed with the ESI laser (back side).

Table 5.1: Descriptive statistics summary of the measurements

| Direction | Means Stress | CS | GF | Line | Sample |
|---|---|---|---|---|---|
| Longitudinal | 10.1 | ±10.6 | ±12.7 | 1 | 2 |
| Transverse | 8.0 | ±14.0 | ±10.5 | 1 | 2 |
| Longitudinal | 15.3 | ±19.4 | ±16.4 | 3 | 2 |
| Transverse | 7.8 | ±14.0 | ±12.0 | 3 | 2 |
| Longitudinal | 11.3 | ±17.0 | ±8.8 | 1 | 12 |
| Transverse | 13.8 | ±20.7 | ±13.2 | 1 | 12 |
| Longitudinal | 12.4 | ±12.7 | ±10.0 | 3 | 12 |
| Longitudinal | 11.6 | ±11.2 | ±8.6 | 3 | 12 |

some how redistributes the thermal shock received from the ESI laser by some intrinsic physical mechanism. This mechanism will be discussed in sections to follow and in Chapter 6

For the analysis of data generated for the X-ray residual stress measurements, three techniques were utilized: multiple linear regression, ANOVA (Analysis of Variance), and Kolmogorov-Smirnov. Least squares regression was used to obtain the stress from the slope of the least squares fit line of the experimental data. Multiple linear regression was used to develop a model of the stress distribution after the samples were laser trimmed. ANOVA was employed to test for the null hypothesis for comparing more than one population mean for residual stress distributions across the alumina substrates in three distinct locations. Kolmogorov-Smirnov non-parametric statistics were used for the same purpose; however, this technique permitted a larger variation in population comparisons.

### 5.2.2 Multiple Linear Regression

Multiple linear regression was utilized to test for the development of a model for the stress distribution of the laser trimmed samples. Multiple regression is a least squares test in which the dependent variable is expressed in a model as a polynomial of independent variables (quantitative and independent). Furthermore, for the multiple regression model there is more than one term in the model.

To develop models of the stress distributions as measured by X-ray diffraction, both linear and multiple regressions were used. Figure 5.11 shows the different models fit to the same X-Ray residual stress data. From the F and T-tests of each model, it is clearly seen that the higher order models are not good representations of the data. For statistical significance, F should be greater than about 4. The F-test statistics are low (average low is 2 and the high is only 5). The F test illustrates the relationship between the stress versus position. A stronger test is the $R^2$ value. If the $R^2$ is near 1 then a good model exist for the data; in the cases for these results a good model could not be found. Therefore we conclude that the linear regression is the best model to describe these data and the stresses are therefore uniformly distributed across the substrates.

### 5.2.3 ANOVA

ANOVA was used to test various models of the residual stress. Again, linear or constant models were found to give the best representation of these data.

### 5.2.4 Kolmogorov-Smirnov Two–Sample Test

A Kolmogorov-Smirnov Two–Sample Test or KS2 was used to test whether two independent samples (or two populations from the same distribution) belonged to the same population. This test was significant since it would give a better picture of whether the stress distribution across the laser trimmed substrates was isotropic or anisotropic. This statistical test procedure was ideal for the laser trim analysis. The KS2 procedure permitted two and one tail tests. The two tailed test can be used to check for variance in location (central tendency), skewness, dispersion, etc. One tail tests are used to check if the data from one population has a large random variation (stochastic) with respect to data from a second population. For instance, for the residual stress data analyzed in this research, tests were performed to see if the stress distribution is stochastically different from another stress distribution located 6 mm away (i.e., to ascertain whether these stresses in general are higher or lower than stresses of the other location).

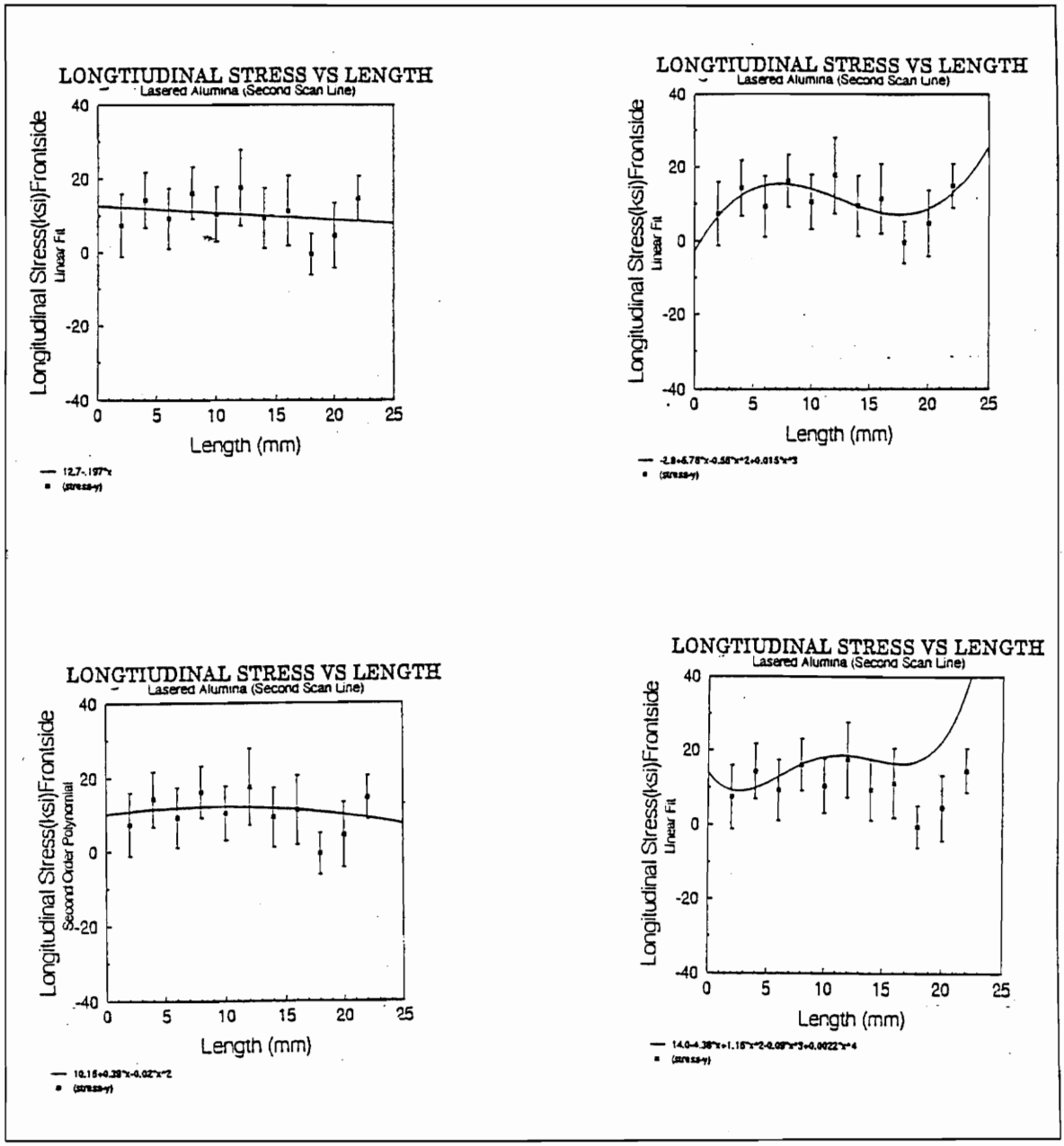


Figure 5.11: Polynomial fits to the stress distributions across the alumina substrates.

### 5.2.5 KS2 Method and Procedure

The procedure for the KS2 technique involves developing a cumulative distribution of the data chosen by using the same intervals or conditions for the two distributions (in our case two stress distributions) and follows that found in Siegel [64]. The next step is to subtract from each interval one step function from the other. The purpose is to look for the largest of the observations after subtraction and then to test for the null hypothesis $H_0$, viz., that the two stress distributions belong to the same populations. Therefore, for comparing one data set to a known cumulative distribution function $P(x)$, the KS statistic is

$$D = \max_{-\infty<x<\infty} \mid S_{N_{(x)}} - P(x) \mid \tag{5.2}$$

and for comparing two different cumulative distribution functions $S_{N_{1(x)}}$ and $S_{N_{2(x)}}$, the KS statistic is

$$D = \max_{-\infty<x<\infty} \mid S_{N_1} - S_{N_2} \mid \tag{5.3}$$

where $S_{N_{(x)}}$ represents the data in the population.

The test statistic developed from these functions is $D_{m,n}$, where m and n are the observed range of any two populations compared. From the results applied to the residual stress data, the null hypothesis $H_0$ that any two stress distrbutions were different was rejected. This was due to the fact that any time any two stress distribution were compared using the KS2 test, it showed that the two distributions belonged to the same population. Therefore, based on all statistical models, it is concluded that the stresss across the substrates are uniform.

## 5.3 NDE Results From the JK700 Laser

The JK700 laser system is a general purpose instrument used primarily for laser welding of metallic workpieces. We have shown that it can also be used for laser trimming

ceramic parts, viz., thick substrates as well. It was used due to its precise control over laser parameters as well as its accuracy and stability.

The laser parameters were:

- power = 15% of maximum power (400 watts)
- pulse height = 1.06 joules/pulse
- pulse width = 3 ms
- pulse rate = 18 Hz
- beam diameter = 30 mils

The parameters presented above can be adjusted in order to achieve optimum laser trimming. A typical laser trim pattern is shown in Figure 5.12. The reader should compare this micrograph with Figure 5.2.

After laser trimming the substrates at 1.06 Joules, three distinct microstructure regions were seen, a melt zone, a region of surface spalling, and a recrystallization zone (see Figure 5.13). The melt zone showed extensive microcracks distributed radially but along the direction of the laser beam translation. Similar results were seen by Gardner and Beauchamp [46] except in the recrystallization region. The bulk material adjacent to the melt zone tended to cut off or stop cracks from propagating from the laser interaction path. This is most likely a fusion zone between the bulk and melt areas sealing off cracks or forcing them in the preferred direction of the laser beam, possibly by serving as hardening zones. An example of this effect is seen in Figure 5.14.

Optical microscopy was used to ascertain microstructure before and after laser processing. Optical techniques included low to high magnification inspection (10X-500X), a polarizing microscope and optical metallographic high magnification inspection. Figure 5.15 shows an optical micrograph of a laser trimmed $Al_2O_3$ substrate.

Four samples were laser trimmed at four different power levels; 0.75, 0.50, 0.25 and 0.1 joules. Dark field optical metallographic micrographs are shown in Figures 5.16 through

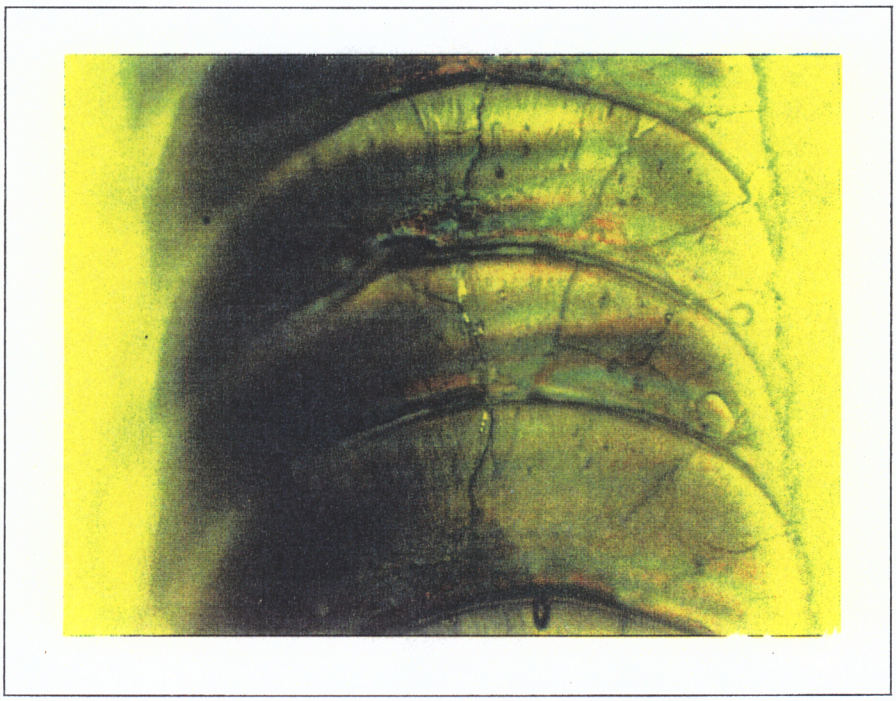

Figure 5.12: Alumina substrate laser trimmed with the JK700 400 Watt Laser. Note the pulsed spacing and cracks generated from easy separation.

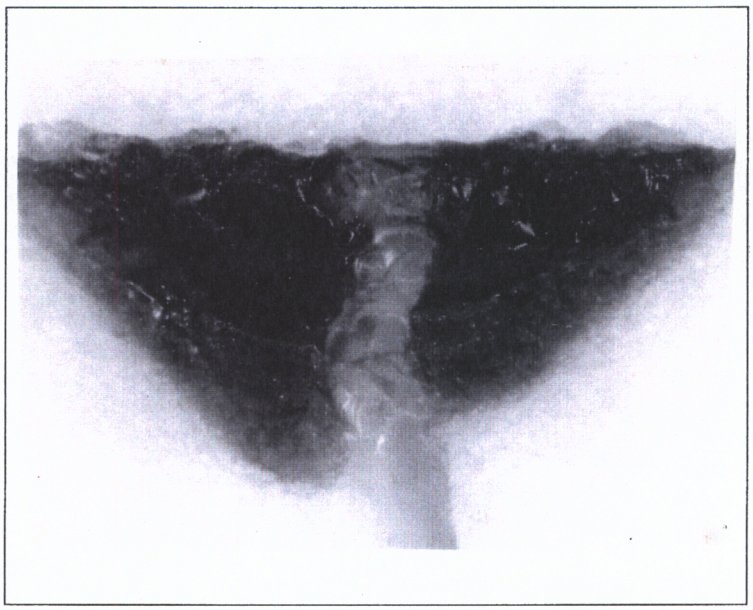

Figure 5.13: Optical micrograph of the side view of a substrate laser trimmed with the JK700 laser. Note the three phases created from the laser effect (see text for explanation).

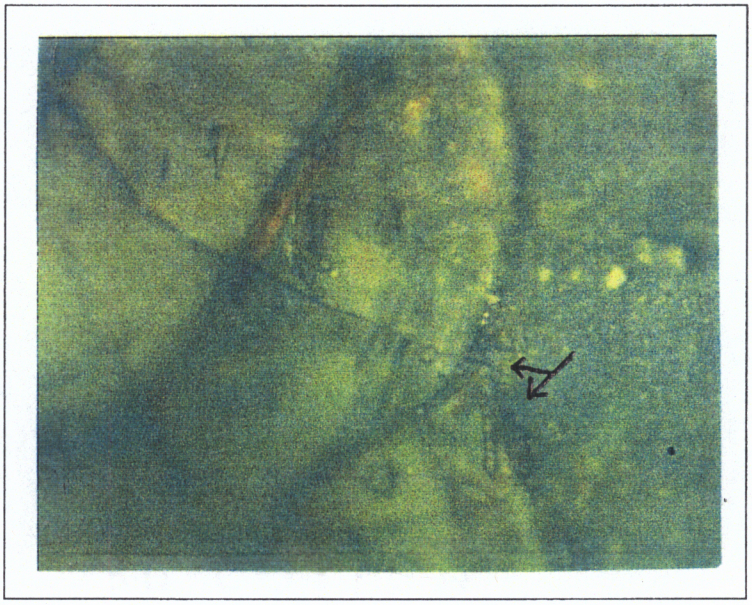

Figure 5.14: Example of a cracks path being altered by the melt/hardening zone.

5.20 of the cross sections of the different laser trim passes as a function of laser power. As expected, the higher the laser power the larger the kerf width and depth. The kerf or laser trim pattern length to depth section is about 23 mils for the highest laser power (1.06 Joules). Figure 5.17 shows a cross section at 0.75 Joules. From this figure, it is seen that the kerf depth broadens as the laser power is reduced. Figures 5.18 and 5.19 also illustrate this broadening which is more profound. These micrographs illustrate the importance of using a beam with sufficient power density so that a proper kerf depth is made to effectively separate the ceramic substrate. Each sample showed varying strain behavior which could be attributed to laser power, sample constraint factor (some were clamped and some were not), and strain gage adherence. The section on strain behavior will illustrate in situ the effect of laser power variations on the substrates.

Figures 5.19 and 5.20 show that laser trimmed patterns for samples K3 and K4 have the familiar cracks which are created when the laser impinges the substrate and when the next pulse starts the first pulse cools creating a crack propagation sequence. The fused edges of the tracks or boundary not affected by the laser pattern assists in the cooling process also.

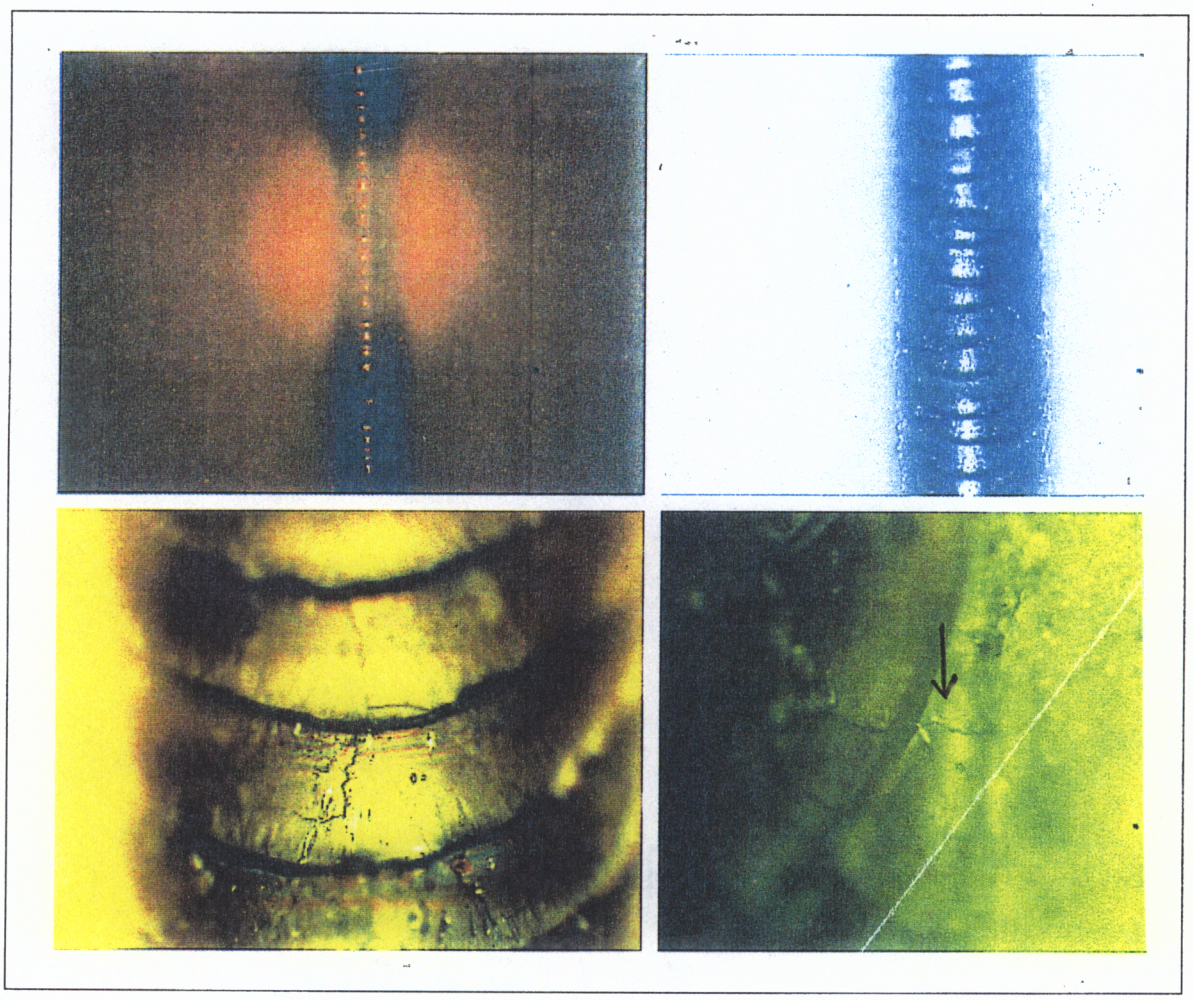

Figure 5.15: Surface optical micrograph of a laser trimmed alumina substrate. Note the pulse-like train of melted material in the surface at 10X (upper left corner) and 50X magnification (upper right corner). The lower left corner illustrates at 250X magnification the stress raising cracks created from the 400 Watt Nd-YAG laser, operating in pulsed mode. The lower right figure at 500X magnification shows how a crack has moved perpendicular with respect to the major crack path.

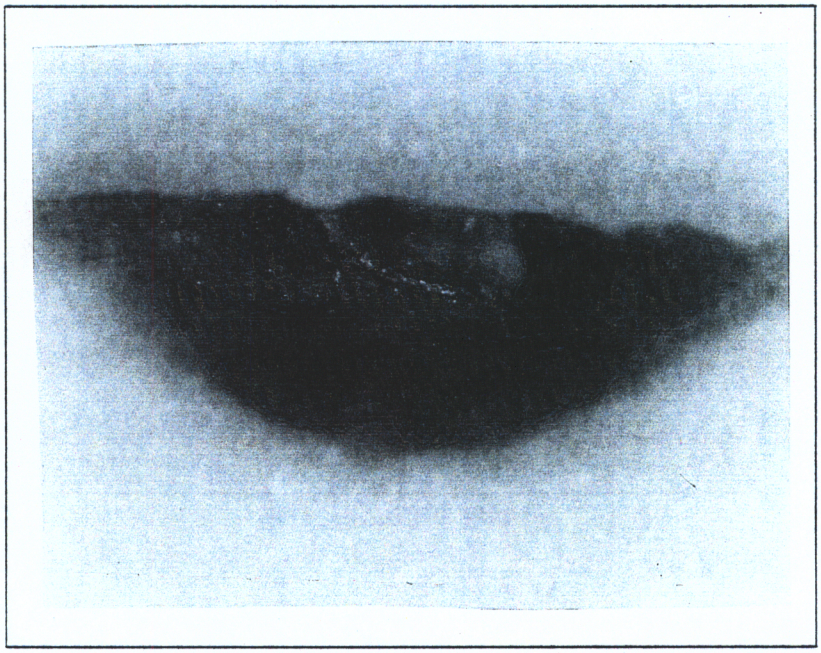

Figure 5.16: Optical micrograph cross section of an alumina substrate laser trimmed with 0.75 joules of laser power (JK700).

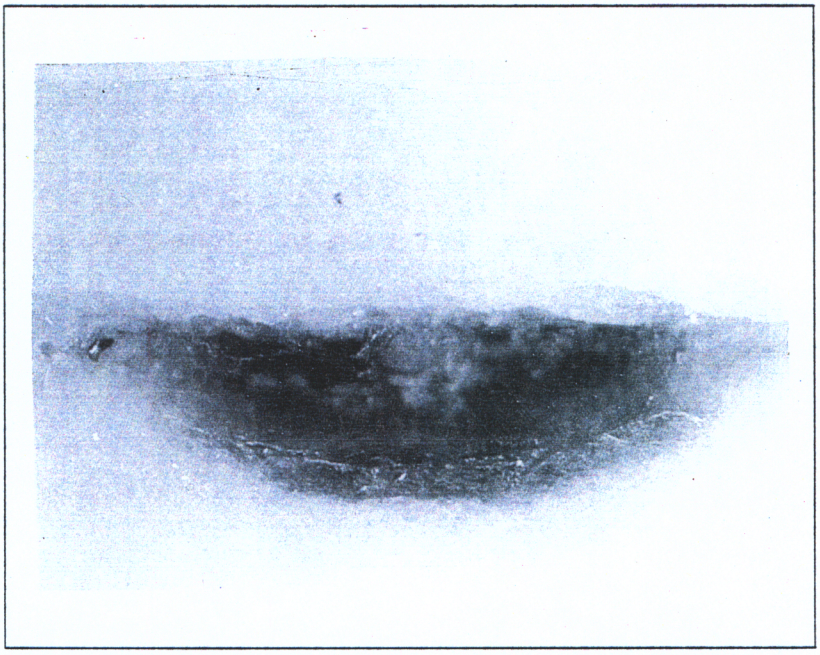

Figure 5.17: Optical micrograph cross section of an alumina substrate laser trimmed with 0.50 Joules of laser power (JK700).

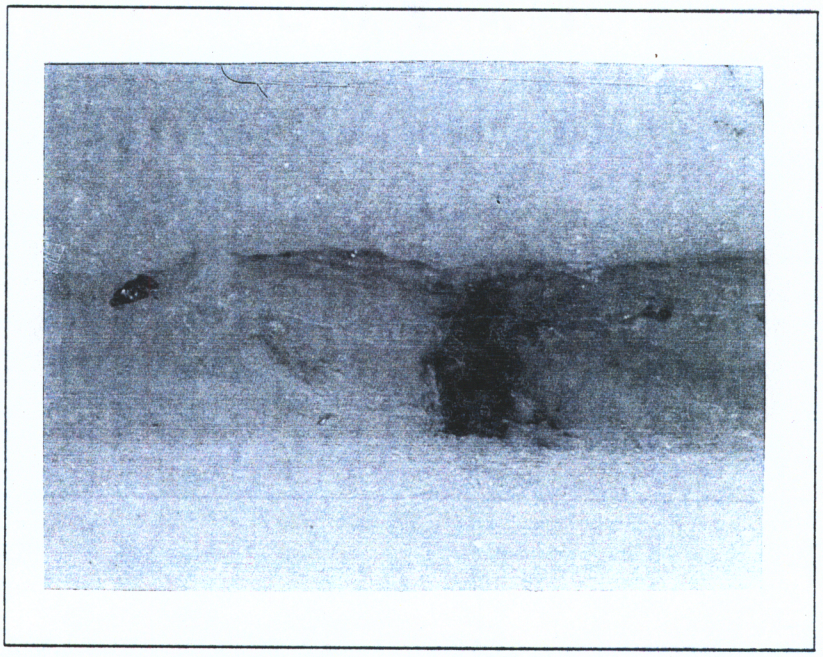

Figure 5.18: Optical micrograph cross section of an alumina substrate laser trimmed with 0.25 Joules of laser power (JK700).

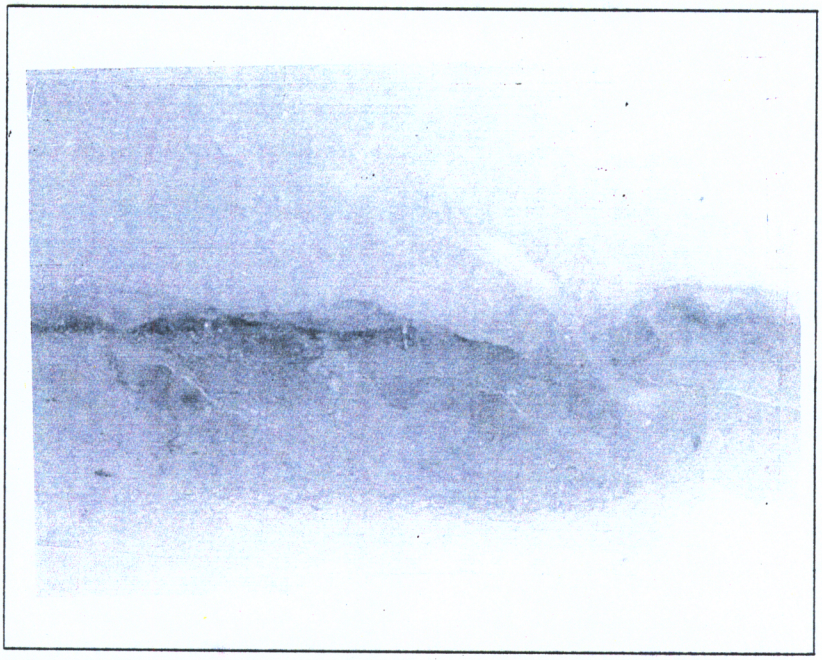

Figure 5.19: Optical micrograph cross section of an alumina substrate laser trimmed with 0.1 Joules of laser power (JK700).

Table 5.2: Descriptive statistics summary of JK700 laser stress measurements.

| Direction | Means Stress | CS | GF | Line | Sample |
|---|---|---|---|---|---|
| Transverse(L) | 13 | ±5.0 | ±10.5 | $C$ | $2k$ |
| Transverse(R) | 9.0 | ±5.4 | ±13.6 | $C$ | $2k$ |
| Transverse(L) | 13 | ±5.0 | ±7.8 | $C$ | $3k$ |
| Transverse(R) | 17.6 | ±5.0 | ±10.5 | $C$ | $3k$ |
| Transverse(L) | 14.3 | ±5.4 | ±10.7 | $C$ | $4k$ |
| Transverse(R) | 14.4.8 | ±5.4 | ±13.5 | $C$ | $4k$ |

It can be seen that the material shows a vaporization and melting sequence on heat input. Figures 5.21—5.23 illustrate the lack of coupling in samples K3 and K4 due to the lack of laser energy coupling to the surface. Samples K3 and K4 also show that at lower incident laser power delivered to the substrates, more chaotic crack branching occurs.

## 5.4 Residual Stress Results of the JK700 Laser Trimming

X-ray residual stress measurements of the samples trimmed with 1.06 joules of laser input energy are shown in Figures 5.24—5.26. These are measurements for a single residual stress measurement pass. Each sample was measured in six positions, all 3 mm from one another. The stresses are essentially isotropic and all data are within $2\sigma$ of the measurement. A summary of the data is given in Table 5.2. The CS are a factor of two lower than the GOF which is very reasonable as compared to previous measurements. The improved statistics are a result of increasing the detector counting times by a factor of two thus generating improved statistics.

The data in Table 5.2 are averages of data on the left and rightside of the three samples. These data are also averages of three x-ray residual stress measurements (with improved CS and GF statistics) at left positions or right positions of the substrates.

A problem throughout the stress measurements was that tensile stresses were measured on both the front and backsides of the substrates. Two processes may be operating here, to generate such stress distributions; the difference in volume expansion of the glassy phase or

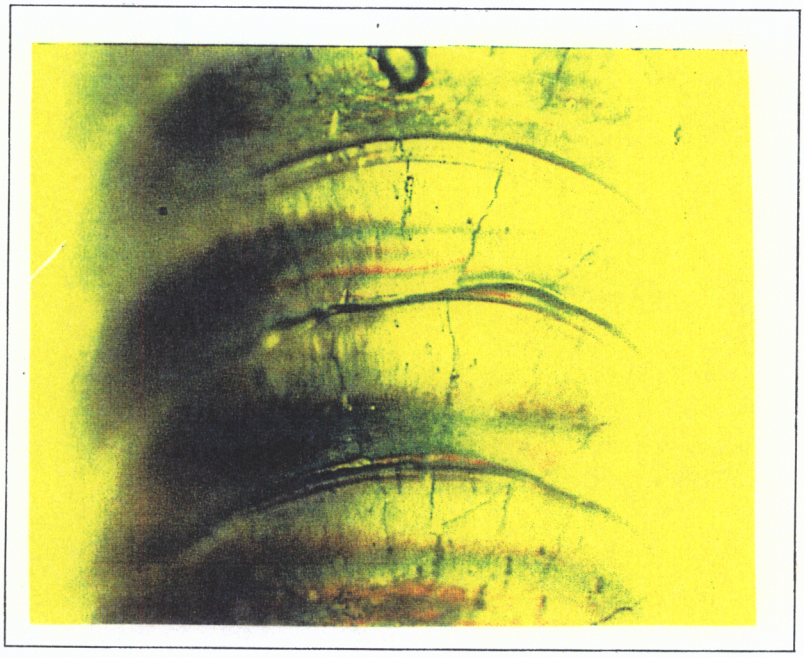

Figure 5.20: Optical micrographs of sample K1 laser trimmed with .75 Joules of laser power (ITT JK700 laser).

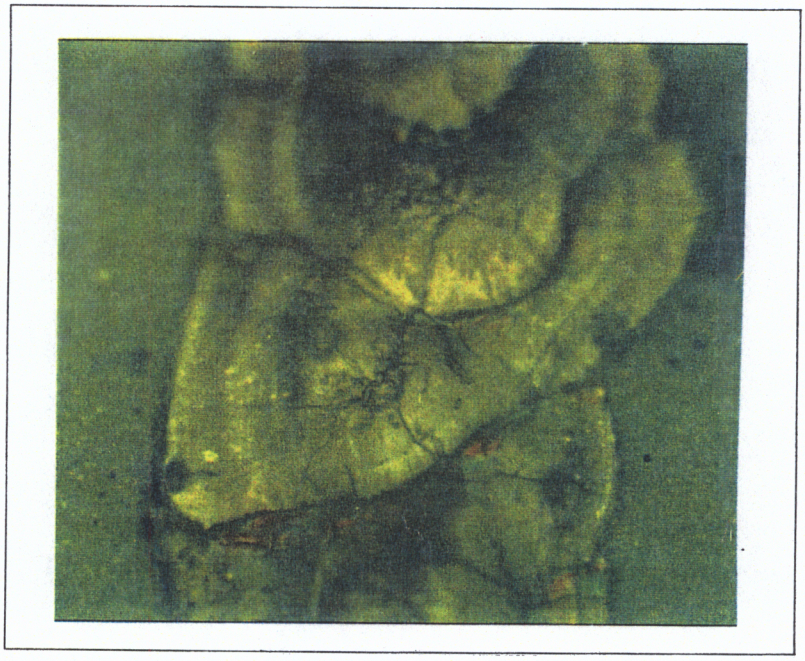

Figure 5.21: Optical micrographs of sample K2 laser trimmed with 0.50 Joules of laser power (ITT JK700 laser).

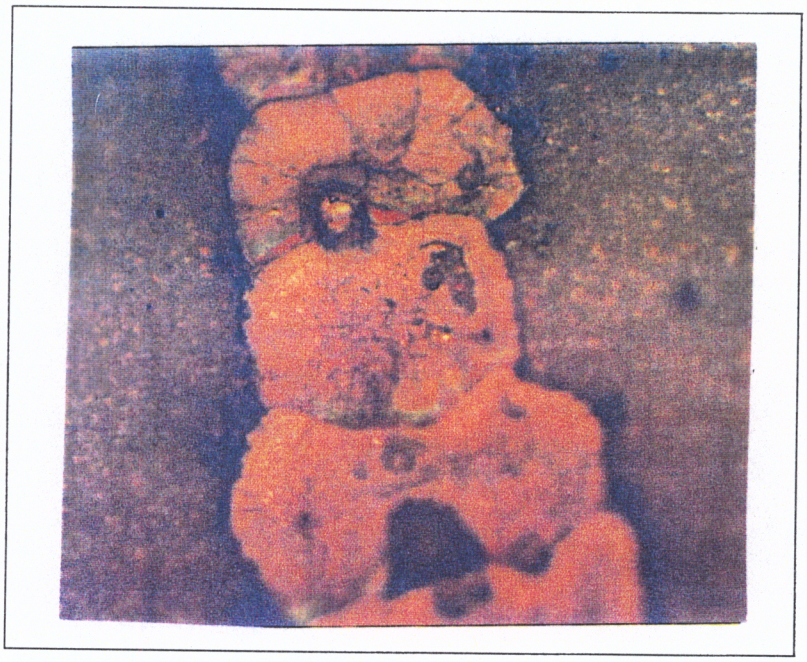

Figure 5.22: Optical micrographs of sample K3 laser trimmed with 0.25 Joules of laser power (ITT JK700 laser).

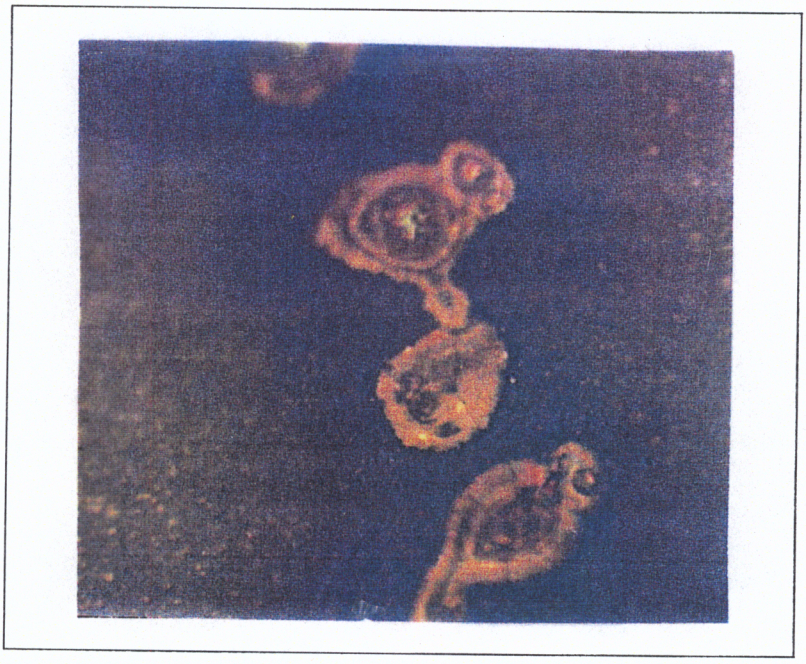

Figure 5.23: Optical micrographs of sample K4 laser trimmed with 0.1 Joules of laser power (ITT JK700 laser).

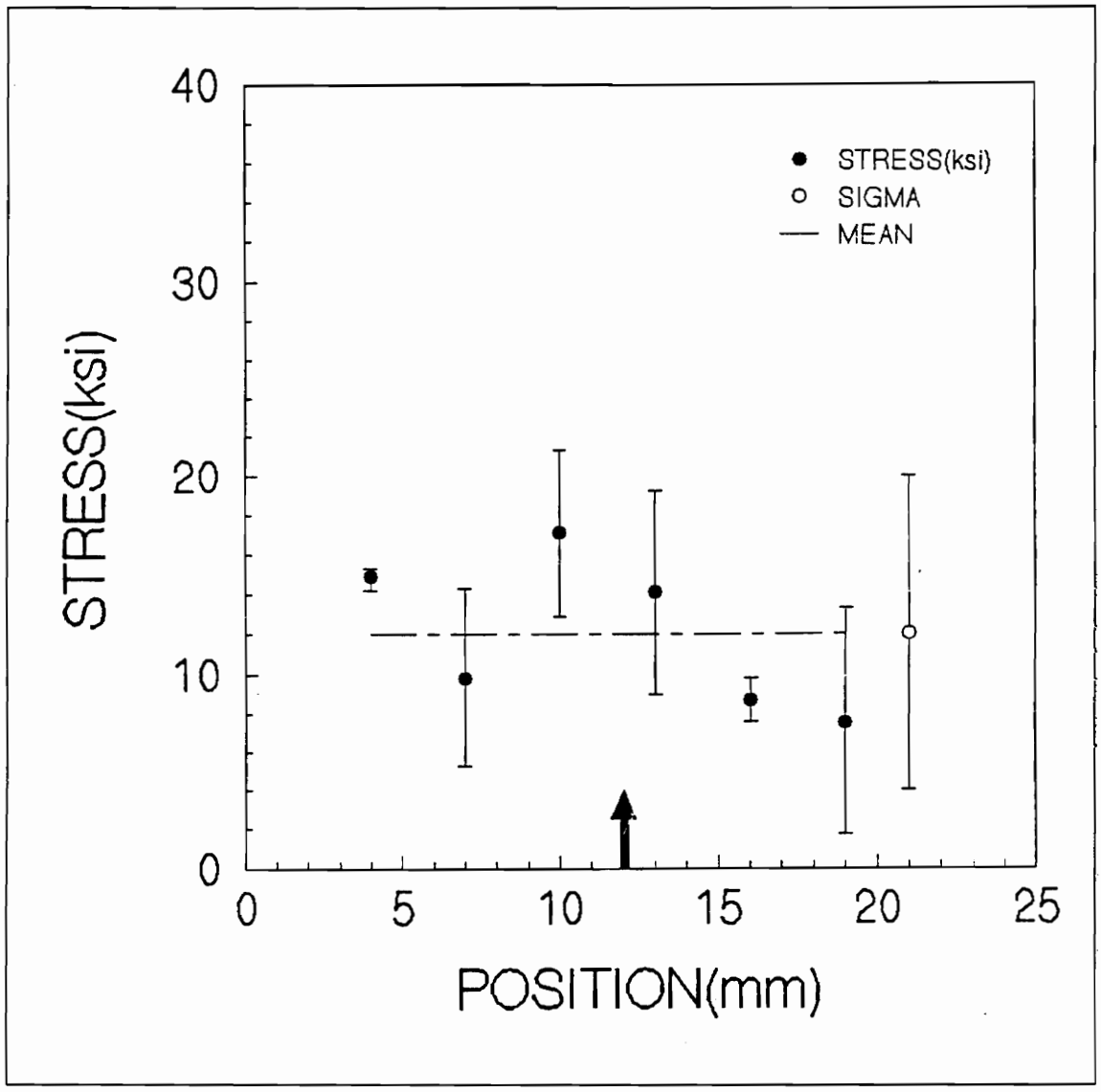


Figure 5.24: Residual stress measurements of sample 2 laser trimmed with the JK700 laser. All data is within $2\sigma$ of the average stress. The arrow represents the location of the laser cut.

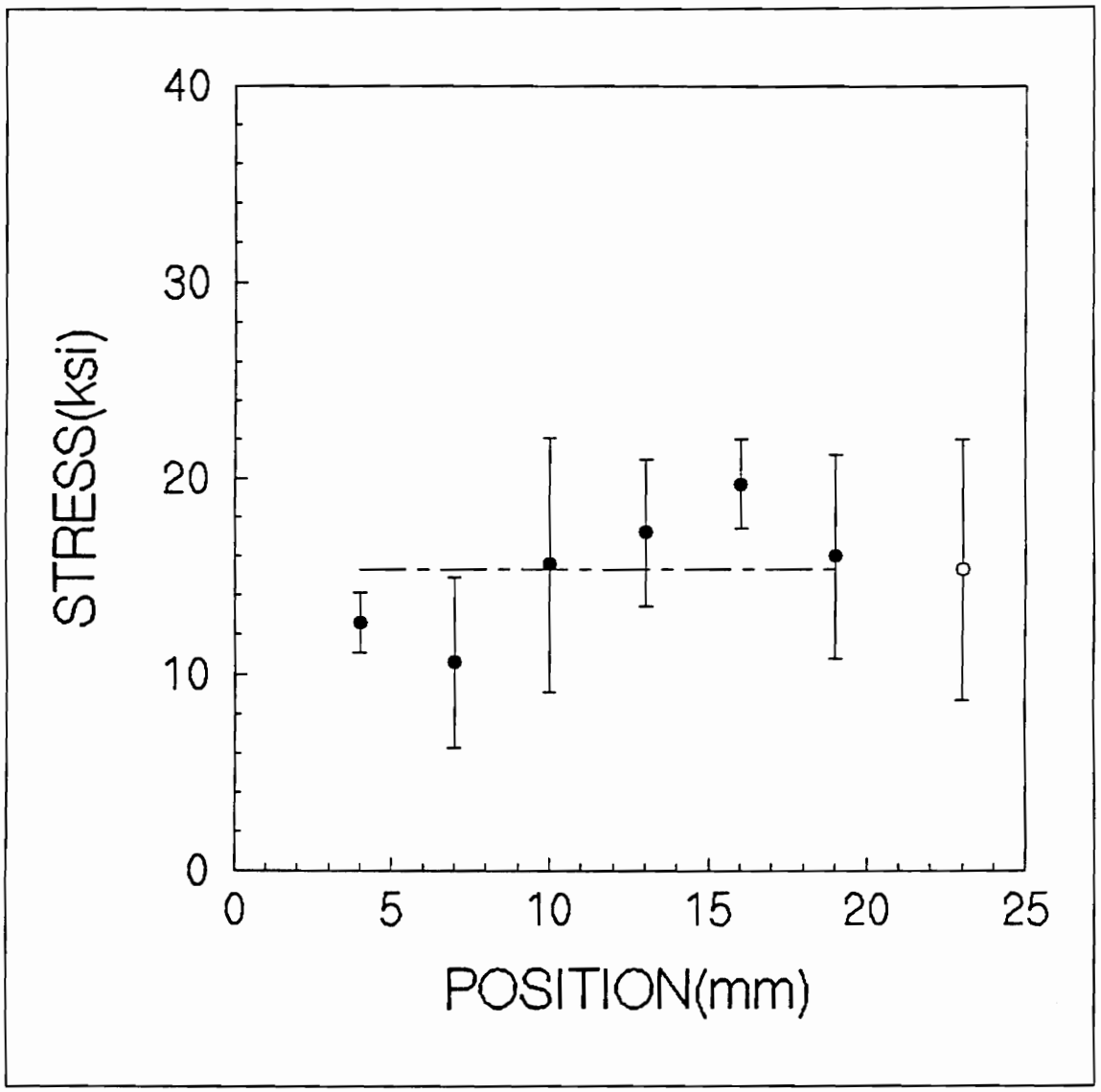


Figure 5.25: Residual stress measurements of sample 3 laser trimmed with the JK700 laser. All data is within $2\sigma$ of the average stress. The arrow represents the location of the laser cut.

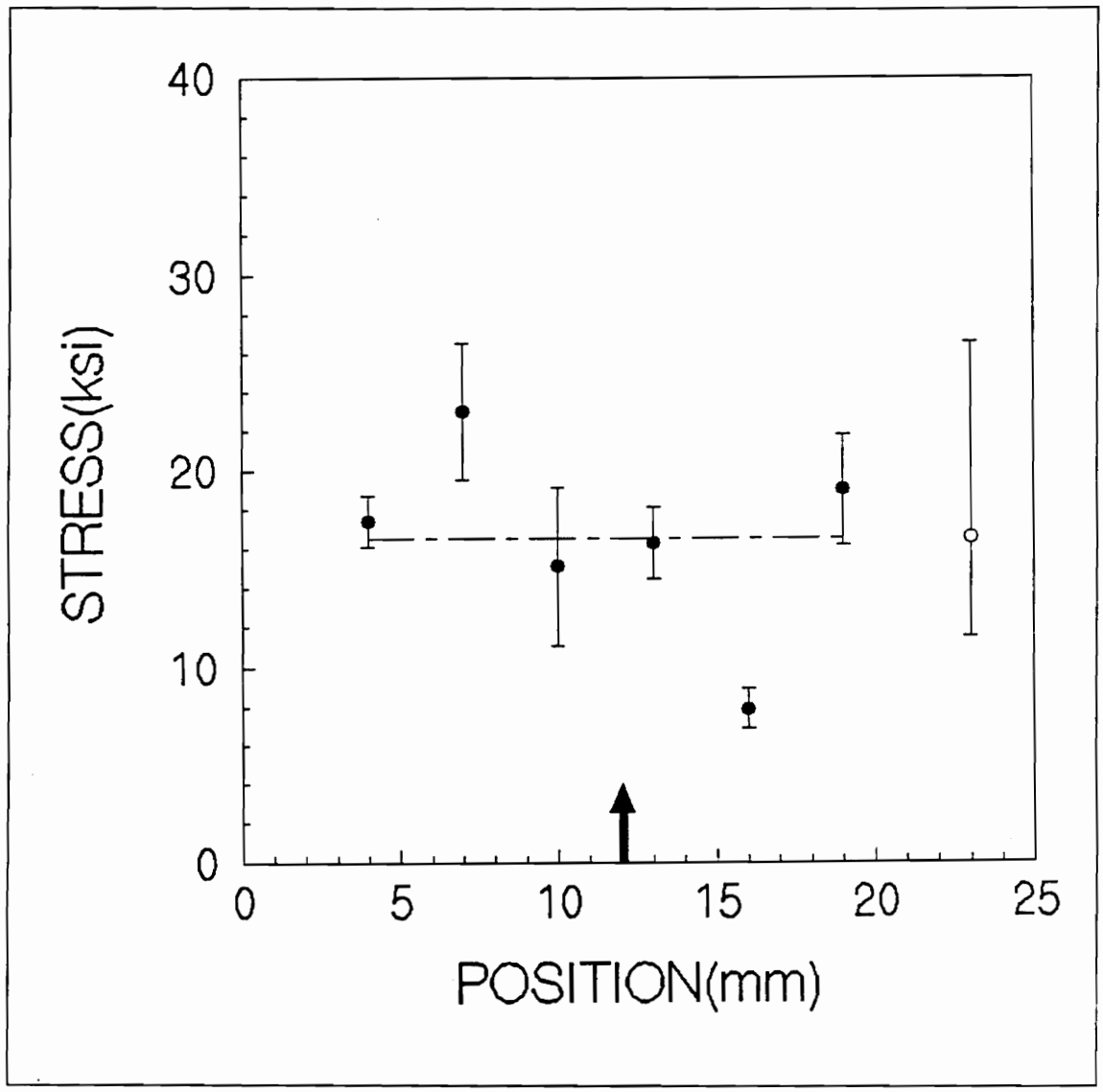


Figure 5.26: Residual stress measurements of sample 4 laser trimmed with the JK700 Laser. All data is within $2\sigma$ of the average stress. The arrow represents the location of the laser cut.

the restraint on the substrates. Yet Another possibility is the constraint resulting from the strain gages themselves. Since the volume of the glassy phase was found to be insignificant as reported in Chapter 4, the first hypothesis can be ruled out. This leaves the restraints on the substrates and the strain gages as the remaining source of why tensile stresses measured on the front and back of the substrates back side averaged about 13 ksi ([90 MPa]) while the front side averaged between 13 - 17 ksi ([90 - 118 MPa]). Thus, as was observed with the ESI laser trimmed samples, the residual stresses in the JK700 trimmed samples are also uniformly distributed across the sample. However, the variance of the measurement is somewhat larger. In general, surface contraction following heat input from the laser trimming process is given by $\alpha(T_0 - T\prime) = T_\alpha$, where $T_0$ and $T\prime$ are the initial and final temperatures of the substrate and "$\alpha$" is the coefficient of thermal expansion. Upon restraint tensile stresses will vary in the surface. Therefore, the integration of stress over the entire volume of the sample is essentially zero:

$$\int_V \sigma_{ij} dV = 0 \tag{5.4}$$

where v is the volume and $\sigma_{ij}$ is the general second rank stress tensor [26]. This implies that for stress equilibrium the surface stress must be balanced by compressive stresses in the interior.

## 5.5 Dynamic Strain Measurement Procedure

### 5.5.1 Procedure

Strain measurements were performed to ascertain the behavior of the substrate in situ during the laser machining procedure. Here, the strain gages were attached to the back side of a substrate and the strain was recorded in real time as the laser beam traversed the sample. The strain gages measured the strain induced in the substrates as a function of laser processing. The substrates go through dimensional and phase transformations when laser machined and the strain gages measured the apparent strain due to these changes.

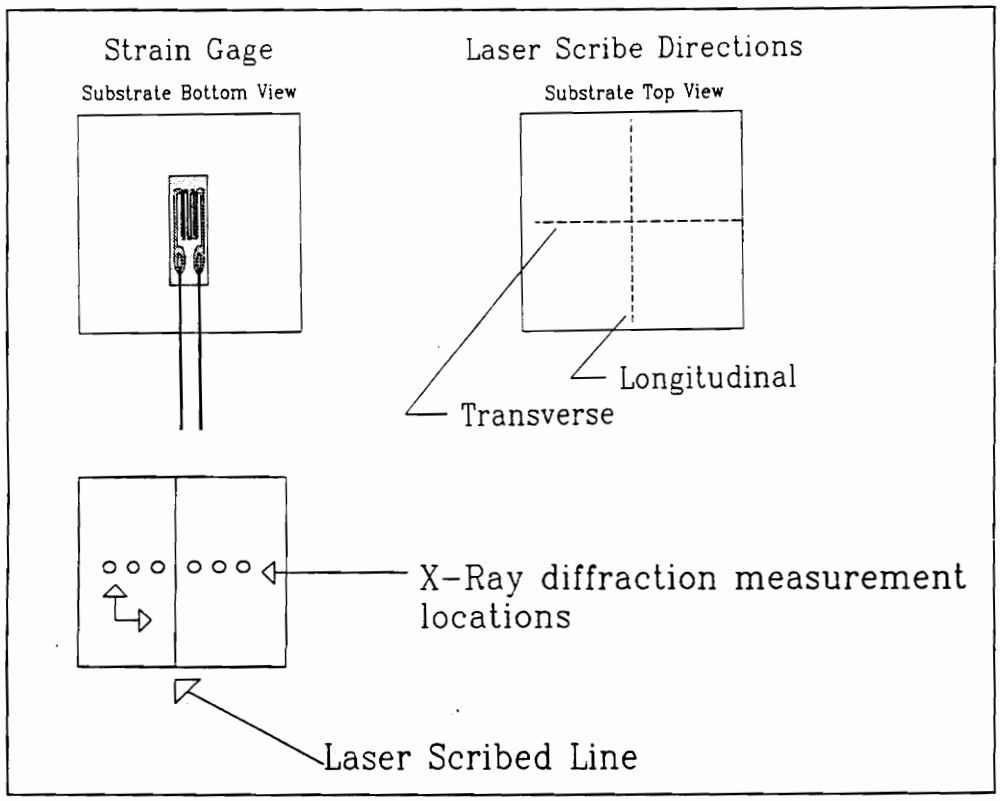


Figure 5.27: Sample geometry showing strain gage location and laser trim marks. Only one line was measured with X-rays across this sample to detect peak stresses near the heat affected zone.

The strain gages utilized in the dynamic measurements were general purpose CEA-060250UW-350 purchased from The Measurement Group in Raleigh, NC. The strain gages were well suited for static or dynamic stress analysis and thus chosen to match the coefficient of thermal expansion of alumina. A strain gage was centered and adhesively attached to the back side of a substrate that was subsequently laser machined. Strain values were calibrated and adjusted with the Measurement Group Model P3500 and Measurement Group Model SB-10 strain gage instrumentation units. A diagram illustrating the laser trimming paths and strain gage attachment are shown in Figure 5.27 and Figure 5.28 illustrates the experimental setup.

Two samples were laser trimmed and both, transverse and longitudinal stresses were

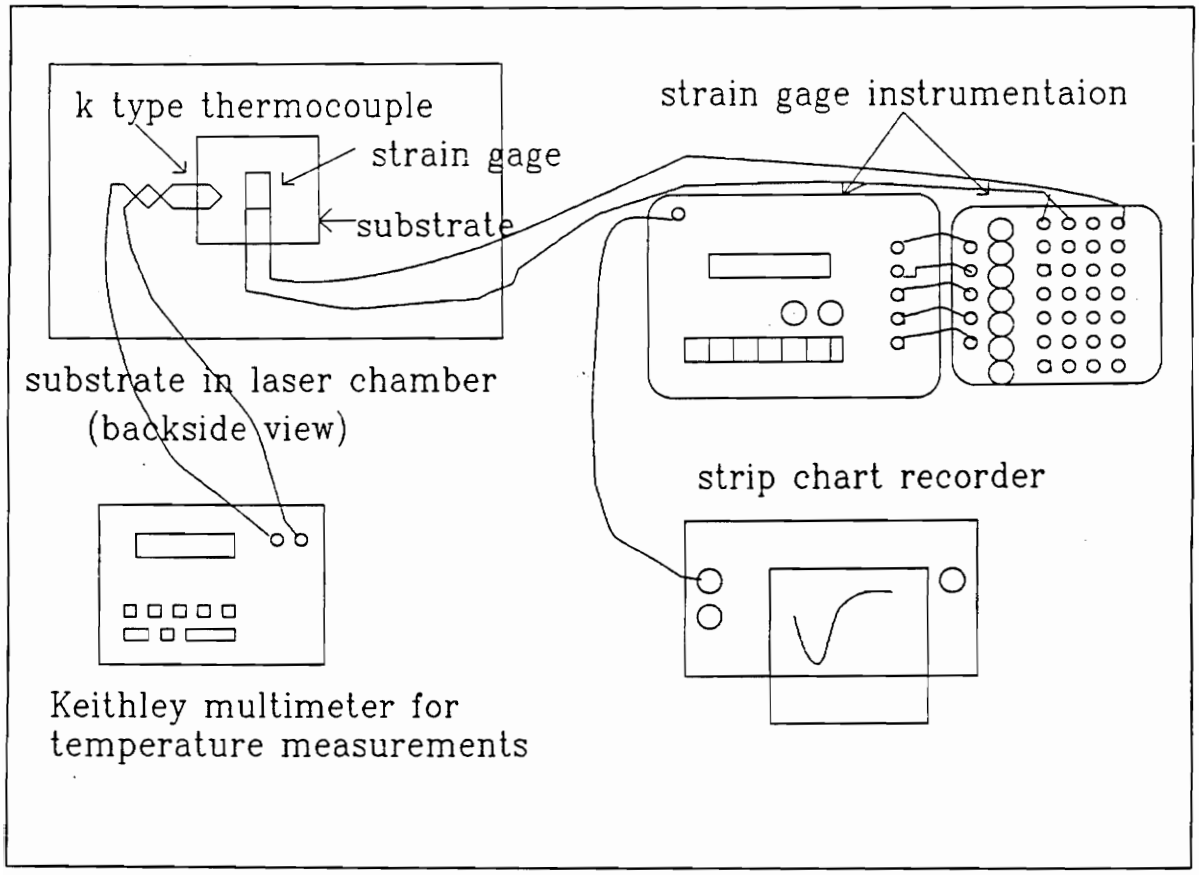


Figure 5.28: Schematic of laser trimming and and strain gage measurements of an alumina substrate.

recorded. Two samples were laser trimmed with two passes, two transversly in one substrate and two longitudinally in the other substrate. The laser used was the JK700 Nd-YAG 400 watt laser system described previously. Figures 5.29 (a) and (b) illustrate the strains recorded during a single laser pass. In these experiments the laser beam traversed the full length of the substrates (1 inch) in approximately 10 seconds. During this time a rapid and large increase in compressive strain in the strain gage as the thermal expansion of the sample on the top side forces the bottom (strain gage) side into compression. Following traverse of the beam ($t > 10$ seconds) the strain was recorded as the sample cooled to room temperature. A large, net tensile strain is observed as the top side contracts, placing the bottom (strain gage) side into tension. Figures 5.30 (a) and (b) illustrate double laser pass on one substrate. The microstrains are shown to have increased by about 110% for transverse laser pass and about 104% for the longitudinal case. Thus, it is seen that the strains are approximately additive as a function of laser pass.

From the initial heating, compressive stresses as measured in the back side result from the restraints on the substrate. As the substrate cools, tensile stresses are subsequently created. Initially the melt zone created by the laser interaction is stress free and the adjacent HAZ is found to be in compression as shown by Figures 5.29 and 5.30. Stresses measured in and around the HAZ are almost symmetrical to the stresses farther away from the HAZ. This may be due to relaxation resulting from plastic deformation at higher temperatures. Upon cooling (contraction), these layers generated large tensile stresses, since the adjacent untreated bulk regions initiated constraints on these layers. More importantly, the viscoelastic flow of the glass matrix phase may serve as a stress relaxation mechanism at lower temperatures since X-ray residual stress measurements showed stresses considerably lower than those reported by the dynamic strain measurements.

Although the fracture strength of the samples laser machined in this research was not measured in this work, Gardner [46] and Beauchamp observed a reduction in the fracture strength after laser machining. This was found to be the effect of laser induced flaws in the melt zone.

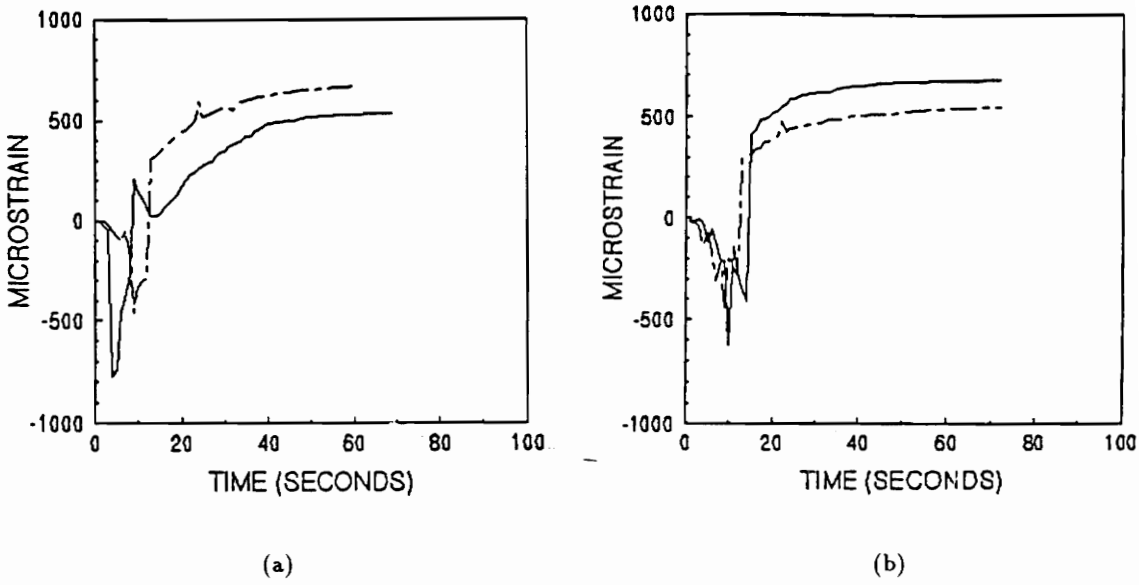


Figure 5.29: Dynamic strain measurements (single laser pass) (a) Single longitudinal and (b) Single transverse laser pass versus microstrain. The dashed lines and data points represent different samples. The laser traversed the sample in approximately 10 seconds. Strains generated after 10 seconds were those resulting from thermal gradients in the sample (see text for discussion).

Flaws such as microcracks that propagate behind the laser paths are due to thermal stresses created from differential contraction as the melt regions cooled as well as the adjacent heat affected boundary.

Since the glassy phase served as a stress relieving mechanism the mechanical strength of 96% alumina substrates are not reduced as much as purer aluminas, viz., 99% alumina [46].

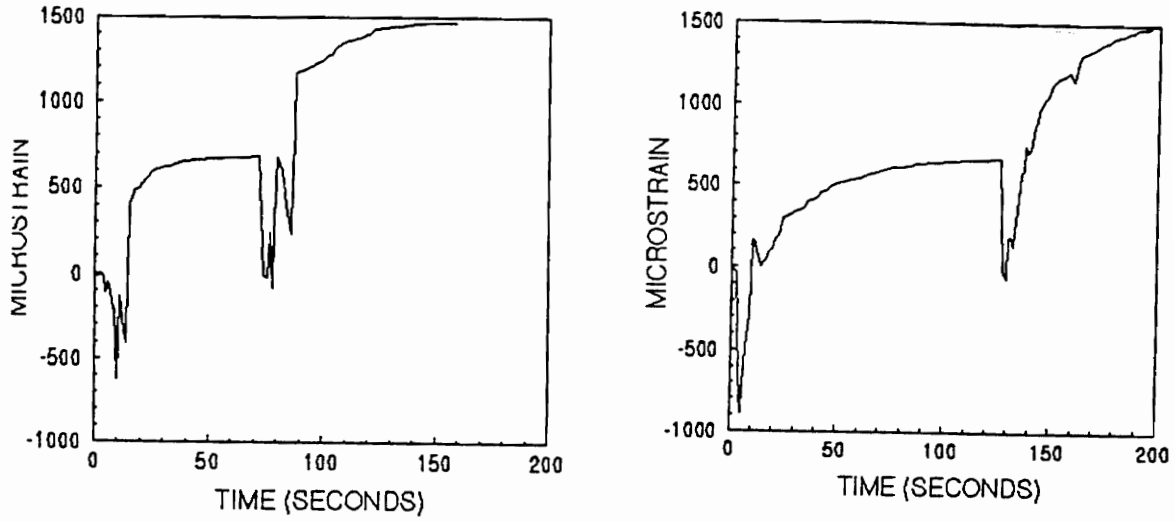


(a) (b)

Figure 5.30: Strain versus beam transit time for double (a) double longitudinal and (b) double transverse laser passes. Dashed line is after first laser pass, data point shows microstrain after second laser pass. The increase in the strain from the second laser pass illustrates the effect of superimposed strains with respect to the first laser pass strains.

**Dynamic Strain Measurements Versus Laser Power Level**

If a material is prevented from expanding as in the early dynamic strain measurements, thermal expansion is halted, upon heating the sample will undergo initial compression as seen in the strain vs position figures. This compression takes on the value of

$$\sigma = E\alpha_l(T_2 - T_1)/(1 - \nu). \tag{5.5}$$

where $\alpha_l$ is the coefficient of thermal expansion and $\nu$ is Poisson's ratio [7]. Therefore, failure results when the thermal stress approaches the fracture stress. And if the material is porous, as in the case of the substrates used in this research, large or small stresses may be initially stopped by the pores [7].

The experiments described in the previous section involved samples which were clamped on two sides. Some component of the observed strain must have arisen from clamping stress. To determine the significance of such stress, the experiments were repeated with free standing samples.

Dynamic strain plots of each unconstrained sample are shown in Figures 5.31 through 5.34. The results are significantly different from those of the constrained samples shown in Figure 5.29. Samples K1 and K2 are shown in Figure 5.31 and 5.32, K3 and K4 are given in Figure 5.33 and 5.34. As sample K1 (0.75 joules) was initially laser trimmed, it showed an initial increase in tensile strain, reaching a max of about 500$\mu\epsilon$, indicating stresses of about 25 ksi (172.5 MPa). The strain decreased after the laser was cut off. At this point the sample began to cool, resulting in an increase in tensile stresses created by this controlled fracture process. The behavior of this sample showing initial tensile strain illustrates the effect of the sample being unconstrained, allowing free thermal expansion. A similar behavior is seen in Figure 5.32 for sample K2 (0.50 joules). Sample K2 started in tension again after the laser was removed, its behavior started in compression, and as it cooled tensile stresses were generated. The maximum tensile stress reached 8.8 ksi (61 MPa) and compressive stresses reached a maximum of -20 ksi (-138 MPa). Sample K3 (0.25

Joules) showed nearly equal compressive and tensile stresses at the onset; however, as the sample cooled the strains returned to nearly zero, indicating 0.25 joules of energy had no controlled fracturing effects. The sample showed tensile stresses to increase 15 to 20 ksi (105 MPa to 140 MPa) which are in agreement with XRRSA results. Sample K4 (0.1 joules) indicates a similar situation as seen in Figure 5.33.

## 5.6 Summary

Two laser systems were utilized for laser machining alumina substrates, the ESI 30 watt and the JK700 400 watt laser. The ESI laser was used in the initial stages of laser machining since it was easily accessible, but it was hard to control laser processing parameters. The JK700 laser was then chosen primarily due to its ability to allow more control over laser processing parameters. The ESI laser showed good trimming capability illustrating that it can laser trim without any crack branching. The JK700 laser showed the opposite result showing crack branching and crack propagation along the laser path. However, a positive result for the JK700 laser is that it created a crack propagation phenomena exhibiting a controlled fracture behavior. This behavior resulted in easy sample separation after laser trimming.

Machining ceramic substrates with the Nd-YAG laser generated the following characteristics:

- The alumina substrates in this study were subjected to thermal input instead of a mechanical load (which is more directly detrimental).
- A very short interaction time exists in which the laser beam touches the substrate surface. This fast process is preferable over other machining techniques for ceramics.
- The heat affected zone was found to be negligible in the processed parts, since laser trimming distributes the stress isotropically. This is probably due to the nature of the defect structure.

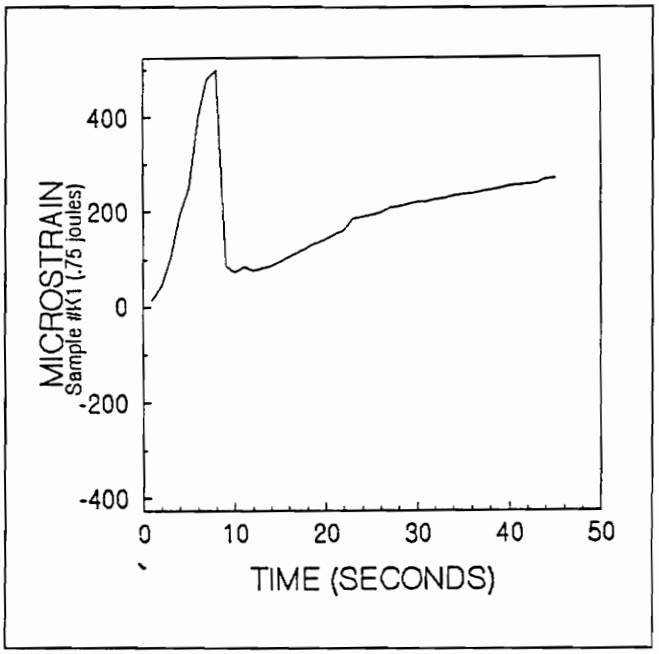


Figure 5.31: Dynamic strain measurements of samples K1 (laser trimmed using 0.75 Joules of laser power from the the JK700 laser at ITT).

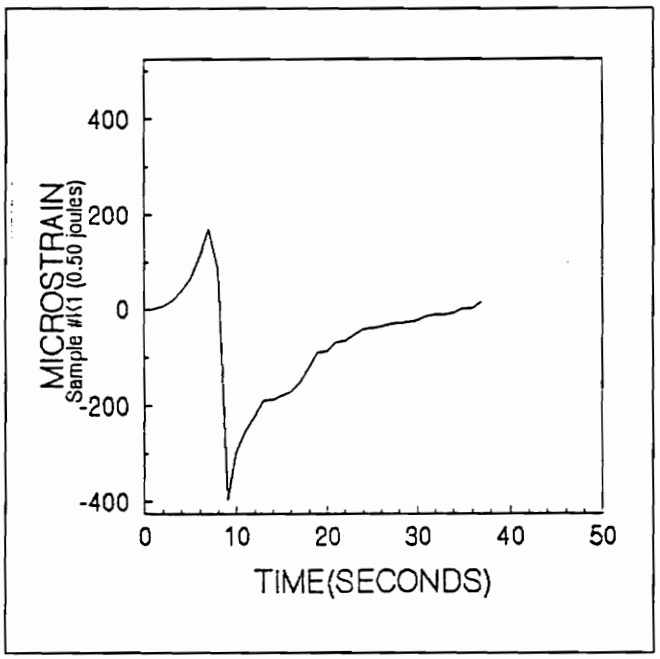


Figure 5.32: Dynamic strain measurements of sample K2 (laser trimmed using 0.50 Joules of laser power trimmed from the JK700 laser at ITT).

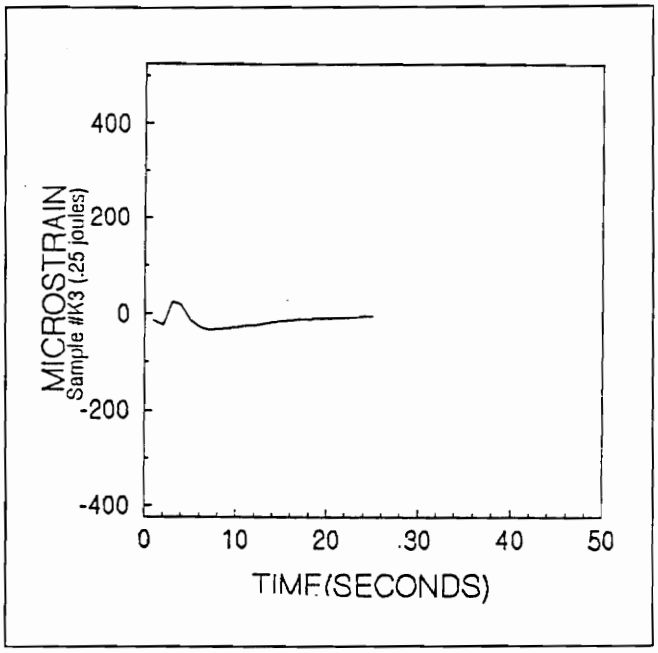


Figure 5.33: Dynamic strain measurements of sample K3 (laser trimmed using 0.25 Joules of laser power trimmed from the JK700 laser at ITT).

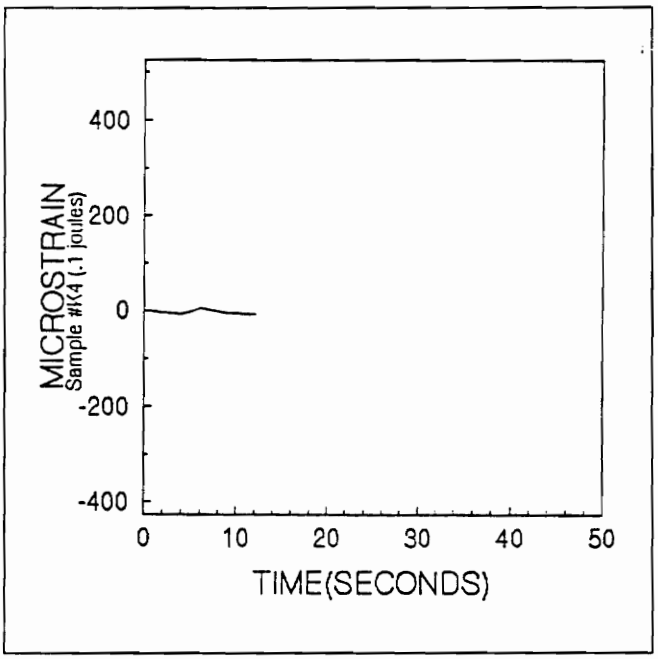


Figure 5.34: Dynamic strain measurements of sample K4 (laser trimmed using 0.1 Joules of laser power trimmed from the JK700 laser at ITT).

- Tangential and radial cracks were not developed on the exterior of the lines in the substrates trimmed with single or double pass, as shown by dye penetrant and fractographic techniques.

- Although $Al_2O_3$ is susceptible to thermal shock, trimming with powers as high as 1.06 joules produced no radial microcracks from the trimmed lines. However, residual stresses as great as 160 MPa (23 ksi) were generated. Pabler reported on the use of 150 W $CO_2$ lasers working in a super pulse mode to avoid any fracturing [65]; however, he does not address residual stresses, which are just as detrimental. Tensile residual stresses are known to result in fracture and ultimate failure of $Al_2O_3$.

Residual stress measurements have shown that the stresses in the substrates are essentially uniformly distributed across the substrates. Strain gage measurements have illustrated that the behavior of the substrates result initially in compression at the onset of laser trimming and result in tension upon cooling immediately after the laser trimming process. The next chapter will discuss the results in some detail and draw some general conclusions on what the data presented here may mean.

# Chapter 6

# DISCUSSION AND CONCLUSIONS

Three approaches have been taken to understand the development of residual stresses in laser trimmed $Al_2O_3$ substrates: physical characterization of the various processing steps, X-ray residual stress analysis (XRRSA) measurement of before and after laser trimming the substrates, and in situ dynamic strain measurements.

Materials characterization played a major role in this research. A variety of techniques were used in order to completely characterize the alumina substrates studied. SEM, ESCA, and general optical fractography proved to be the most useful generating insight into both composition and microstructure. EPMA and areal analysis (point counting) has shown that a discontinuous (not networked) glassy phase with a volume fraction of 7.4%, an aluminum magnesium spinel phase having a volume fraction of 3.4% and pores with a volume fraction of 4.4% are present. Because the glassy phase is less than about 15-20% as required for continuity, we conclude that the alumina substrates may be considered to be a uniform distribution of small particles in a continuous matrix.

Other nondestructive evaluation techniques such as dye penetrant and x-ray radiography results were negative. Acoustic microscopy was also used to explore other defects due to trimming. This technique may have detected the HAZ of the laser trimmed substrates.

The substrates were laser machined with two techniques, laser scribing using a ESI 30 W laser and controlled fracturing using a JK700 laser. The ESI laser operated on a Q-switch mode (extremely fast overlapping continuous laser beam train) while the JK700 laser operated in pulse mode. Residual stresses were measured after laser processing and were found to be tensile in nature and uniformly distributed across the substrates. No peak stresses were observed from the XRRSA measurements in the HAZ; stresses in this zone

were found to be of the same magnitude as in the surrounding regions.

Dynamic strain measurements of the substrates during laser machining with the JK700 laser showed a large difference between constrained and unconstrained substrates. Constrained substrates showed large initial compressive stresses and, upon cooling, large tensile stresses were noted. Unconstrained substrates showed initial tensile stress behavior upon laser machining and final tensile stresses were observed during and after cooling. XRRSA measurements for the constrained substrates showed a factor of two reduction in tensile stresses compared to the final in-situ tensile measurements. It was noted that the laser trimmed samples showed a bending deflection which was measured by the strain gage, but not by XRRSA. In addition this discrepancy may be attributed to rapid stress relaxation due to controlled cracking and heating. The unconstrained substrates in-situ measurements were in good agreement with XRRSA measurements.

Substrates laser trimmed with the JK700 laser showed complete separation at 1.06 J of laser power. Even at the maximum laser power for the ESI laser complete separation was not observed. Stress raising cracks were also observed for the lowest power level when the JK700 laser was utilized.

We have illustrated that laser trimming introduces thermal stresses into the substrates. From ANOVA and Kolmogorov-Smirnov (K-S) statistical data analysis, residual stress measurements of laser trimmed substrates were shown to be isotropic. Initial laser trimming experiments showed stresses that are about 15 to 25% of the modulus of rupture of alumina (278 MPa). More importantly, both ANOVA and K-S statistical analysis showed essentially uniform distributions of stress over the entire surface even though the heat input was along two very narrow lines (about 13$\mu$m wide) when the ESI laser was employed. The JK700 laser produced the same result with even a higher incident laser beam energy. Thus, unlike the welding of metals, there is no residual stress concentration in the heat affected zone of the laser cut.

The uniformly distributed tensile stresses measured across the substrates even when high input laser energy was used may be attributed to the various phases of the alumina

substrates acting in such a manner as to average out the stresses throughout the substrate's body. Furthermore, it is well known that when a material or surface is treated the atoms affected will move to new positions of equilibrium due to irreversible damage. If the damage occurs where there are no native defects, the areas that were irradiated may increase and result in microvolume deformations thus creating plastic or viscous flow behavior. This behavior may explain why there are no detectable peak stresses in the HAZ of the substrates.

However, the uniform stress distribution observed in the substrates may also be due to the creation of plastic or viscous flow behavior resulting from the laser machining process. The pore-glass mechanism proposed below could aid in this process. More importantly, since there are three major phases (glass, pores, and $MgAl_2O_4$) including trace elements found in the substrates the stresses in each phase will average out the total stress in a random but uniform manner upon laser machining.

In addition to the glassy phase playing a role in redistributing and thus lowering the stress, pore size effects may also serve as a stress reduction mechanism and therefore may contribute in the creation of the uniform stress distribution process. This means that although the pores serve to conduct heat (as explained below), their existence may hinder large thermal stresses by reducing the thermal shock wave caused during laser machining. The stress wave will impact the pore or empty space, and will be slightly uniformly degraded through scattering. In general, pore size distribution is known to affect heat flow by both conduction and radiation and can contribute to heat transfer at high temperatures. If the pores are relatively small, they are a good shield against heat flow which lowers the thermal conductivity [7].

From this, when laser energy is incident upon the $Al_2O_3$ substrates, translating and performing laser ablation (vaporization and material removal), thermal stresses are believed to be propagating throughout the volume in a uniform manner due to a pore-glass radiation shield heat transfer mechanism. For metals, this mechanism is not observed since thermal conductivity is high. Thus, the anticipated high tensile residual stress in the HAZ is not seen in the ceramic as is the case in welded metals.

The JK700 laser was also employed in the dynamic strain gage measurements and laser energy variation experiments. This laser was found to produce initial compressive stresses as great as 40 ksi (278 MPa) and final tensile stresses as great as 60 ksi (414 MPa) as measured by the strain gages when the samples were trimmed with 1.06 input power. These large stresses included both macroscopic strains due to sample bending as well as microscopic (intergranular) residual stresses since X-ray diffraction measurements showed average stresses less than half of these values which explains why the maximum measured stress on these samples was 17 ksi (118 MPa) as opposed to the 40 to 60 ksi calculated from the strain. Despite this reduction in stress, the remaining tensile stresses should be removed from the substrates before use. These data are consistent with previous laser trimming in which stresses of 30% to 40% of the modulus of rupture were observed [12, 27]. In the earlier work, however, the laser parameters were not so well controlled as in the present study.

Furthermore, if a constant heat source is applied to the substrate for controlled crack growth, as in the case of the action of the JK700 YAG laser, a line of assumed fracture heated by the laser moving at a certain speed will cause the substrate to increase in volume. If the substrate is hindered as in the previous dynamic strain measurements, compressive stresses are created in the surface (since the temperature is high there). However, tensile stresses are created at a certain depth "x" beneath the heated zone. These stresses will act everywhere at the dimensions of the fixture holding the sample in place. Figure 5.2 illustrated how a laser beam incident on ceramic substrate behaved and dynamic strain measurements show similar distributions as this theoretical plot.

From this research, it may be concluded that laser trimming alumina substrates will result in large uniformly distributed tensile residual stresses. The reason for the uniform distribution may be attributed to the pore-glass radiation shield mechanism or due to the various phases acting together and averaging out the stress. The glassy phase may play a significant role since it was found to make up a volume fraction of 7.4% and is randomly distributed as is the pore phase. The tensile stresses generated as a result of laser trimming

are possibly superimposed stresses since there may be a coefficient of thermal expansion mismatch between the alumina matrix phase and the glass precipitate phase generating the initial residual stresses [67].

Further, it was discovered that the substrates may be laser trimmed in three ways, by scribing (ESI laser), controlled fracturing (JK700 laser) and a two—ended controlled fracturing process using two lasers as proposed by other investigators [31]. Scribing was found to require a large load applied to the part in order to complete the separation process, while controlled fracturing, and two—ended controlled fracture requires little or no additional mechanical load for separating the part. It is important to note that although the ESI laser exhibited cleaner edges after its use, nonuniform separation was seen after a mechanical load was applied at the laser scribed region; this was never observed when the JK700 laser was used. Therefore, it is recommended that a combination of both lasers be used (in a single laser pass) in the process industries for laser machining alumina for thick applications. From this, one will get the clean edges as seen from the ESI laser results and the controlled fracturing as observed from the JK700 results (nonuniform separation is avoided using controlled fracturing).

# Chapter 7

# RECOMMENDATIONS FOR FUTURE WORK

The present work has shown that laser trimming is a complex and challenging process and that the alumina substrates are not always nearly stress free as received from the vendor. Therefore, it is important to perform nondestructive evaluations on the as-received material. For instance, before laborious x-ray stress experiments are performed on as received material, the substrates could be inspected more efficiently by X-ray radiographic techniques (preferably microfocused), ultrasonic or more sensitive acoustic microscopic techniques. Which ever technique generates the fastest and most accurate result should be utilized.

Materials characterization work should continue to be employed through whatever process methodologies are employed, and characterization should involve the following procedures:

- continue SEM and EPMA work. EPMA seems to be the best method to perform quantitative analysis on the substrates. Compositional maps with this technique should especially be applied to diamond cutting as well as laser trimming and any other mechanical separation techniques (water jet, for instance),
- employ other techniques such as secondary ion mass spectroscopy (SIMS), atom probe topographical techniques, etc., for further chemical and structural analysis,
- perform basic fractographic methods to determine crack propagation origins and flaw effects in the laser trimming process, and
- study the effect of pore size on laser heat transfer energy, to test whether the pore phase in the substrates has an effect on thermal stresses.

Experimental work can continue in a variety of ways. Other residual stress methods could be applied to the substrates in order to compare results and experimental accuracies. Other methods could include:

- performing residual stress measurements on the substrates using two different stress analyzers, e.g., the TEC and Scintag machines. To monitor the accuracy of the results.
- perform XRRSA on a higher sensitivity machine such as the Scintag system because of the high modulus of $Al_2O_3$.
- perform residual stress measurements of various geometrical shapes and thicknesses of alumina,
- using synchrotron radiation sources to measure properties after laser trimming, and before laser trimming. A high brilliance X-ray source such as those of synchrotron machines may find transformed phases that conventional X-ray sources are unable to detect,
- varying the laser parameters to narrow the kerf or trim width on the samples. The estimated widths for substrates trimmed with the JK700 laser were about 300$\mu$m compared to 13$\mu$m of the ESI laser,
- annealing the substrates to remove or redisttribute the residual stresses. New and conventional techniques could be performed such as microwave annealing, laser annealing or vacuum oven heating,
- measuring the state of stress in different alumina compositions. For instance, measure the state of stress vs purity, e.g., 96% versus 98% or even 99% alumina to look for similarities or differences. These measurements could aid in substrate evaluations, and
- performing microanalysis or SEM and EPMA on various phases of the hybrid metallization processes. This procedure could aid in determining phase change anomalies

between substrate and metallization materials.

The research presented here utilized several models for data analysis and interpretation; however, more insight is needed from newer statistical techniques such as experimental design and Taguchi methods. These techniques could allow for improved ways to guide experimental work.

Finally, theoretical work is needed to model the role of thermal stresses generated from laser machining alumina substrates. Possible work could include the following:

- finite element analysis of the laser/ceramic interaction zone to predict residual stress or other mechanical deformations,
- develop a model for the role the glassy phase plays in determining the level of residual stresses in $Al_2O_3$ substrates,
- model the contribution the initial stress state makes on the overall stress distribution in the substrates, and
- correlate the nature of residual stresses in diamond—cut substrates to those which have been laser trimmed.

Although there are still many variables to understand, X-ray residual stress analysis is a very reliable nondestructive evaluation technique for predicting failure in ceramic products. The technique shows promise for application in the electronics substrate industry.

# REFERENCES


[1] Beck, G., "Preface," from International Conference On Residual Stresses, ICRS2, G. Beck, S. Dennis, and A. Simon, eds, Amsterdam: Elsevier Science Publishers, 1989.

[2] Mura, T., Micromechanics of Defects in Solids, The Hague, The Netherlands: Martinas Nijhoff Publishers, 1982.

[3] Noyan, I.C., and J.B. Cohen, "Residual Stresses in Materials," American Scientist, **79**, March-April 1991, pp. 142-153.

[4] Goebble, K., "Nondestructive Evaluation of Advanced Ceramics," Proceedings of the 2nd European Symposium on Engineering Ceramics, Nov. 1987, pp. 99-159.

[5] Hamann, C., and Rosen, H-G.R, "Laser Machining of Ceramics and Silicon", Proceedings, SPIE(Society of Photo-Optical Instrumentation Engineers), High Power Lasers, E.W. Kruetz, et al, editors, March 31-April 3, 1987, The Hague, The Netherlands:, **801**, pp. 130-137.

[6] Colm, I.J., Ceramic Science for Material Technologist, London: Hill Publishers, 1983.

[7] Kingery, W.D., H.K. Bowen, and D.R. Uhlmann, Introduction to Ceramics, 2nd ed., New York: John Wiley & Sons Publishers, 1960.

[8] Lange, F.F., M.R. James, and D.J. Green, "Determination of Residual Surface Stresses Caused by Grinding in Polycrystalline $Al_2O_3$," Communications of the American Ceramics Society, Feb., 1983, **66**(2), pp. C16–C17.

[9] Brinksmeier, E., H. Siemer, and H.G. Wobker, "Requirements on Nondestructive Testing Methods after Machining of Ceramics," P. Holler, V. Hauk, G. Dobman, C.O. Ruud, and R.E. Green, eds., Nondestructive Characterization of Materials, Berlin: Springer-Verlag, 1989, pp. 36-45.

[10] Johnson-Wallis, D., A.G. Evans, D.B. Marshall, and M.R. James, "Residual Stresses in Machined Ceramic Surfaces", Journal of American Ceramic Society, **69**(1), 1986, pp. 44-47.

[11] Schulz, N.N., M.T. Stawovy, J. Jinmyun, R.W. Robert Hendricks, and A. Elshabini-Riad, "The Effect of an Applied Load on the Electrical Characteristics of Thick Film Transmission Lines," Proc. of the Third Int'l Conference on Residual Stresses(ICRS3), held in Tokoshima, Japan, July 23-26 1991, Amsterdam: Elsevier Applied Science, pp. 632-637.

*REFERENCES*


[12] Schulz, N.N.,"The Role of Residual Stresses in Ceramic Substrate Materials for Hybrid Thick Film Applications," MSc thesis, Electrical Engineering Department, Virginia Polytechnic Institute and State University, February, 1990.

[13] Vest, R.W., Materials Aspect of Thick Film Technology, Ceramic Materials For Electronics, Processing Properties and Applications, 2nd Edition, Buchanan, R.C., ed., New York: Marcel Dekker Inc., 1991, pp.435-437.

[14] Loasby, R.G., and H. Barlow, Handbook of Thick Film Technology, (P.J. Holmes and R.G. Loasby, eds.), London:Electrochemical Publications Ltd., 1976, pp. 75-95.

[15] Holmes, P.J., and R.G. Loasby, eds., "Special Purpose Materials and Processes," in Handbook of Thick Film Technology, Electrochemical Publishers Ltd., 1976, pp. 185, 196-197.

[16] Topfer, M., Thick Film Microelectronics Fabrication Design and Applications, New York: Van Nostrand Reinhold Co., 1971, pp. 41-43.

[17] Hoffman, L.C., "Interaction of Thick Film Materials With Roll Compacted Alumina Ceramics," Int'l Journal for Hybrid Microelectronics, **6**(1), Oct. 1983, pp. 603-606.

[18] Southern, J.C., "Ceramic Aluminas: Manufacturing, Use and Characteristics," Advanced Ceramics Conference, Society of Manufacturing Engineers, SME, Dearborn, Mich., Feb. 20, 1989, pp.118-1—118-10.

[19] W.A. Crossland and L. Hailey, "Substrates," in Handbook of Thick film Technology, P.J. Holmes and R.G. Loasby eds., London: Electrochemical Publications Ltd., 1976, pp. 74-91.

[20] Dettmer, E.S., and H.K. Charles, "Fundamental Characterization of Aluminum Nitride and Silicon Carbide for Hybrid Substrate Applications," International Journal of Hybrid Microelectronics, **10**(2), 2nd Quarter 1987, pp. 9-18.

[21] Schulz, N.N., R.W. Hendricks, and A. Elshabini-Riad, "The Role of Residual Stress in Ceramic Substrate and Metallization Materials For Hybrid Thick Film Applications," Proc. 1989 Int. Symp. on Microelectronics, ISHM, Baltimore, 1989, pp. 220-226.

[22] Kurihara, Y., S. Takahashi, K. Yamada, K. Kanai, and T. Endoh, "Laser Trimming of Thick Film Resistors on Aluminum Nitride Substrates," IEEE Transactions on Components, Hybrids, And Manufacturing Technology, **133**(3), September 1990, pp. 596-602.

[23] Horiuchi, et al,"New Mullite Ceramic Packages and Substrates," IEEE Transactions on Components and Hybrids and Manufacturing Technology, **11**,(4), Dec. 1988, pp. 439-441.

*REFERENCES*


[24] Werdecker, W. and Aldinger, F., Proceedings of the Electronic Components Conference, IEEE, 1984, p. 404.

[25] Schulz, N.N, R.W. Hendricks, and A. Elshabini-Riad, "Role of Residual Stresses in Ceramic Substrate Materials For Hybrid Thick Film Applications ," Proceedings of the 1989 International Symposium on Microelectronics, Reston, Virginia: ISHM, 1989, pp. 220-226.

[26] Noyan, I.C., and J.B. Cohen, Residual Stress: Measurement by Diffraction and Interpretation, New York: Springer-Verlag, 1986.

[27] Venzant, K.L, R.W. Hendricks and Elshabini-Riad, A, "X-ray Diffraction Analysis of Residual Stresses in Laser Trimmed Alumina Electronic Substrates", National Society of Black Engineers Technical Symposium, New York, NY: NSBE, 1991, pp. 1-7.

[28] Lin, R., and Ericsson, T., "Residual Stress Distribution Around Laser Hardened Tracks in Cr-Mo Steel," Department of Mechanical Engineering, Linkoping University, S-581 83 Linkoping, Sweden.

[29] Tonshoff, H.K., and Emmelmann, C.,"Laser Processing of Ceramics", Power Beam Processing, Electron, Laser, Plasma Arc, Proceedings of the International Power Beam Conference, E.A. Metzbower and D. Hauser, eds., San Diego, Ca., 1988, pp. 199-205.

[30] Rosenfelder, O. and Reiter, H., Fortschrittsberichte der DKG, **1**(1) 1985, pp. 103-112.

[31] Měnćik, J. Strength and Fracture of Glass and Ceramics in Glass Science and Technology, **12**, New York: Elsevier Science Publishing Company, Inc., 1992.

[32] Evans, A.G. and Marshall, D.B., Fundamentals of Friction and Wear, D.A. Rigney, editor, American Society of Metals.

[33] Marshall, D.B., "Surface Damage in Ceramics," in Progress in Nitrogen Ceramics, F.C. Riley, ed., Boston: Martinus Nijhoff, 1983, pp. 635-56.

[34] Eigenmann, B., B. Scholtes, and Macherauch, "X-ray Stress Determination in Ceramics and Ceramic-Metal Composites," G. Beck, S. Denis, and A. Simon, eds., Proceedings of the Second International Conference on Residual Stresses, ICRS2, Nancy, France, New York: Elsevier Science Publishing Co., 1991, pp. 21-27.

[35] Macherauch, E., "Introduction to Residual Stress," in A Study of Residual Stress in Material Systems, J. Bernasconi and M. Roth, eds., France: Pergamon Press, 1987.

[36] Hauk, V., "Nondestructive Methods of Measurement of Residual Stresses," in Advances in Surface Treatments," J. Bernasconi and M. Roth, eds., France: Pergamon Press, 1987.

*REFERENCES*


[37] Cullity, B.D., Elements of X-Ray Diffraction, 2nd ed., Reading: Addison-Wesley Publishing Company, Inc., 1978.

[38] Gazzara, C.P., "The Measurement of Residual Stress With X-Ray Diffraction", AMMRC MS 83-1 Army Materials and Mechanics Research Center, Watertown Mass., 02172, May 1983.

[39] Machulka, G.A., Laser Working of Glass (in Russian; Lasernaya obrabotka stekla), Sovietskoe radio, Moscow, 1979.

[40] Courtney, S.B., J. Potet, M.J. Tricard, and R.W. Hendricks, "RS-base: A Residual Stress Database Management System", in Residual Stresses–III: Science and Technology, Proc. Third Int'l Conf. on Residual Stress, Tokushima, Japan, 23-26 July, 1991, H. Fujiwara, T. Abe and K. Tanaka, eds., Amsterdam: Elsevier Applied Science, (1992), pp. 1549-1554.

[41] Tricard, M., "An Expert System for the Validation and Interpretation of X-ray Residual Stress Data," MSc thesis, Materials Engineering Department, Virginia Polytechnic Institute and State University, May, 1990.

[42] Bass, M. editor, Laser Materials Processing, New York: North-Holland Publishing Company, New York, 1977.

[43] Duley, W.W., Laser Processing and Analysis of Materials New York: Plenum Press, 1983.

[44] Affolter, P., and H.G. Schmid, "Processing of New Ceramic Materials with Solid State Laser Radiation," Proceedings, SPIE, High Power Lasers, E.W. Kruetz, A. Quenzer, D. Sschuocker, eds., March 31-April 3, 1987, Hague, The Netherlands, **801**, (1987), pp. 120-125.

[45] Pabler, M., and G. Lensch, "Cutting and Scribing Alumina Ceramic Using a $CO_2$ Laser", Proc. of SPIE, High Power Lasers, Kruetz, E.W., A. Quenzer, and D. Schuocker, eds., March 31-April 3, 1987, Hague, The Netherlands:, **801**, pp. 283-287.

[46] Gardner, T.J. and E. Beauchamp, "The Effect of Laser Machining on the Strength of $Al_2O_3$ Substrate Materials", in Intersociety Symposium on Machining of Advanced Ceramic Materials and Components, April, 1987, R.E. Barks, K. Subramanian, and K.E. Ball editors, American Ceramic Society.

[47] Gladman, T and J.H. Woodhead, "The Accuracy of Point Counting in Metallographic Investigations," Journal of The Iron and Steel Institute, **194**, February 1960, pp. 189-193.

[48] Hendricks R.W., "One-And Two-Dimensional Position-Sensitive X-Ray And Neutron Detectors", Proceedings of the Symposium on Instrumentation for Tomorrow's Crystallography, Transactions of the American Crystallography, Assoc., **12**, 1976, pp. 103-146.

[49] Tanaka, K., K. Suzuki, and Y. Yamamoto, "Residual Stress Effect on Fracture Strength of Ceramics", in International Conference on Residual Stresses (ICRS2), G. Beck, S. Dennis, and A. Simon, Amsterdam: Elsevier Applied Science, 1989, pp. 15-26.

[50] Foster, D. C., and R. E. Tontodonato, "Correlation of X-ray Determined Residual Stress with Rupture Modulus in $Al_2O_3$", Senior thesis, Materials Science and Engineering Department, Virginia Polytechnic and State University, Blacksburg, Va., May, 1988.

[51] Abuhasan, A., C. Balasingh and P. Predecki, "Residual Stresses in Alumina/Silicon Carbide (Whisker) Composities by X-ray Diffraction", Journal of American Ceramic Society, **73**(8), pp-2474-2784.

[52] TEC Model 100 X-ray Stress Analysis System Operation and Operation and Maintenance Manual, Technology for Energy Corp., Knoxville, TN, 1985.

[53] Lumley, R.M., "Controlled Separation of Brittle Materials Using a Laser", American Ceramic Society Bulletin, **48**(9), 1966, pp. 850-854.

[54] Ott, L. An Introduction to Statistical Methods and Data Analysis, 3rd., Boston: PWS-Kent Publishing Company, 1988.

[55] Soarez, O.D. and M. Perez-Amor, Applied Laser Tooling, Boston: Martin-Nijhoff Publishers, pp. 15-45.

[56] Marshall, D.B. and Lawn, B.R., "Residual Stress Effects In Sharp Contact Cracking," Journal of Materials Science, **14**(8), 1979, pp. 2001-2012.

[57] Buchanan, R.C., "Electrical/Electronic Applications for Advanced Ceramics," Engineered Materials Handbook, **4**, ASM Int'l, Dec. 1991, pp. 105-110.

[58] Yoshioka Y., "X-ray Measurements of Elastic Constants and Residual Stresses in Alumina Ceramics," G. Beck, S. Denis, and A. Simon, eds., Proceedings of the Second International Conference on Residual Stresses, ICRS2, Nancy, France, New York: Elsevier Science Publishing Co., 1991, pp. 348-353.

[59] Yasukawa, A. and T. Sakamoto, "Stress Analysis and Hybrid Technology," Int. J. Hybrid Microlelectronics, **11**(1), 1988, pp. 12-18.

[60] Ester, L. and L.D. Hart, Alumina Chemicals, Science and Technology Handbook, Westville, Ohio: American Ceramics Society, 1990.

*REFERENCES*


[61] Dörre E., and H. Hubner, Alumina, Materials Research and Engineering, Berlin: Springer-Verlag, 1984.

[62] Grossman, D.B. and L.N. Fulrath, "X-ray Strain Measurement Techniques for Ceramics", Journal of the American Ceramic Society, 1961, **44**(11), pp. 567-71.

[63] Dölle, H., "The Influence of Multiaxial Stress States, Stress Gradients and Elastic Anisotropy on the Evaluation of (Residual) Stresses by X-rays," Journal of Applied Crystallography, 1979, **12**, p. 489-501.

[64] Siegel, S., and N.J. Castellan, Jr., Nonparametric Statistics for the Behavioral Sciences, 2nd ed., New York: McGraw-Hill Book Co., 1988, pp. 144-150.

[65] Pabler, M., and G. Lensch, "Cutting and Scribing of Alumina Ceramic Using a $CO_2$–Laser." Proceedings of SPIE, High Power Lasers, E.W. Kruetz, et al, eds., March 31-April 3, 1987, The Hague Netherlands, **801**, pp. 283-287.

[66] Korhonen, M.A., "X-Ray Diffraction Analysis of Aluminum Thin Films", Fourth Conf. on Nondestructive Evaluation Testing, Anapolis, Maryland, 11-14, June, 1990, R. Green and C.O. Ruud, eds., New York: Plenum Publishing Co., 1990.

[67] Hasselman, D.P.H., private communications, (October 1, 1992).

[68] Moon, D.W. and E.A., Metzbower "Temperature Measurements in a Mid-Plane of A Laser Beam Weldment in A36 Steel," Power Beam Processing, Electron, Laser, Plasma Arc, Proceedings of the International Power Beam Conference, E.A. Metzbower and D. Hauser, eds., San Diego, Ca., 1988, pp. 125-130.

# Chapter 8

# VITA

The author was born in Chicago, Illinois on December 13, 1960. He graduated from St. Ignatius College Prep, Chicago, Illinois in May, 1979. He then attended Rockhurst College, Kansas City, Missouri to pursue studies in physics and philosophy. He graduated from Rockhurst College with a B.S. degree in Physics with a major in Philosophy in August of 1983. He then returned to Chicago to work as an engineer at Ni-Tec Inc. and later in 1985 to 1987 he worked as a research assistant at Fermi National Accelerator Laboratory (Fermilab) To gain further knowledge in manufacturing he left Fermilab to work as a research and development engineer at ITT Electro-optics Products Division in August of 1987 to 1990. There he conducted research and development work on Third Generation night vision systems. He also made improvements in manufacturing processes while at ITT including statistical process control and hardware development for electronic materials characterizaiton. He left ITT to pursue fulltime graduate studies towards a masters degree in materials science and engineering at Virginia Polytechnic Institute and State University specializing in electronic materials. During the summer of 1993 the author conducted materials research on superconducting radio-frequency accelerator cavities at the Continuous Electron Beam Accelerator Facility in Newport News, Virginia.